2017

An Investigation of Premixed Flame Propagation in a Straight Rectangular Duct

Zakaria Movahedi
University of Windsor

An Investigation of Premixed Flame Propagation in a Straight Rectangular Duct

by

Zakaria Movahedi

A Dissertation
Submitted to the Faculty of Graduate Studies
through the Department of Mechanical, Automotive & Materials Engineering
in Partial Fulfillment of the Requirements for
the Degree of Doctor of Philosophy at the
University of Windsor

Windsor, Ontario, Canada

2017

An Investigation of Premixed Flame Propagation in a Straight Rectangular Duct

by

Zakaria Movahedi

APPROVED BY:

C. Devaud, External Examiner
University of Waterloo

R. Barron
Department of Mechanical, Automotive, and Materials Engineering

---

G. Rankin
Department of Mechanical, Automotive, and Materials Engineering

---

J. Defoe
Department of Mechanical, Automotive, and Materials Engineering

---

A. Sobiesiak, Advisor
Department of Mechanical, Automotive, and Materials Engineering

October 12, 2017

Author's Declaration of Originality

I hereby certify that I am the sole author of this thesis and that no part of this thesis has been published or submitted for publication.

I certify that, to the best of my knowledge, my thesis does not infringe upon anyone's copyright nor violate any proprietary rights and that any ideas, techniques, quotations, or any other material from the work of other people included in my thesis, published or otherwise, are fully acknowledged in accordance with the standard referencing practices. Furthermore, to the extent that I have included copyrighted material that surpasses the bounds of fair dealing within the meaning of the Canada Copyright Act, I certify that I have obtained a written permission from the copyright owner(s) to include such material(s) in my thesis and have included copies of such copyright clearances to my appendix.

I declare that this is a true copy of my thesis, including any final revisions, as approved by my thesis committee and the Graduate Studies office, and that this thesis has not been submitted for a higher degree to any other University or Institution.

Abstract

This work reports on the premixed propane-air flame propagation in a long length (1.8 m) straight rectangular (51×25 mm) duct. The mixture is assumed to be homogenous inside of the duct. Different equivalence ratios are examined. Two cases of fully opened and fully closed end outlet conditions are considered here. The flame behavior along with its propagation in the duct including initial stage of flame growing after the ignition, flame finger shape, flame-wall touch, flame flatten profile, tulip flame formation, tulip flame lips collapsing, and possible subsequent inversion/inversions are discussed. At each step, the flame-feeding flow interchangeable effect is explored using numerical simulations. Furthermore, the physical mechanisms behind the tulip flame and the subsequent inversion/inversions (especially the first flame inversion in opened end outlet case) are illustrated. Also, similarities and differences between these two phenomena are studied.

In terms of the numerical method, two CFD software packages, Star CCM+ and OpenFOAM have been utilized. The available EBU (Eddy Break-Up) combustion model in Star CCM+ code, while its reaction rate is limited to Arrhenius reaction rate, is employed (semi-laminar model). The XiFoam model which is the embedded turbulent combustion model in OpenFOAM is also used. Other famous numerical combustion models such as TFC (turbulent model), FSC (it can capture both laminar and turbulent conditions simultaneously), and TFM (laminar and turbulent combustion model) are made based on the XiFoam model. Also, these models (XiFoam, TFCFoam, FSCFoam, and TFMFoam) are coupled with adaptive mesh library in order to make the finer mesh at the flame location (3D geometries). The new models are named: XiDymFoam, TFCDymFoam, FSCDymFoam, and TFMDymFoam. Moreover, further modifications are made to make these new models ready for 2D cases. The capability of these models for simulation of premixed propane-air flame propagation in the duct has been examined.

The analytical works published by other research groups were also modified for the rectangular channel, and the results employed as another datum for validation of experimental and numerical results.

Acknowledgements

First and foremost, I would like to acknowledge and thank my supervisor, Prof. Andrzej Sobiesiak who provided me with invaluable advice and support throughout my Ph.D. studies. The experiences that I have been afforded while in his research group have been second to none, and I have always been given the opportunity to test my own hypotheses and to be creative. I sincerely and truly thankful for all the commentaries and guidance provided to my research throughout the past five years.

I would also like to thank my doctoral committee members, Prof. Ronald Barron, Prof. Gary Rankin, Dr. Jeff Defoe, and Prof. Cecile Devaud, for their feedback and recommendations regarding this dissertation.

This research would not have been possible without the financial contributions from the AUTO21 and the University of Windsor Faculty of Graduate Studies.

The bulk of the numerical simulations were conducted on the Compute Canada and Sharcnet supercomputing facilities, and assistance from staff at both these facilities is much appreciated. Moreover, I would like to thank CD-adapco Company and Star-CCM+ support team.

I appreciate the support and friendship of the other research group members: Indika Gallage, Xisheng Zhou, Dr. Iain Cameron, Tony Nguyen, Jeff Canape, Steven Dal Bello, Luka Celic and Dale Haggith.

I am eternally grateful to my parents, Ali and Ziba, who have supported and encouraged my academic endeavors. I owe them forever. I am also grateful to my brother, Yazdan, for his love and kind moral support.

Finally, I would like to acknowledge my beloved wife and life companion, Sahar. Thank you for being on my side, with your unconditional love and support.

Dedicated to my parents,

Ali Movahedi

and

Ziba Mozaheb

Contents

List of Figures

List of Tables

Nomenclature

C_p	Specific heat at constant pressure
C_v	Specific heat at constant volume
D	Mass diffusivity
Da	Damkohler number
E	Energy
Ka	Karlovitz number
k	Turbulent kinetic energy
L	Characteristic length
Le	Lewis number
l_k	Kolmogorov length scale
l_0	Integral length scale
$\dot{m}$	Mass flow rate
Nu	Nusselt number
P	Pressure
Pr	Prandtl number
Q	Heat energy
R	Gas constant
Re	Reynolds number
Re_T	Turbulent Reynolds number
S_l	Laminar flame speed
S_l^0	Unstrained laminar flame speed
T	Temperature
T_{wall}	Wall temperature
t	Time

C_p	Specific heat at constant pressure
T_{AFT}	Adiabatic flame temperature
T_{amb}	Ambient temperature
$\acute{u}$	RMS velocity fluctuations
U	Velocity
α	Thermal diffusivity
δ	Flame thickness
ϵ	Turbulence dissipation rate
μ	Dynamic viscosity
ν	Kinematic viscosity
ρ	Density
ρ_b	Burned gas density
ρ_u	Unburned gas density
τ	Time constant
Φ	Air/fuel equivalence ratio

Abbreviations

AFR	Air-to-Fuel Ratio
BML	Bray-Moss-Libby
CC	Correlation Coefficient
CFD	Computational Fluid Dynamics
DAQ	Data Acquisition System
DDA	Digital Differential Analyzer
DDT	Deflagration to Detonation Transfer
EBU	Eddy Break-Up
FPD	Flame Propagation Duct
FSC	Flame Speed Closure
LES	Large Eddy Simulation
LIC	Line Integral Convolution
TFC	Turbulent Flame Closure
TFM	Thickened Flame Model
TTL	Transistor-Transistor Logic
RANS	Reynolds-Averaged Navier–Stokes
RMS	Root Mean Square
PEBU	Premixed Eddy Break-Up

Units

%	Percent
°	Degrees (temperature)
atm	Atmosphere
C	Celsius
fps	Frames per Second
K	Kelvin
mm	Millimetre
cm	Centimetre
m	Metre
m/s	Metre per Second
L	Litre
g	Gram
kg	Kilogram
Pa	Pascal
kPa	Kilopascal
MPa	Megapascal
s	Second
ms	Milli-Second
Hz	Hertz

Chapter 1

1 Introduction

1.1 Overview and background

Premixed flame propagation in tubes and ducts, at different opening conditions, have been studied for about a hundred years [1, 3, 5, 7, 8, 9, 10, 11, 12, 13, 14, 15, 16, 17, 18, 19]. A broad scope of theoretical concepts and applications such as micro-propulsion on light-weight spacecraft, gas explosion dynamics, deflagration to detonation transition (DDT), and specifically internal combustion engines were the main areas of focus in these studies. Other reasons for numerous experimental, numerical and analytical works on this topic are the elaboration of premixed flame propagation in a tube or duct from the ignition, laminar flame development, flame-boundary interactions, flame-pressure wave interplay and the transition to turbulent flame. The experiments done by Ellis [1] in a closed duct showed that the flame shape undergoes a radical change in curvature with an aspect ratio greater than two. After ignition, the flame expands spherically until it approaches the top and bottom walls. The flame then takes on an elliptical shape as the portions that are nearing the top and bottom walls slow down. When the flame reaches these walls, it is quenched and the flame surface area decreases. This causes the flame to slow since a lower flame area results in less burning and therefore cooler expanding gas. Salamandra et al. [20] called this a 'tulip flame'.

The tulip flame formation can depend on many factors such as the geometry of the combustion chamber, flammability limits of the mixture, equivalence ratio, initial pressure and temperature, and outlet opening ratio [15, 21]. Clanet and Searby [14] have studied the transition to a tulip flame and explained this as a manifestation of the Rayleigh–Taylor instability. Zero Mach number numerical simulations

disprove the pressure wave effects as the main reason for tulip formation [15, 22]. Instead, they suggested parameters such as wall boundary conditions, mixture composition, and combustion chamber geometry as effective factors. A numerical simulation (2D – Thickened flame model) by Gonzales et al. [23] questioned the wall friction effect on tulip flame formation. Instead, they determined the Darrieus–Landau (DL) instability and the transverse velocity gradient as important elements. The same conclusion regarding the wall friction effect was reported by Marra and Continillo [22]. An earlier explanation by Guenoche [24] postulated that the tulip flame is caused by pressure wave interactions that have reflected off the end wall. The pressure waves are generated during initial flame propagation and then reflect off of the closed end of the tube and interact with the flame.

Many experiments and numerical studies have focused on the impacts of the vortices in the vicinity of flame front, on the tulip flame formation [8, 10, 11, 25, 26, 27, 28]. Matalon and Metzener [10, 29] concluded that vortical motion in the burned gas caused by the produced vorticity at the flame front creates the tulip flame. Their work also described why the DL instability cannot be considered as the main and only reason for tulip flame creation. This is not in contrast with the possibility of flame front inversion initiation by DL instability determined by Matalon [30] and Chomiak [31].

Zhou et al. [11] reasoned that tulip flame formation is due to the interaction between the flame front and flame-induced flow. Once the flame front begins to flatten, the interaction results in an uneven force distribution mainly due to dynamic pressure. This force distribution causes the forces near the corner sections to be greater than the middle of the flame front. As a result, the corner sections propagate faster thus covering more distance than the middle section, thereby facilitating the formation of a tulip flame. Xiao et. al [8] postulate the same theory regarding the tulip flame formation in his recent work. They described this mechanism through

experiment and 2D numerical simulation more comprehensively. They concluded that the reverse flow due to vortex motion behind the flame front in addition to an adverse pressure gradient causes the tulip flame initiation. The Rayleigh–Taylor (RT) instability created by pressure waves generated by the flame –wall interaction have a role but this is not a vital factor.

Bychkov et al. [12], proposed an analytical model to predict the time and location of the flame front at three different stages from ignition to tulip flame development. They found that these steps are independent of the Reynolds number.

A one-step global reaction model [32, 33] and level set method [31] were used in previous numerical studies. The reactions are treated as a one-step chemical reaction model, whereas in the level set method, the G-equations are solved and therefore the flame front would gain [31]. The "G" is defined as a non-reacting scalar and the G-equation is a premixed flame-front tracking model based on kinematics approach. A flame front is modeled as an infinitely thin interface denoted into either a burned and unburned region. Each of these regions has a spatially uniform density and the motion of the flame interface is traced in the zero Mach number model [33]. One significant advantage of the G-equation formulation of turbulent premixed flames is the absence of chemistry source terms in the transport equations. As a consequence, the turbulent flame speed plays a crucial role as a predetermined input.

Sobiesiak et al. [34] investigated flame propagation experimentally in a rectangular duct with a varied cross section aspect ratio, mixture composition, and an open end exit. They observed that the tulip flame formed almost always at the same distance from the spark end. In addition, several other flame formations were observed after the tulip flame formation, which they have called inversions. Furthermore, the flame itself is not moving at a constant speed and periodically accelerates and decelerates (a leap frog phenomenon).

In the numerical simulation of premixed reacting flow, it is computationally expen-

sive to resolve the flame front on the computational grid because the flame thickness is very thin, normally a fraction of a millimeter. Several methods are commonly used to overcome this difficulty, such as simulation of an artificially thickened flame, the use of a flame front tracking technique based on the G-equation and the use of a filtered progress variable with a reaction rate depending on flame surface density [35, 36].

Schmidt et al. [37] investigated on open outlet case experimentally and showed as a flame continues to propagate down the tube it goes through a transition from laminar to turbulent.

Propagation of the flame in the mostly turbulent premixed propane/air mixture ahead of the flame front, specifically after the tulip flame has formed, brings in the idea for testing the capability of a turbulent combustion model for simulation of this phenomena.

1.2 Research objectives

The primary objectives of this research were as follows:

a. Through experiment:

I. Gain insight into premixed propane-air flame propagation in a long rectangular duct for two different outlet conditions; fully opened end and fully closed end cases. In particular;

Ia. Establish the flame behavior (speed and shape) before, during and after the tulip flame formation point;

Ib. Explore the flame shape and speed after the tulip flame collapse which is defined as "first flame inversion and/or subsequent flame inversions" for the purposes of this work;

Ic. Study the outlet condition effects on the flame behavior at the tulip flame point and afterward.

b. Through analytical modeling:

I. Employ the modified version of works by Clanet et al. [14] and Bychkov et al. [12], to examine their capability to predict the flame front location and time at different steps of flame propagation in our case study;

II. Compare the results from this method with two other schemes (experimental and numerical methods).

c. Through numerical modeling:

I. Examine different premixed combustion model capability for the simulation of propane-air premixed flame propagation in the duct. This includes the tulip flame and the flame subsequent inversion modeling.

II. Explore the causes for tulip flame and subsequent inversion/inversions and highlight possible differences/similarities between these causes.

1.3 Differences from other works

- There is no other individual study that has dealt with the subsequent inversion/inversions in either opened or closed end outlet conditions. The creation of subsequent inversion/inversions, their causes, and effects on the flame propagation speed had required further investigation.

- Earlier studies were performed in short to medium length size (mostly shorter than 0.6 m) or in long channels to monitor detonation. The duct length which is used in this study (1.8 m) was not employed by any other research group. This

length was selected in a way that could capture the initial and middle stages of the flame movement while providing the possibility of monitoring the flame prior transition to detonation.

- In previous works, the tube and square cross-section duct have been used. The significance of this study is that it employs the rectangular cross-section duct which delivers the monitoring capability for flame behavior at a non-unity aspect ratio in comparison with the former studies.

- Numerical modeling for the above-mentioned length size (about 1.8 m) and rectangular cross-section duct have not been investigated in the past. Thus simulation of such case may pose a number of difficulties in terms of the mesh size, mesh numbers, the running time and the flame feeding flow state which switches between laminar and turbulent conditions interchangeably.

- The flow-flame and flame-wall interactions experience varied conditions of the fresh gas introduced via feeding flow as it moves through the duct. These interactions in relation to the tulip flame creation and the subsequent flame inversions have been extensively explored in this work.

1.4 Significance of the study

- Several interpretations were proposed for the premixed flame propagation movement and the tulip formation in the channel. However, the reasons behind the tulip flame and possible subsequent inversion/inversions are still not clearly understood. This work attempts to summarize, explain and conclude the causes for these aforementioned points.

- Different experimental trials with the same operating condition have acceptable repeatability for the tulip flame formation zone. In fully open end outlet

condition, the subsequent inversion/inversions are not equally repeatable from one experiment run to another due to the chaotic effect of turbulence at this zone. This will be discussed in later chapters. This work tries to solve this issue by using a numerical method.

- There are some qualitative similarities between the flame propagation in the duct/tube and the flame propagation inside of the cylinder in an internal combustion engine. These include kernel flame growing, flame-wall interaction and flame-flow interplay. Also, study of the flame movement in engine cylinder is not easy due to the different types of restriction. Therefore, transferring this scenario to the duct/tube can eliminate these limitations.

- There are many direct applications of this study:

  I. The flame propagation in the opened end outlet channel has applications in the flame development and propagation in coal mines from a hazard and safety point of view.

  II. Transport of grain in an elevators piping and mine shaft. When the grains have been transported in the elevator, due to the friction between the grains, there is a creation of dust with air mixture and this mixture is flammable. If that mixture starts burning, the flame propagation onsets. The mine shaft follows similar theory. The coal dust mixes with air and creates the flammable mixture.

- Specific trends of flame movement in the open end outlet and long channel, provides a great capacity to examine numerical models such as the flame speed closure (FSC) model. The FSC model claims to have the ability to capture both laminar and turbulent combustion conditions. The model has been verified before by Yasari [38] for the stationary premixed flame. This case study, and specifically the opened end outlet case, offers a valuable opportunity to test

this model for the moving premixed laminar to turbulent changing flame (see Figure 1.1). Obtained results can help extend the FSC model application to internal combustion engines for future work.

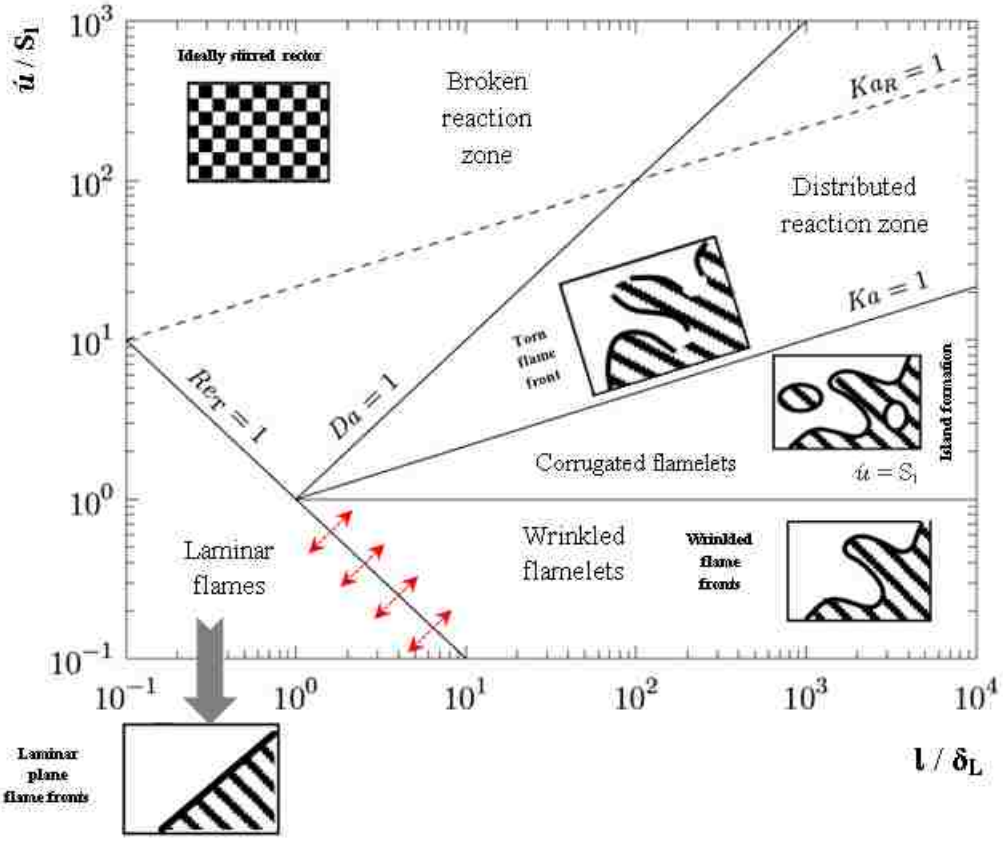

Figure 1.1: Regime diagram for premixed combustion (Adapted from Warnatz et al. [2], Peters [4] and Borghi [6]). The red arrows on the $Re_T = 1$ line (laminar region border), highlight our initial forecast regarding flame propagation in the channel, especially for the opened end outlet case. It is expected the flame to cross this border repeatedly within its movement through the duct.

- In some research, the flame propagation in a channel with an obstacle has been used to validate the turbulent premixed numerical model. This work considers the complexity involved in flame propagation in a long duct, which proposes an alternative and more extensive approach for validation of the numerical turbulent/laminar model.

1.5 Organization of dissertation

The organization of the remainder of this document is as follows:

- Chapter 2: explains in detail the experimental setup which is used in this study, describing the experimental procedures, data extraction methodology and sources of error.

- Chapter 3: provides a "brief overview" of the numerical methodology, which includes initial conditions, the semi-laminar combustion model (from Star CCM+), the turbulent combustion models (XiFoam and TFCFoam in this study) and the one that can catch/switch between laminar and turbulent combustion states (FSCFoam in this work). Moreover, a thickened flame model (TFMFoam) is presented in this chapter.

- Chapter 4: explores the analytical scheme which is comprised of the available and adopted analytical and empirical equations (for this work) to predict the premixed flame movement in the duct.

- Chapters 5-10: present the results from all three chapters (2-4). Discussion of the possible similarities and differences between the results is provided.

- Chapter 11: a summary of the presented work with major findings, conclusions, and potential future works.

Chapter 2

2 Experimental method

2.1 Experimental apparatus

The experimental apparatus used is shown in Figure 2.1. The apparatus consists of major components: 1- Flame Propagation Duct (FPD), 2- Ignition site, 3- Mixture preparation cylinders, 4-High speed camera, and 5-Pressure transducer.

2.1.1 Flame propagation duct (FPD)

Experiments are carried out in the rectangular cross section duct that has an aspect ratio of 25.4 mm x 50.8 mm and length of 1800 mm (Figure 2.1). The duct is machined out of aluminum with steel clamping bars and it is sealed with O-ring cord. The end-plate at one of the ends (spark end) featured a threaded opening for a centrally mounted spark plug. The surface area of the exit end of the duct can be varied to provide from 0% to 100% open area. The smaller side wall is made of transparent material to allow recording of the flame propagation inside of the duct.

Flushing of the burnt gas and filling with the fresh mixture is done through a gas manifold. The duct internal pressure is measured by an Omega 4-digits absolute pressure gauge.

2.1.2 Ignition site

The ignition is triggered by a single spark at the duct closed end. The LabVIEW program is used in combination with a data acquisition card (DAQ) for the ignition process. The ignition system includes high voltage transformer, switch, and modified automotive type spark plug. The transformer is similar to the one which is widely used in gas or oil-fired home heating furnace. The operation voltage for this unit is

120 V AC with 20 mA current rate as output. Transferring of electrical discharge to the spark plug occurs through a high-voltage insulated wire. Non-conductive silicone sealant is used to seal the wires, ceramic core and metal casing.

Transistor-Transistor Logic (TTL) type optical switch is used to control the spark. The output signal from the DAQ is used to trigger the spark which signal is managed by a dedicated LabVIEW program.

By using the optical switch, triggering circuit and DAQ board insulation ensures that the electro-magnetic from the spark plug does not interfere with the data collection process.

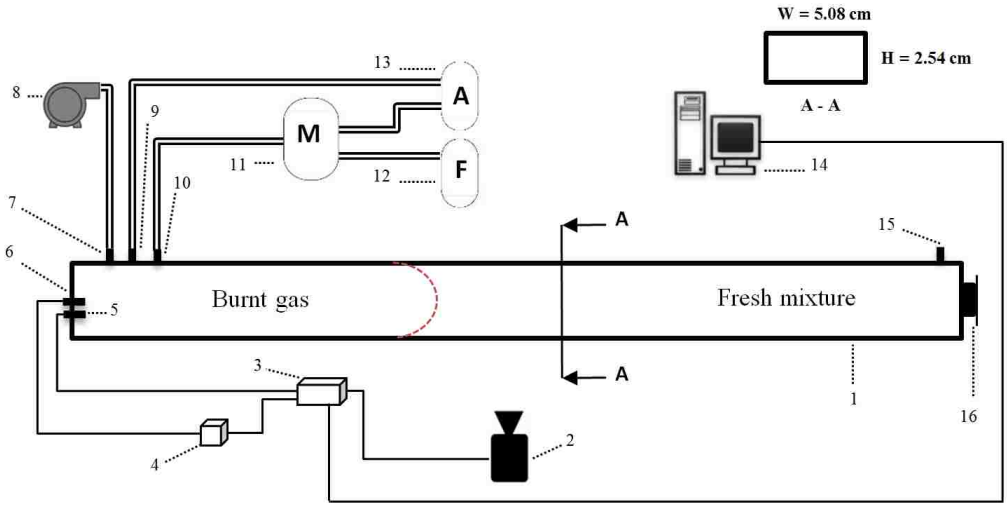

Figure 2.1: Schematic of experimental apparatus: (1) Flame Propagation Duct (FPD), (2) high-speed video camera, (3) connector, (4) optical switch, (5) pressure transducer, (6) spark, (7) vacuum vent, (8) vacuum pump, (9) air valve, (10) mixture valve, (11) mixing (sample) tank, (12) fuel bottle, (13) air bottle, (14) DAQ & data recorder, (15) discharge vent, (16) outlet.

2.1.3 Mixture preparation setup

The flammable mixture at required equivalence ratio is prepared in a separate cylinder using the partial pressure method following these equations:

$$P_{air} = P_{total}\left[1 + \Phi * \left(\frac{F}{A}\right)_{Stoich}\right]^{-1} \tag{2.1}$$

$$P_{fuel} = P_{total}\left[1 + \frac{1}{\Phi * \left(\frac{F}{A}\right)_{Stioch}}\right]^{-1} \tag{2.2}$$

where P_{air} and P_{fuel} are the partial pressure of air and fuel respectively. P_{total} is the total pressure, Φ is the equivalence ratio and $\left(\frac{F}{A}\right)_{Stioch}$ stands for the stoichiometric fuel to air ratio.

A thick walled (2250 ml) cylinder called sample (mixing) tank is installed on the mixture panel (Figure 2.2)and used to mix and store the combustion mixture (air and fuel mixture). The duct is filled to atmospheric pressure with the given premixed propane-air mixture. The mixture is allowed to become quiescent before ignition where the initial temperature is ambient.

An Ashcraft 1082 vacuum and a pressure gauge are used on the mixture preparation panel which has an accuracy of ± 0.25 % (full scale).

Mixture preparation panel also includes a vacuum pump which is utilized to evacuate the sample cylinder and relevant piping ahead of mixture preparation. Ultimate pressure and corresponding errors are 0.2 kPa and 0.2 % respectively.

Two separate high-pressure industrial gas cylinders have been employed to store the fuel (industrial grade 99.5% propane) and the oxidizer (dry air).

Operation requires to decrease the pressure output from each gas cylinder as the maximum operational pressure is 700 kPa (100 psig).

2.1.4 Flame recording

The propagation process is recorded with FASTCAM Mini UX100 high speed camera (Figure 2.3) and processed using ProAnalyst (Version 1.5.7.0). The framing speed is set to 10,000 frames/second (fps). The camera is triggered from the DAQ board

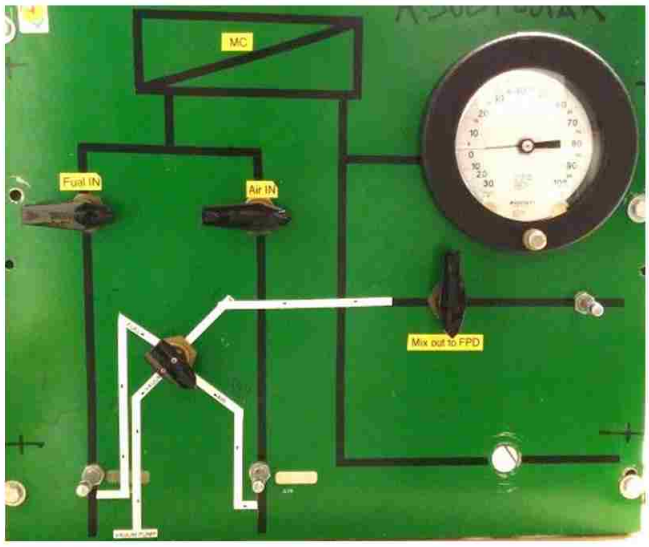

Figure 2.2: Photograph of the mixture preparation panel.

that is generated and managed by LabVIEW.

Figure 2.3: Photograph of Photron FASTCAM Mini UX100 high speed camera.

2.1.5 Pressure measurement

A Kistler (6117B) pressure transducer is mounted at the spark end in order to trace the dynamic pressure in the duct during flame expanding. This sensor can measure pressure up to 200 bars and it has the linearity of ± 0.6 % (full scale). DAQ board has been used again to collect data from the pressure transducer.

2.2 Experimental procedure

a) Mixture preparation

- Select the equivalence ratio(Φ).
- Calculate appropriate amounts of fuel and air pressure using the Equations 2.1 and 2.2. The total mixture pressure value should be considered as 6.89 bar (100 psi).
- Vacuum the mixing cylinder.
- Transfer the required amount of fuel to the mixing cylinder.
- Add the required air until reaching the total mixture pressure value.

The mixture is required to settle in the mixing tank for about 1-2 minutes. During this process FPD setup should be completed. Leaving the mixture over an extended period of time can cause stratification of the mixture.

b) FPD setup

- Plug in the spark triggering system.
- Turn on the room exhaust.
- Close the FPD end-plate and the discharge vent.
- Evacuate the FPD using the vacuum pump.
- Fill the FPD with the prepared mixture to a pressure of 1 bar (14.7 psi).
- Leave the mixture to settle in FPD for about 1 minute.
- Open the discharge vent.
- For the open end test, open the FPD end-plate.
- Turn off the lights.

- Trigger the spark, camera, and pressure data acquisition by clicking on 'Play' at LabVIEW program (FPD-Test.vi).
- Turn on the lights.
- Remove the burnt gas in the FPD using the air flush. This prepares the FPD ready for the next test.

c) Camera setup

- Mount the camera to tripod at the FPD level.
- Set the camera position to proper distance (approximately 2m) away from the duct.
- Make sure that all camera cables, power supply, and connector cable are connected.
- Adjust the camera field view in a way that it can view and focus the full duct (from the spark to the outlet).
- Set the frame rate to 10,000 fps.

The camera starts recording once the spark is initiated.

2.3 Image processing

The image processing is done through analysis of AVI recorded files using ProAnalyst (Version 1.5.7.0). In experiments, images are saved every 0.1 ms at 10,000 fps. The flame location is defined through a light intensity when it exceeds a certain threshold. The first white pixel locates the ignition point on the images. The duct centre-line is defined as the X-axis and the ignition electrode tip is chosen as the axis origin.

ProAnalyst line tracking feature helps to trace the luminous flame front movement. Based on the grey scale images pixel format, each pixel has a value between 0

(100% white cell) and 256 (100% black cell). By defining a certain threshold (for instance 10), then the value of each pixel is converted to 0 or 1. In other words, either 0 or 1 is assigned to those pixels which have a value below and above the threshold respectively. Therefore the matrix composed of zeros and ones is created.

The pixel numbers between the duct end and the flame front are counted. Knowing the numbers of the pixel for entire duct length, the pixels between the ignition point and the flame front can be calculated. Conversion of the pixel to length can be done through mm/pixel scaling (which is computed separately by dividing the duct actual width to its allocated pixel numbers).

This procedure creates the table with two main columns. The first column states the time from the ignition and the second column shows the relevant flame front location referencing to the spark plug.

2.4 Flame speed calculation

The absolute flame speed (instantaneous flame propagation speed) at the duct centre-line is calculated from the flame images. The table obtained in the previous section (2.3) is utilized to compute the absolute flame speed (AFS) through the equation below:

$$AFS_n = \frac{X_n - X_{n-1}}{t_n - t_{n-1}} \tag{2.3}$$

where X_n and X_{n-1} are the flame front locations at times t_n and t_{n-1} respectively.

2.5 Error sources

McKeller [39] has done his Master thesis with the same experimental setup. He calculated all relevant uncertainty regarding this rig on Appendix B of his thesis. The same setup has been used in this study. Therefore, the McKeller [39] uncertainty

calculations can still be valid.

The main source of error is attached to the equivalence ratio determination and mixture preparation. Based on McKeller [39] work, the equivalence ratio uncertainty is about $\pm$ 0.06. This can cause an issue on the differentiation of the results between equivalence ratio 1.0 and 1.1.

The repeatability of the results, especially after the formation of tulip flame is somewhat questionable. Therefore, it is required to repeat each case for many times (about 30 runs) in order to reach proper statistical assessment. This non-repeatability (as if will be discussed in Chapter 5) originates from the chaotic nature of generated unburned mixture flow which in turn highlights the main reason for the numerical modeling of this phenomenon.

Processing of the flame recorded images to extract the flame front speed also involved uncertainties. A certain threshold of the line intensity is utilized to define the flame front location, the process may be within one or two pixel/pixels (about 3-6 mm) of the actual flame front.

Chapter 3

3 Numerical modeling

3.1 Numerical codes

Numerical modeling in conducted with two different codes:
a) Star CCM+ 10.02.012-R8 which is commercial CFD software with widespread use in industrial problems and it has the capability of tackling multi-physics and complex geometry. It also has an established reputation for producing high quality solving (pre-processing, solving and post-processing) in a single code.
b) OpenFOAM 2.2.2 (Open Field Operation and Manipulation) which is an open source CFD software package. Commercial and academic organizations have increased their attraction to the OpenFOAM libraries over recent years.

3.2 Numerical scheme and initial conditions

The finite volume method is employed to discretize the governing equations. For Star CCM+ case, the unsteady formulation is solved by a first order implicit scheme. The time step is calculated following the Courant-Friedrichs-Lewy criterion ($\Delta t = 5e^{-7}$ second). The 2D geometry (H = 2.5 cm and L = 160 cm) is employed. It consists of 3 walls at top, bottom and left sides. A "pressure outlet" boundary condition is set for fully opened outlet case (right edge). A uniformly structured grid is adapted to grid size 0.5×0.5 mm. The total number of cells is 160,000. This simulation is required about 2 weeks running time using 20 parallel cores (CPUs) and 20 GB of memory on SHARCNET computing nodes.

Regarding OpenFOAM models, the finite volume method is also utilized to discretize the governing equations. A second order upwind scheme for convection terms and second order central differencing scheme for the diffusion terms are employed.

The first order implicit scheme is applied as the time scheme for the RANS cases. Regarding the LES cases, the unsteady formulation is solved by a second order implicit scheme. Considering a Courant-Friedrichs-Lewy criterion, the base time step is defined as 1e-7 s but time modifiable is used to reduce the whole calculation time. Three different geometries, 3D, 2D and Semi-2D (3D case with W=1 mm) have been used. In the 3D case, a quarter of actual geometry with two symmetrical edges (bottom and back), three walls (front, top, and left) and one patch (outlet) at right have been utilized. Regarding the 2D case, the front and back are set to empty. For the model accompanied with dynamic mesh, the initial grid size is set to be 1×1 mm. This grid size modifies to 0.2×0.2 mm at the flame zone during the calculation. Employing this adaptive mesh method reduces the simulation time considerably. For 3D-RANS cases, the total number of cells before modification is 2,000,000. This number can increase up to 3,000,000 cells after the modifications during simulation time. Therefore, about 2 weeks running time using 30 parallel cores (CPUs) and 30 GB of memory on SHARCNET computing nodes is required. Regarding 2D-RANS cases, the mesh numbers change between 40,000 at simulation starting point and it can increase by 200,000 cells during the flame propagation. The running time is 3 days, using 16 parallel cores (CPUs) and 16 GB of memory. The 5 layers of the prism mesh have added close to the top and bottom sides of the wall for 2D-LES cases. An "inletOutlet" boundary condition is set for fully opened outlet case.

As mentioned in the previous chapter, the actual duct length is equal to 1.8 meters as in the experiment. Due to the high fluctuation of the flame front surface in the last 20 cm of the duct, the image processing of experimental results was not possible in this zone. Moreover, the initial numerical modeling results show that the last 20 cm of this geometry does not affect the final results. Therefore, the length in numerical modeling is considered as 1.6 m.

The ignition position is located at the left end. The wall temperature is defined

as constant at 300K and initial pressure is set to 1 atm. Non-slip and adiabatic boundary conditions are adopted at the duct walls. The reaction of propane/air mixture is taken into account using a single-step global kinetics. This is due to the importance of flame front tracking rather than the detailed study of involved species (reactants and products) in this study.

3.3 Laminar combustion model

Earlier works have shown that the initial stages of premixed flame propagation in a tube can be well modeled using a 2D numerical approach [25]. However, the application of the commercial code to model flame propagation in a tube or duct is not reported in publications. The combustion model available in Star CCM+ 10.02.012-R8, 2D Premixed Eddy Break-up model (PEBU) is employed to simulate the flame propagation. If the reaction rate is limited to the Arrhenius form, the model would be able to employ for the laminar flame case. In the other words, the reaction rate would not be affected by turbulence characteristic of flow and it is only calculated based on chemical properties.

3.3.1 Governing equations

The governing equations consisting of continuity equation, momentum, energy (reduced temperature equation in this case), species and ideal gas state equations are as follows:

$$\frac{\partial \bar{\rho}}{\partial t} + \frac{\partial}{\partial x_j}\left(\bar{\rho}\tilde{u_j}\right) = 0 \tag{3.1}$$

$$\frac{\partial}{\partial t}\left(\bar{\rho}\tilde{u_j}\right) + \frac{\partial}{\partial x_j}\left(\bar{\rho}\tilde{u_j}\tilde{u_i}\right) = -\frac{\partial \bar{P}}{\partial x_i} + \mu\frac{\partial^2 \tilde{u_j}}{\partial x_j \partial x_i} - \frac{\partial \tau_{ij}}{\partial x_j} \tag{3.2}$$

where the Reynolds stress tensor is: $\partial\tau_{ij} = \widetilde{\bar{\rho}u_j'' u_i''}$

$$\frac{\partial \bar{\rho}\widetilde{\theta}}{\partial t} + \frac{\partial}{\partial x_j}\left(\bar{\rho}\tilde{u_j}\widetilde{\theta}\right) = \frac{\partial}{\partial x_j}\left(\bar{\rho}\bar{D}\frac{\partial \widetilde{\theta}}{\partial x_j} - \bar{\rho}\widetilde{u_j''\theta''}\right) + \bar{\dot{W}}_\theta \tag{3.3}$$

where the reduced temperature (regress variable) is: $\theta = \frac{T-T_b}{T_u-T_b}$

$$\frac{\partial}{\partial t}\left(\bar{\rho}\widetilde{Y_m}\right) + \frac{\partial}{\partial x_i}\left(\bar{\rho}\tilde{u_i}\widetilde{Y_m}\right) = \frac{\partial}{\partial x_i}\left(\bar{\rho}\bar{D}_m\frac{\partial \widetilde{Y_m}}{\partial x_i}\right) + \bar{\dot{W}}_m \tag{3.4}$$

$$P = \bar{\rho}RT \tag{3.5}$$

where t is the time, ρ is the density, P is the pressure, u_i is the velocity component, μ is the viscosity, T is the temperature, $\bar{\dot{W}}$ is the reaction rate and R is the gas constant of the mixture. For species m, Y_m is the mass fraction and D_m is the diffusivity coefficient. The overbar and tilde denote Reynolds and Favre averaging respectively.

3.3.2 Premixed Eddy Break-up model (PEBU)

In the PEBU model, a fuel mass fraction is tracked by transport equations. The mean species concentrations are calculated as functions of the mean fuel mass fraction and a one-step global reaction scheme which is determined based on the unburnt gas composition. The mean enthalpy can be obtained by solving a mean enthalpy transport equation. Knowing the mean enthalpy and species concentration, the mean density and temperature can be calculated. By choosing the reaction control as kinetic only, it is assumed that the reaction rate is dictated solely by finite-rate chemical kinetics (Arrhenius form). This makes the model suitable for laminar flow simulation.

$$\bar{\dot{W}}_\theta = -A_n T^{\beta_n} \prod all - reactants \left(\frac{\bar{\rho}Y_m}{M_m}\right)^{P_{mn}} e^{-\frac{E_{an}}{R_u T}} \tag{3.6}$$

where A_n, β_n, E_{an} and p_{mn} are the pre-exponential factor, temperature exponent, activation energy for the n^{th} reaction and rate exponents of reacting species (dimensionless), respectively, and R_u is the universal gas constant [40].

3.4 Turbulent combustion model

XiFoam is the embedded model for the simulation of premixed/partially premixed turbulent combustion in OpenFOAM. Both Reynolds-Averaged Navier-Stokes (RANS) and Large Eddy Simulation (LES) turbulent models work with the XiFoam model. Xi ($\equiv \Xi$) is the flame-wrinkling (dimensionless - surface function) which is defined as:

$$\Xi = \frac{S_t}{S_l} = \frac{A_T}{A} \tag{3.7}$$

where S_t is the turbulent flame speed, S_l is the laminar flame speed, A_T is the total flame surface and A is the flame cross section area.

The application of this turbulent model would generally provide better results with 3D cases. Therefore, 3D geometry is employed in this model. A quarter of the duct, limited to the two symmetrical plane and two walls are modeled.

3.4.1 XiFoam and governing equations

XiFoam is the turbulence model for simulating compressible premixed combustion. The general governing equations are consisting of conservation equations of mass, momentum, energy, species and ideal gas state. In contrast the XiFoam model follows Bray-Moss-Libby (BML) approach and it assumes the temperature on the burned side is predefined. Therefore, there is no need to solve the energy equation as the flame front propagation is modeled by solving a Favre-averaged transport equation for mean reaction regress variable:

$$\frac{\partial}{\partial t}\left(\bar{\rho}\tilde{b}\right)+\nabla.\left(\bar{\rho}\tilde{u_i}\tilde{b}\right)-\nabla\left(\frac{\mu_t}{S_{ct}}\nabla\tilde{b}\right)=-\bar{\rho}S_l\Xi|\nabla\tilde{b}| \tag{3.8}$$

where t is the time, ρ is the density, u is the velocity, μ_t is the turbulent viscosity, S_{ct} is the turbulent Schmidt number ($=\mu/\rho D$), D is the diffusion coefficient, and b is the regress variable:

$$b=1-c \tag{3.9}$$

where c is the progress variable:

$$c=\frac{T-T_u}{T_b-T_u} \tag{3.10}$$

where b stands for burned gas, and u stands for unburned (fresh) gas.

3.4.2 Xi calculation methods

XiFoam model uses the b-Xi two-equation model in which Xi could be obtained by either the solution of the Xi transport equation or employing an algebraic expression. In this work, both methods are based on Gulder's [41] flame speed correlation.

The algebraic method calculates the Xi based on below equations [42]:

$$\Xi^*_{eq}=1+X_iCoef\sqrt{\frac{\acute{u}}{S_l}}R_\eta \tag{3.11}$$

$$\Xi_{eq}=1+2\left(X_iShapeCoef-b\right)\left(\Xi^*_{eq}-1\right) \tag{3.12}$$

where $\acute{u}$ is the turbulence intensity and R_η is the Kolmogorov Reynolds number. X_iCoef (=0.62 in this study) and $X_iShapeCoef$ are input data. The assumption of local equilibrium ($\Xi=\Xi_{eq}$) has been considered in this method for the sake of simplicity.

In transport method the following equation should be solved along with Equation 3.8:

$$\frac{\partial \Xi}{\partial t} = \widetilde{U_S} .\nabla \Xi = G\Xi - R\left(\Xi - 1\right) + \left(\sigma_S - \sigma_t\right)\Xi \tag{3.13}$$

where:

$$R = \frac{0.28}{\tau_\eta} * \frac{\Xi^*_{eq}}{\Xi^*_{eq} - 1} \tag{3.14}$$

$$G = R\frac{\Xi_{eq} - 1}{\Xi_{eq}} \tag{3.15}$$

$$\sigma_t = \left(\widetilde{U} + S_l \Xi \widetilde{n}\right) - \widetilde{n}.\left[\nabla\left(\widetilde{U} + S_l \Xi \widetilde{n}\right)\right].\widetilde{n} \tag{3.16}$$

$$\sigma_s = \frac{\nabla.\widetilde{U} - \widetilde{n}.\left(\nabla \widetilde{U}\right).\widetilde{n}}{\Xi} + \frac{\left(\Xi + 1\right)\left\{\nabla.\left(S_l \widetilde{n}\right) - \widetilde{n}.\left[\nabla\left(S_l \widetilde{n}\right)\right].\widetilde{n}\right\}}{2\Xi} \tag{3.17}$$

$$\widetilde{U_S} \approx \widetilde{U} + S_l \frac{\widetilde{n}}{\Xi} \tag{3.18}$$

where τ_η is the Kolmogorov time scale, $\widetilde{U}$ is the density weighted ensemble average velocity and $\widetilde{n}$ is the flame unit normal. Unlike the algebraic approximation, the direct effects of strain are considered in the transport method.

3.4.3 Calculation of laminar flame speed in equilibrium with the applied strain

In this scenario, three different models are available to calculate the laminar flame speed with the applied strain effect including unstrained, equilibrium and transport. For the unstrained case the laminar speed remains unchanged:

$$S_l = S_l^0 \tag{3.19}$$

where S_l^0 is the unstrained laminar flame speed which is computed based on Gulder correlation [41] in this study. Equilibrium case is estimated based on the idea of the balancing between the local deformation rate and the laminar flame speed:

$$S_l^\infty = S_l^0 max\left\{1 - \frac{\sigma_S}{\sigma_{Ext}}, 0\right\} \tag{3.20}$$

where σ_{Ext} is the strain rate at extinction. For the transport case:

$$\frac{\partial S_l}{\partial t} + \widetilde{U_S}.\nabla S_l = -\sigma_S S_l + \sigma_S S_l^\infty \left\{\frac{S_l^0 - S_l}{S_l^0 - S_l^\infty}\right\} \tag{3.21}$$

when the chemical time scale and the strain rate time scale is such that $t \to \infty$,$S_l \to S_l^\infty$.

3.4.4 XiDymFoam model

Three-dimensional simulations always deal with time and cost. Employing adaptive grids can reduce these defects. In this regard, the XiFoam model is coupled with the OpenFOAM dynamic mesh (dynamicFVMesh.H) library. The new model is named "XiDymFoam". The base grid size is refined at the flame region which is separately defined by the Xi (or temperature) margin. These refinements expand gradually from the flame section to the both sides of fresh and burnt gasses.

3.4.5 Ignitor model

In OpenFOAM, the ignitor is modeled by the below equation:

$$Ignitor \equiv \frac{\left[\frac{(Ignitor-Strength)*(Cell-Volumes)*\rho_u}{(Ignitor-Duration)}\right]}{b + 0.001} \tag{3.22}$$

where Ignitor-Strength, Ignitor-Duration, and Cell-Volumes (ignitor size) can be defined by the user. The ignitor effect on the regress variable equation (b-Equation) is computed by:

$$(b - Equation) = (b - Equation) + Ignitor \tag{3.23}$$

3.5 Flame speed closure model (FSC)

The flame speed closure model proposed by Lipatnikov [43] . This model is modified based on the turbulent flame speed (TFC). TFC is the RANS turbulent combustion model which is firstly suggested by Zimont and Lipatnikov [44]. In TFC model the progress variable (regress variable) computes through solving single transport equation. Zimont and Lipatnikov [44] enclosed the two terms on the right hand side of the progress variable Equation 3.24 by introducing below Equation 3.25 :

$$\frac{\partial \widetilde{\bar{\rho}c}}{\partial t} + \frac{\partial}{\partial x_j}\left(\bar{\rho}\tilde{u}_j\widetilde{c}\right) = -\frac{\partial}{\partial x_i}\left(\overline{\rho u_j'' \theta''}\right) + \widetilde{\bar{\rho}W} \tag{3.24}$$

$$\frac{\partial \widetilde{\bar{\rho}c}}{\partial t} + \frac{\partial}{\partial x_j}\left(\bar{\rho}\tilde{u}_j\widetilde{c}\right) = -\frac{\partial}{\partial x_i}\left(\bar{\rho}D_t\frac{\partial \widetilde{c}}{\partial x_j}\right) + \rho_u U_t|\nabla \tilde{c}| \tag{3.25}$$

where:

$$|\nabla \tilde{c}| \equiv \left\{\sum_{j=1}^{3}\left(\frac{\partial \widetilde{c}}{\partial x_j}\right)^2\right\}^{1/2} \tag{3.26}$$

and for K-εpsilon model:

$$D_t = D_{t,\infty} = \frac{C_\mu}{Pr_t}\frac{\widetilde{k}^2}{\widetilde{\varepsilon}} \tag{3.27}$$

and based on Zimont submodel [45]:

$$U_{t,\infty} = A\acute{u}Da^{1/4} = A\acute{u}\left[\frac{\tau_t}{\tau_c}\right]^{1/4} = A\acute{u}\left[\frac{L/\acute{u}}{k_u/S_l^2}\right]^{1/4} \tag{3.28}$$

D_t is turbulent diffusivity, U_t is turbulent flame speed, K is turbulent kinetic energy, ε is dissipation rate, L is turbulent length scale, Da is Damkohler number, τ_t is turbulent time scale, τ_c is chemical time scale, κ_u is unburned heat diffusivity and Pr_t is turbulent Prandtl number. The constants used in the k-ε model are as follows: $C_\mu = 0.09$, $C_1 = 1.44$, $C_2 = 1.92$, $C_3 = -0.33$, $\sigma_k = 1.0$ and $\sigma_\varepsilon = 1.3$.

There are deficiencies on the application of TFC model for 3D cases. The FSC model promotes by Lipatnikov and Chomiak [43, 46, 47] to overcome these difficulties. The laminar heat diffusivity term $K\frac{\partial \widetilde{c}}{\partial x_j}$ and laminar source term $\frac{\bar{\rho}(1-\widetilde{c})}{t_r(1+D_{t,t}/k_b)}\exp\left(-\frac{\theta}{\widetilde{T}}\right)$ added to the right side of Zimont transport equation (Equation 3.25); therefore the model gets the capability of capturing flame laminar stage:

$$\frac{\partial \bar{\rho}\widetilde{c}}{\partial t}+\frac{\partial}{\partial x_j}\left(\bar{\rho}\tilde{u_j}\widetilde{c}\right)=-\frac{\partial}{\partial x_i}\left(\bar{\rho}\left(D_{t,t}+K\right)\frac{\partial \widetilde{c}}{\partial x_j}\right)+\frac{\bar{\rho}\left(1-\widetilde{c}\right)}{t_r\left(1+D_{t,t}/k_b\right)}\exp\left(-\frac{\theta}{\widetilde{T}}\right)+\rho_u U_{t,t}|\nabla\tilde{c}| \tag{3.29}$$

Where these modifications are done through alerting the turbulent diffusivity and turbulent flame speed equations from the TFC model:

$$D_{t,t} = D_{t,\infty}\left[1-\exp\left(-\frac{t_{fd}}{\tau_L}\right)\right] \tag{3.30}$$

$$U_{t,t} = U_{t,\infty}\left\{1+\frac{\tau_L}{t_{fd}}\left[\exp\left(-\frac{t_{fd}}{\tau_L}\right)-1\right]\right\}^{1/2} \tag{3.31}$$

where θ is activation temperature, K is laminar heat diffusivity, κ_b is unburned heat diffusivity, t_{fd} is flame development time relative to the time of ignition, τ_L is Lagrangian time scale $\left(= D_{(t,\infty)}/\acute{u}\right)$, Da is Damkohler number $(= \tau_t/\tau_c)$, D_t is turbulent diffusivity, $D_{t,\infty}$ is fully developed turbulent diffusivity, $D_{t,t}$ is time dependent turbulent diffusivity, U_t is turbulent flame speed, $U_{t,\infty}$ is full developed turbulent flame speed and $U_{t,t}$ is the time dependent turbulent flame speed.

Considering these changes, the FSC model is capable of switching between laminar and turbulent combustion models. In other words, as the flame reach the laminar fresh gas the turbulent terms $\acute{u} = D_{t,t} = U_{t,t} = 0$ cancel out and the balance equation changes to the one for the laminar flame theory. The application of this model for the stationary flame has been tested by Yasari [48, 49]. In this study because of the initial comparison between the laminar/turbulent combustion model results and the experimental data (check chapter 5) and due to the special behavior of the flame in the duct, it is decide to investigate the application of this model for premixed moving flame.

The TFC and FSC model do not exist in OpenFOAM combustion library. These two models are required to create/modify based on the XiFoam model available in OpenFOAM.

3.5.1 FSCDymFoam model

At this section similar to XiDymFoam model (see 3.4.4), the FSC model is coupled with the open foam dynamic mesh library to create a new model to save time and cost of 3D simulation. This new model is named FSCDymFoam.

3.6 Thickened Flame Model (TFM)

Thickened Flame Model (TFM) provides a method for modeling flames on meshes that are too coarse to resolve the flame structure. This model artificially thickens flames in three-dimensional premixed or partially-premixed gas combustion scenarios. The basic idea of the thickened flame approach is to consider a flame thicker than the actual one, but having the same laminar flame speed S_l^0 [35, 55]. Following simple theories of laminar premixed flame, the flame speed S_l^0 and the flame thickness δ_l^0 may be expressed as:

$$S_l^0 = \sqrt{D\bar{W}} \tag{3.32}$$

$$\delta_l^0 = \frac{D}{S_l^0} \tag{3.33}$$

where D is the molecular diffusivity and $\bar{W}$ the mean reaction rate. Then, an increase of the flame thickness δ_l^0 by a factor F (thickened flame factor) with a constant flame speed S_l^0 is easily achieved by replacing the thermal and the molecular diffusivities α and D by (F$*\alpha$) and (F$*$D), and the reaction rate $\dot{W}$ by $\dot{W}/F$. If F is sufficiently large (in this study F=6), the thickened flame front may then be resolved on the LES computational mesh. The reaction rate remains expressed using an Arrhenius law, as in direct numerical simulations.

The thickening procedure above reduced the Damkohler number D_a to D_a/F, which makes the flame less sensitive to the small turbulent eddies smaller than $F * \delta_l^0$. This subgrid scale effect can be incorporated in the modeling by using an efficiency factor E_f evaluated from the subgrid scale wrinkling factor. The underestimation of the flame front wrinkling by the thickened flame approach can be corrected by increasing the flame speed by the factor E_f.

Therefore, the fuel mass fraction equation or in our case, the regress variable (b) equation would be modified to:

$$\frac{\partial}{\partial t}(\rho b) + \nabla.(\rho \overrightarrow{u} b) - \nabla.(E_f * F * \rho * D * \nabla b) = \frac{E_f * \dot{W}}{F} \tag{3.34}$$

where E_f is calculated from wrinkling factor ratio model by Colin et al. [55] and defined as the ratio between the wrinkling factor (Ξ) of laminar unthickened flame (δ_l^0) to thickened flame (δ_l^l) :

$$E_f = \frac{\Xi \mid_{\delta_l^0}}{\Xi \mid_{\delta_l^l}} \geq 1 \tag{3.35}$$

Here, the wrinkling factor Ξ is calculated from:

$$\Xi = 1 + \beta \frac{\acute{u}\Delta_e}{S_l^0} \Gamma \left(\frac{\Delta_e}{\delta_l^0}, \frac{\acute{u}\Delta_e}{S_l^0} \right) \tag{3.36}$$

where $\acute{u}\Delta_e$ is the local subgrid scale turbulent velocity, Δ_e is the local filter size and β is computed as:

$$\beta = \frac{2 \ln 2}{3 C_{ms} \left(Re_t^{1/2} - 1 \right)} \tag{3.37}$$

where $C_{mc} = 0.28$ and Re_t is the turbulent Reynolds number $\left(= \frac{\acute{u} l_t}{\mu} \right)$.

The function Γ represents the integration of the effective strain rate that is induced by all scales affected due to artificial thickening, and is estimated as:

$$\Gamma \left(\frac{\Delta_e}{\delta_l^0}, \frac{\acute{u}\Delta_e}{S_l^0} \right) = 0.75 \exp \left[-1.2 \left(\frac{\acute{u}\Delta_e}{S_l^0} \right)^{-0.3} \right] \left(\frac{\Delta_e}{\delta_l^0} \right)^{2/3} \tag{3.38}$$

$\dot{W}$ is also computed through Arrhenius reaction rate for one-step propane-air chemistry:

$$\dot{W} = A \nu_F W_F \left(\frac{\rho Y_F}{W_F} \right)^{\nu_F} \left(\frac{\rho Y_O}{W_O} \right)^{\nu_O} exp \left(-\frac{T_a}{T} \right) \tag{3.39}$$

where pre-exponential factor A= 1.65e11 cgs, activation temperature $T_a = 15000$ K, atomic weights of propane ($W_F = 44$) and oxygen ($W_O = 32$), ν_F =0.5 and $\nu_O = 1$.

The "TFM-Foam" model creation and required modifications are done based on "XiFoam" model.

3.6.1 TFMDymFoam model

Similar to the sections 3.4.4 and 3.5.1, the "TFMFoam" model is coupled with dynamic mesh (dynamicFVMesh.H). The new model is named "TFMDymFoam". The base grid size of 1 mm is refined to 0.2 mm at a flame region which is separately defined by the predefined(b) margin. These refinements expand gradually from the flame section to the both sides of fresh and burnt gasses.

3.7 Two-dimensional (2D) dynamic mesh

All above mentioned dynamic mesh models (sections 3.4.4, 3.5.1 and 3.6.1 $\equiv$ XiDymFoam, FSCDymFoam and TFMDymFoam) in the OpenFOAM are genuinely applicable in 3D cases. This is due to the limitation in the dynamicFVMesh file. Some modifications are necessary to adopt these 3D models to 2D. In this work, follows Abdelrahman work [56] and makes new models named "XiDymFoam-2D", "FSCDymFoam-2D" and "TFMDymFoam-2D". Proper 2D geometry with the same length and height as the 3D case has been utilized for these 2D models.

3.8 Large-eddy simulation (LES)

For some of the aforementioned OpenFoam turbulent combustion models, the application of large-eddy simulation is verified in this work. The one equation eddy-viscosity model has chosen to enclose the turbulent terms. The eddy viscosity subgrid scale model is using a modeled balance equation to simulate the behavior of k (turbulent kinetic energy). The k equation coefficients are set to C_k =0.094 and C_e = 1.048 in this study.

3.9 Line integral convolution (LIC) technique

Line Integral Convolution (LIC) is one of the most data visualization methods around. Traditionally streamlines technique is used to investigate the vector flow field. The streamlines are critically dependent on the location which they are placed. Also, complex information turbulent vector field can be missed entirely if the streamlines are not well placed. LIC method which is developed based on the DDA (Digital Differential Analyzer) technique can solve these issues. The DDA Convolution algorithm works in the following way:

1. Each vector in the field is used to define a long, narrow, DDA generated filter kernel that is tangential to the vector and going in the positive and negative vector direction some fixed distance (L).

2. A texture is then mapped one-to-one onto the vector field.

3. The input texture pixels under the filter kernel are summed, normalized by the length of the filter kernel (2L), and placed in an output pixel image for the vector position.

The LIC algorithm is a derivative of the DDA technique that, instead of using a vector, uses a local streamline to generate the filter. The local behavior of the vector field can be approximated by computing a local streamline that starts at the center of the pixel and moves out in the positive and negative directions [57]. It's dropping paint in a river to see how the current is flowing: to visualize a vector field simply take an image and have the vector field smear the colors. The result is a powerful alternative to using arrows or streamlines. And while the intuition is very straightforward, the actual mathematics that power the technique are very complex.

Chapter 4

4 Analytical scheme

Clanet and Searby [14] suggested the acceleration mechanism (analytical - empirical theory) of flame acceleration in an open-ended tube. They stated that the flame acceleration happens due to the initial ignition geometry at the tube axis when a flame develops to a finger-shaped front, with surface area growing exponentially in time. Flame surface area develops fast but only for a short time. Their combined analytical - empirical formulas predict the flame front location and relevant time for three different stages during the flame initial growth in reference to the spark site. These steps include; flame spherical shape, flame-wall first contact, and tulip flame starting point. The analytical part of flame acceleration theory is developed by Bychkov et al. [12] which determines the acceleration time, the growth rate and the maximal increase of the flame surface area. Xiao et al. [25] modified these equations for the square cross-sectional duct. These formulas are adopted in this study to be applied in the rectangular duct. The outcome of this approach is compared with the experimental data and the numerical simulation (laminar model) in the results chapter.

4.1 Acceleration mechanism

This theory ignores the pressure variations and relates the flame propagation speed directly to the burnt gas production rate. The flame skirt is close to the wall during the finger flame propagation. The flame skirt radial velocity toward the tube wall is an order of laminar burning velocity (0.2-0.4 m/s) while the flame tip axial velocity is much higher (10-50 m/s). The tube wall prevents the freely unburned gas radial movement. Figure 4.1 presents the simplified geometrical model of the flame front.

It is assumed that the flame surface can be represented as a cylindrical finger of radius "r" with a hemispherical tip. The model neglects the effect of curvature on the local burning velocity.

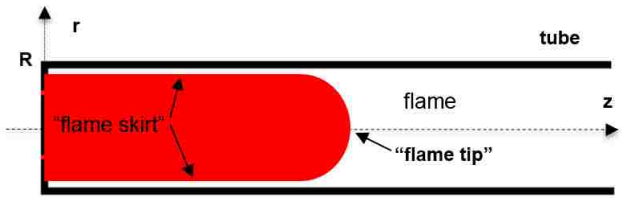

Figure 4.1: Geometry of a flame acceleration in an open end tube.

In the process of burning, the volume of the burnt gas (V_b) increases as:

$$\frac{dV_b}{dt} = \theta * S_l^0 * A_t \tag{4.1}$$

where the expansion ratio (θ) is defined as the density ratio of the fuel and the burnt gas. S_l^0 is the laminar burning velocity and A_t is the area of the total flame front. Supposing that the flame is cylindrical with a hemispherical cap:

$$V_b = \pi r^2 (z_{tip} - r) + \frac{2}{3}\pi r^3 \tag{4.2}$$

where z_{tip} is the tip axial ordinate. The major contribution to the flame surface area S comes from the flame skirt:

$$A_t \approx 2\pi * r * z_{tip} \tag{4.3}$$

Substituting Equations 4.2 and 4.3 into Equation 4.1, and neglecting $\frac{dr}{dt} \cong S_l^0$ compared with $\frac{dz_{tip}}{dt}$ and putting r = R, Equation 4.1 reduces to:

$$\frac{dz_{tip}}{dt} = \frac{z_{tip}}{\tau} \tag{4.4}$$

where:

$$\frac{1}{\tau} = \frac{2 * \theta * S_l^0}{R} \tag{4.5}$$

Equation 4.4 can be easily integrated to yield:

$$\frac{z_{tip}}{R} = e^{\frac{t - t_{sph}}{\tau}} \tag{4.6}$$

where t_{sph} is a time at which the initial spherical flame changes to a finger flame.

Clanet and Searby [14] plotted the characteristic time (t_{tulip}, t_{wall} and t_{sph}) versus the R/S_l^0 for the experiment and proposed Equations 4.7 , 4.8 and 4.9 :

$$t_{sph} = 0.1 \left(\frac{R}{S_l^0}\right) \pm 0.02 \left(\frac{R}{S_l^0}\right) \tag{4.7}$$

$$t_{wall} = 0.26 \left(\frac{R}{S_l^0}\right) \pm 0.02 \left(\frac{R}{S_l^0}\right) \tag{4.8}$$

$$t_{tulip} = 0.33 \left(\frac{R}{S_l^0}\right) \pm 0.02 \left(\frac{R}{S_l^0}\right) \tag{4.9}$$

where t_{wall} is the time at which the flame skirt touches the burner wall and t_{tulip} is the moment at which the dent appears at the flame front surface for the first time.

4.1.1 Adopted model for a duct

The model has been modified for the rectangular cross-section by substituting the "r" with "h/2" (h: duct height). Also, X_{tip} is the axial coordinate of the tip replaces with z_{tip} (see Figure 4.4). Therefore, the Equation (4.4) can be rewritten as:

$$\frac{dX_{tip}}{dt} = \frac{X_{tip}}{\tau} \tag{4.10}$$

where τ is the characteristic time:

$$\tau = \frac{h/2}{2 * \theta * S_l^0} \tag{4.11}$$

The flame leading tip position can be calculated through integration of both sides of the Equation 4.10 [14, 51]:

$$X_{tip} = (h/2) * \exp\left(\frac{t - t_{sph}}{\tau}\right) \tag{4.12}$$

The t_{sph}, t_{wall} and t_{tulip} can be estimated by the following linear relationships:

$$t_{sph} = 0.1\left(\frac{(h/2)}{S_l^0}\right) \pm 0.02\left(\frac{(h/2)}{S_l^0}\right) \tag{4.13}$$

$$t_{wall} = 0.26\left(\frac{(h/2)}{S_l^0}\right) \pm 0.02\left(\frac{(h/2)}{S_l^0}\right) \tag{4.14}$$

$$t_{tulip} = 0.33\left(\frac{(h/2)}{S_l^0}\right) \pm 0.02\left(\frac{(h/2)}{S_l^0}\right) \tag{4.15}$$

In this study, due to the position of ignitor, the value of calculated X_{sph} from Equation (4.12) should be divided by two.

4.2 Bychkov's model

Bychkov et al. [12] developed the analytical theory of acceleration mechanism. They considered the early stages of burning in a tube based on the Clanet and Searby [14] work. Consider a flame propagation in a cylindrical tube of radius "R" with one end closed (Figure 4.2). The dimensionless coordinates $(\eta; \xi) = (r; z)/R$, velocities $(w; v) = (u_r; u_z)/U_f$, and time $\tau = tU_f/R$ are used. An infinitesimally thin flame front which propagates with the velocity U_f (or unity in the dimensionless variables) is assumed. The flame is initially ignited at the tube axis at the closed end $(\eta; \xi)$ =$(0; 0)$. At the beginning the front is hemispherical, but the flame shape changes as the flame

skirt η_f moves along the tube end wall ($\xi = 0$) from the axis $\eta = 0$ to the side wall $\eta = 1$. The following calculations consider only the flow infinitesimally close to the wall at $\xi \to 0$. Therefore, the flame front touching the wall can be treated as locally cylindrical not only in the case of a finger shape even for the hemispherical front.

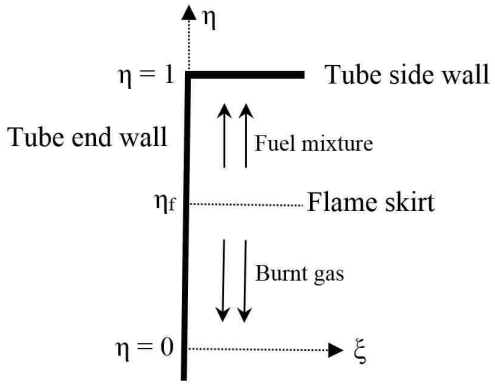

Figure 4.2: Flow close to the tube end wall.

The continuity equation for the in-compressible flow is:

$$\frac{1}{\eta}\frac{\partial}{\partial \eta}(\eta w) + \frac{\partial v}{\partial \xi} = 0 \tag{4.16}$$

where at the end wall ($\xi = 0$), $v = 0$. The flow along the wall in the limit of $\xi \to 0$ is interested. In the fuel mixture (labeled "1"), the flow is potential. So, it is assumed as:

$$v_1 = A_1 \xi \tag{4.17}$$

where the factor A_1 may depend on time. Employing Equation 4.16 and boundary condition at the side wall $w = 0$ at $\eta = 1$, the radial velocity of the fuel mixture is calculated as:

$$w_1 = \frac{A_1}{2}(\frac{1}{\eta} - \eta) \tag{4.18}$$

The velocity in the burnt gas (labeled "2") considering the boundary condition at the tube axis $w = 0$ at $\eta = 0$ is as:

$$v_2 = A_2 \xi \tag{4.19}$$

$$w_2 = -\frac{A_2}{2}\eta \tag{4.20}$$

In the Equations 4.19 and 4.20, it is assumed that the flame front is locally cylindrical and these two equations are potentially similar to the Equations 4.17 and 4.18. To complete the solution, the matching conditions at the flame front $\eta = \eta_f$ is considered:

$$\frac{d\eta_f}{d\tau} - w_1 = 1 \tag{4.21}$$

$$w_1 - w_2 = \theta - 1 \tag{4.22}$$

$$v_1 = v_2 \tag{4.23}$$

Equation 4.21 specifies the fixed propagation velocity U_f of the flame front with respect to the fuel mixture (which is unity in scaled variables). Equations 4.22 and 4.23 describe the jump of the normal velocity and continuity of the tangential velocity at the front. Equation 4.23 follows the irrotational assumption coupled with the cylindrical flame shape and it applies only at the flame skirt close to the tube wall. By substituting Equations 4.17-4.20 into Equations 4.21-4.23:

$$A_1 = A_2 = 2(\theta - 1)\eta_f \tag{4.24}$$

and for the flame front the equation is as:

$$\frac{d\eta_f}{d\tau} - (\theta - 1)(1 - \eta_f^2) = 1 \tag{4.25}$$

According to Equation 4.25, two opposite regimes of flame propagation can be separated: when the flame skirt is close to the axis $\eta_f \ll 1$, and when it is close to the wall $1 - \eta_f \ll 1$. In the limit of $\eta_f \ll 1$, the flame propagates with the velocity $\frac{d\eta_f}{d\tau} = \theta$ (or $\dot{R}_f = \theta U_f$). The same velocity takes place for an expanding hemispherical flame front. In the other case of $1 - \eta_f \ll 1$, the flame propagation velocity is $\frac{d\eta_f}{d\tau} = 1$ (or $\dot{R}_f = U_f$). In that limit a locally cylindrical flame skirt approaches the wall; the radial velocity of the fresh fuel mixture tends to zero, and the flame skirt propagates with the planar flame velocity with respect to the tube end wall. Integrating the Equation 4.25 with the initial condition $\eta_f = 0$ at $\tau = 0$:

$$\tau = \frac{1}{2\alpha} \ln(\frac{\theta + \alpha\eta_f}{\theta - \alpha\eta_f}) \tag{4.26}$$

or:

$$\eta_f = \frac{\theta}{\alpha} \tanh(\alpha\tau) \tag{4.27}$$

where:

$$\alpha = \sqrt{\theta * (\theta - 1)} \tag{4.28}$$

Considering Equation 4.27, the flame velocity is equal to the velocity of a hemispherical front close to the axis, when $2\alpha\tau \ll 1$ and $\eta_f = \theta\tau$ (or $R_f = \theta * t * S_l^0$). Respectively, one should expect transition to the finger shape flame at the characteristic time:

$$\tau_{sph} \approx \frac{1}{2\alpha} \tag{4.29}$$

when the flame skirt is at $\eta_f \approx 0.5\frac{\theta}{\alpha}$. It should be mention that there is no exact mathematical definition of the transition time and the characteristic time comes as a parameter considering the shape of function "tanh" at Equation 4.27.

Substituting $\eta_f = 1$ into the Equation 4.26 :

$$\tau_{wall} = \frac{1}{2\alpha} \ln(\frac{\theta + \alpha}{\theta - \alpha}) \tag{4.30}$$

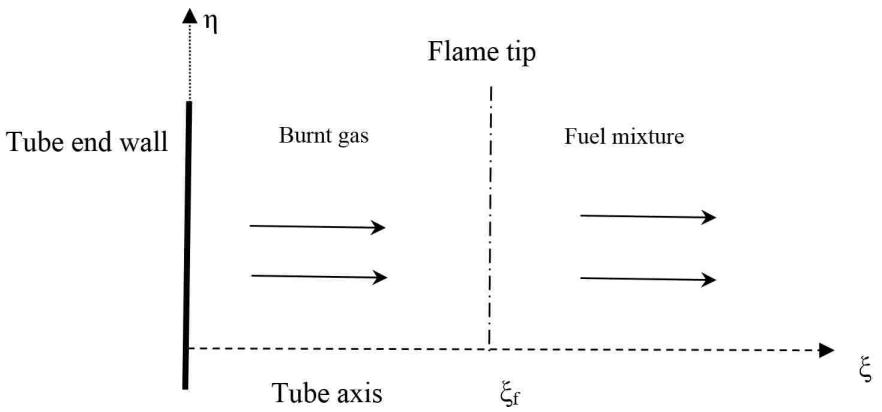

Figure 4.3: Flow close to the tube axis.

Considering the flow along the axis $\eta = 0$ as shown in Figure 4.3, then it is also possible to find evolution of the flame tip. The equation for ξ_{tip} becomes:

$$\frac{d\xi_{tip}}{d\tau} - v_2 = \theta \tag{4.31}$$

Equation 4.31 is the condition of a fixed propagation velocity of a planar flame front written with respect to the burnt matter. The flame shape assumes locally planar close to the axis, at $\eta \to 0$. In that limit the flow may be described as a potential one, with the axial velocity component (v) determined by a function similar to the Equation 4.19. The solution for v along the axis has to coincide with

Equation 4.19 at $\eta \to 0$,$\xi \to 0$. Thus the same formula for v_2 along the axis as in Equations 4.19 and 4.24 has been obtained. Therefore, the differential equation for the flame tip is as:

$$\frac{d\xi_{tip}}{d\tau} - 2(\theta - 1)\eta_f(\tau)\xi_{tip} = \theta \tag{4.32}$$

with the initial condition $\xi_{tip}(0) = 0$ and with the solution:

$$\xi_{tip} = \frac{\theta}{4\alpha}[\exp(2\alpha\tau) - \exp(-2\alpha\tau)] = \frac{\theta}{2\alpha}\sinh(2\alpha\tau) \tag{4.33}$$

Just after ignition, $2\alpha\tau \ll 1$, the flame tip moves in the same way as the flame skirt, $\xi_{tip} = \eta_f = \theta\tau$.When the flame skirt touches the wall, $\tau = \tau_{wall}$, the position of the flame tip is:

$$\xi_{wall} = \xi_{tip}(\tau_{wall}) = \frac{\theta}{2\alpha}\sinh(2\alpha\tau_{wall}) = \theta \tag{4.34}$$

or $z_{wall} = \theta R$ in the dimensional units.

Bychkov et. al [12] plots the skirt velocity $\frac{U_{skirt}}{U_f}$ versus the value $2\alpha\frac{z_{wall}}{R}$ for the experiment and as a result:

$$U_{skirt} = \beta 2\theta\sqrt{\theta(\theta - 1)}U_f \tag{4.35}$$

where the factor β comparable to unity. As the skirt position moves along the wall, the burnt gas velocity, Equation 4.19 modifies roughly as:

$$v_2 = A_2(\xi - \xi_{skirt}) \simeq 2(\theta - 1)(\xi - \xi_{skirt}) \simeq 2\alpha(\xi - \xi_{skirt}) \tag{4.36}$$

and considering Equation 4.35, Equation 4.32 reduces to:

$$\frac{d\xi_{tip}}{d\tau} \simeq 2\alpha\xi_{tip} - (2\alpha)^2\beta\theta(\tau - \tau_{wall}) + \theta \tag{4.37}$$

For the initial condition $\xi_{tip}(\tau_{wall}) = \theta$, the last term in the Equation 4.37 can be neglected in the limit of $\theta^{-1} \ll 1$. Integrating Equation 4.37 :

$$\xi_{tip} = -(\beta - 1)\theta \exp[2\alpha(\tau - \tau_{wall})] + \beta\theta[2\alpha(\tau - \tau_{wall})] \tag{4.38}$$

The instant tulip corresponds to $z_{tip} = z_{skirt}$ or $d\xi_{tip}/d\tau = 0$, and the interval of inversion $t_{lag} = t_{tulip} - t_{wall}$ is calculated from Equation 4.38 as:

$$U_f * t_{lag}/R = \tau_{lag} = (2\alpha)^{-1} \ln(\frac{\beta}{\beta - 1}) \tag{4.39}$$

It should remember that calculations 4.36-4.39 are only a qualitative model based on the empirical formula 4.35. Therefore, in reality, one should interpret Equation 4.39 as another correlation of the form:

$$t_{lag} = \lambda(2\alpha)^{-1}\frac{R}{U_f} \tag{4.40}$$

with the coefficient λ comparable to unity.

4.2.1 Modified model for a duct

In this section, the mentioned equations are modified to be applied in the duct.

4.2.1.1 Spherical flame shape

This step is defined as the required time for the flame to transform into a finger shape (t_{sph}). In other words, this is the last moment since the spark time at which the flame still has its spherical shape (see Figure 4.4):

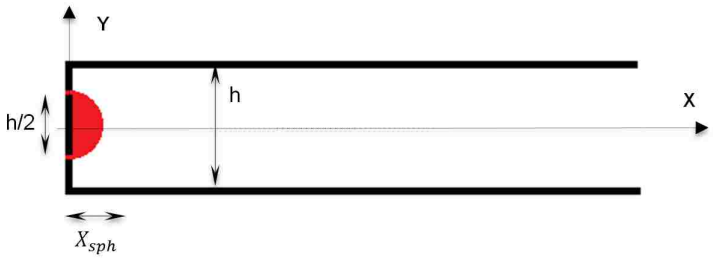

Figure 4.4: Schematic of the spherical flame stage.

$$t_{sph} = \frac{1}{2\alpha} * \left(\frac{(h/2)}{S_l^0} \right) \tag{4.41}$$

For the propane/air mixture at equivalence ratio of 1.1, the expansion ratio is equal to $\theta = 8$. The laminar burning velocity is $S_l^0 = 0.32$ m/s. "h" is equal to the duct height. The location of flame front for the spherical step is defined as:

$$X_{sph} = \frac{h}{4} \tag{4.42}$$

4.2.1.2 Flame-wall first touch

Figure 4.5 illustrates the schematic of the flame skirt when it comes to contact with the side wall for the first time.

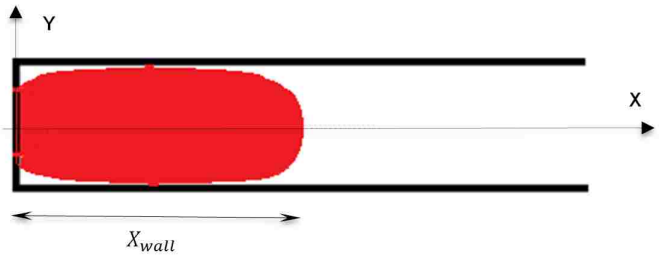

Figure 4.5: Schematic of the flame-wall first touch.

The time and the location of the flame front when the flame skirt touches the wall for the first time are given by Equation 4.43:

$$t_{wall} = \frac{1}{2\alpha} * \frac{(h/2)}{S_l^0} * \ln\left(\frac{\theta+\alpha}{\theta-\alpha}\right) \tag{4.43}$$

$$X_{wall} = \theta * (h/2) \tag{4.44}$$

when Lewis number is assumed to be unity.

4.2.1.3 Tulip flame starting point

This is defined as the moment at which the dent appears at the flame front surface for the first time (Figure 4.6). In other words, it is the last moment before the creation of dent through the flame front (tulip flame initiation).

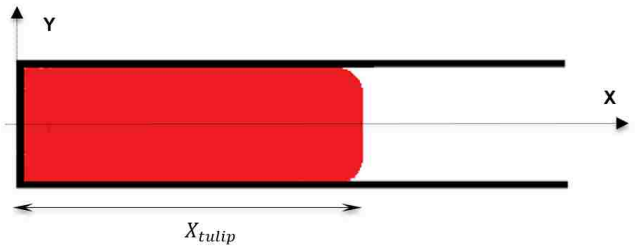

Figure 4.6: Schematic of the tulip flame starting point.

The time and location of the flame front at the start of tulip flame formation are described as follows:

$$t_{tulip} = t_{wall} + t_{lag} \tag{4.45}$$

$$X_{tulip} = U_{skirt} * t_{tulip} = \left(2 * \beta * \theta * \alpha * S_l^0\right) * t_{tulip} \tag{4.46}$$

where β is the model constant (=1.25 according to [12]) and the lag time [50, 12] is:

$$t_{lag} = \lambda * \left(\frac{1}{2\alpha}\right) * \left(\frac{(h/2)}{S_l^0}\right) \tag{4.47}$$

where λ is the model coefficient (λ=1 for this study).

Chapter 5

5 Results for fully opened end: Experiment

In this chapter, the results obtained from the experimental method for the opened end case are explained.

5.1 Experimental results

In Figure 5.1, experimental results for the three trial at $\Phi = 1.1$ (rich condition) are presented. The experiment is repeated 50 times for the constant initial condition. Comparison of the obtained results shows that the trend for most of the trials (about 90%) is similar to those which are plotted in Figure 5.1. The curves show the flame front distance (with respect to the spark location) versus the flame propagation time. The flame front is taken at the duct centre-line. In this graph, the regions of tulip flame and flame first inversion are addressed based on the captured image in the experiment. As the figure shows, there is acceptable repeatability on all trials specifically for initial flame from ignition to the tulip flame. The maximum discrepancy at this area between these trials is about 76 mm and 2.4 ms. The discrepancy between the trials increases as the flame enters the first inversion zone (146 mm and 2.3 ms). The differences between trials reach keep increasing at the first inversion zone (77 mm and 5.6 ms). The maximum discrepancy can be seen in the first inversion region (up to 422 mm and 6.2 ms). This behavior can be primarily attributed to chaotic effects caused by turbulence at the first inversion region and after that towards the duct end. This is one of the main motivations for the numerical simulation of this phenomenon.

5.2 Trend in experimental flame propagation speed

Other than the point which is mentioned in section 5.1.1, a variation of the absolute speed of the flame along the duct can also be noticed. Figure 5.2 depicts these variation for the slightly rich mixture ($\Phi = 1.1$). The flame is not moving at a constant speed, periodically speeding up and slowing down. This pattern repeats itself several times along the duct. For the purposes of this work this behavior is defined as "leap frog". The films show that after ignition, the flame assumes a spherical shape.

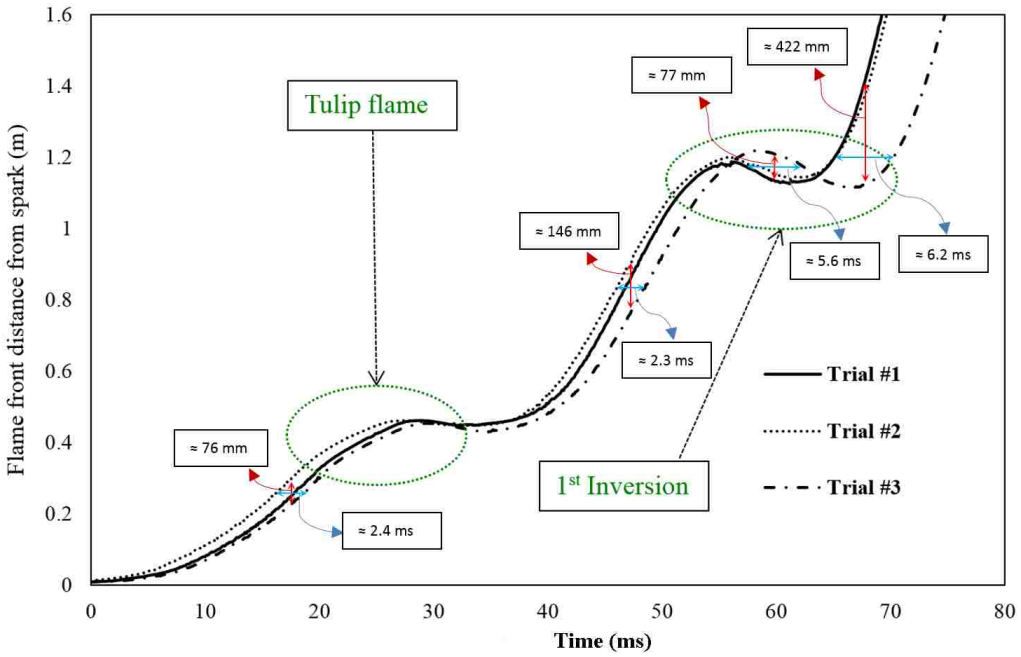

Figure 5.1: Experimental results for the uniform composition field ($\Phi = 1.1$), changes of the flame front position along opened end FPD centre-line for three different trials.

As the flame propagates it touches the wall and evolves into a finger shape (parabolic) before deforming into a flat profile. This happens after the flame lateral parts (flame skirt) touch the wall which causes a decrease of the reaction surface area and therefore a decrease in the flame propagation speed. The flame continues decelerating until the absolute flame speed reaches zero. At this point, the flame develops a horizontal split referred to as the tulip flame (for close ended case).

After a short distance, the tulip flame collapses on itself and forms the finger shape

again. Upon collapsing the tulip flame, the flame accelerates again until absolute flame speed reaches above 50 m/s. The process of accelerating and decelerating repeats again one or two more times. For the purpose of this work this behavior is defined as "1st inversion" and "2nd inversion". Finally, the flame accelerates and leaves the duct with high speed (V$\simeq$ 100 m/s).

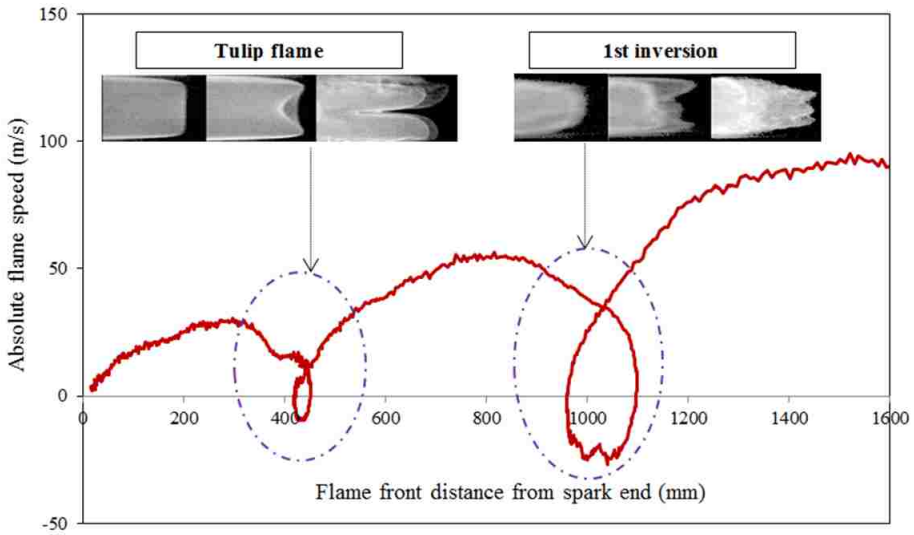

Figure 5.2: Changes of absolute flame speed along the channel centre-line versus flame front distance from spark. The tulip flame front and 1st inversion are depicted (opened exit and mixture equivalence ratio $\Phi = 1.1$). Note the characteristic "leap frog" flame movement.

The same periodic acceleration and deceleration pattern is expected for the unburnt flow ahead of the flame. This is referred to as a "flame feeding flow". A quick comparison of the flame surface from tulip to 1st inversion suggests that the flame at tulip stage is mostly laminar, while it becomes more wrinkled and turbulent at the 1st inversion zone. This will be explored more later.

Another feature worth noticing is the much higher absolute flame speed when compared to propane/air laminar flame speed ($\approx$ 0.32 m/s) at most points along the duct. This is due to three different reasons. Firstly, the ratio of unburnt gas density to the burnt gas (for $\Phi = 1.1, \frac{\rho_f}{\rho_b} \approx 8$). This is referred as a dilatation of

burnt gas [35]. Secondly, the total flame surface increased because of wrinkling which primarily is the product of turbulent in feeding flow ahead of the flame front (see Figure 6.4). The sequence of increasing absolute flame speed maximum from the tulip stage ($\approx$ 25 m/s) to the 1st inversion ($\approx$ 50 m/s) and finally after the 1st inversion ($\approx$ 100 m/s) is worth investigation. Increasing of amounts burnt combustion products as the flame propagates along the duct is the key factor here. Furthermore, whilst the flame propagates to the exit end the turbulent in feeding flow ahead of flame increases and this can be addressed as a reason for increased flame speed (see Figure 6.4).

5.3 Pressure at the ignition end versus the flame propagation speed

Figure 5.3 depicts the variation of pressure at the ignition end, filtered with a low pass filter of 25Hz, 50Hz and the absolute flame speed from the experiment. The pressure trace correlates well with the changes in the characteristic tedious flame. When the low pass filter of 50Hz was applied, a clear correspondence between the pressure, the tulip flame, and the 1st inversions occurrence times can be seen. The pressure is increasing in each sequence, only to drop rapidly at the time of the tulip flame formation and the 1st flame inversion point. Besides the pressure rise due to the ignition when using a 50Hz filter, both pressure traces exhibit the same trends as mentioned above.

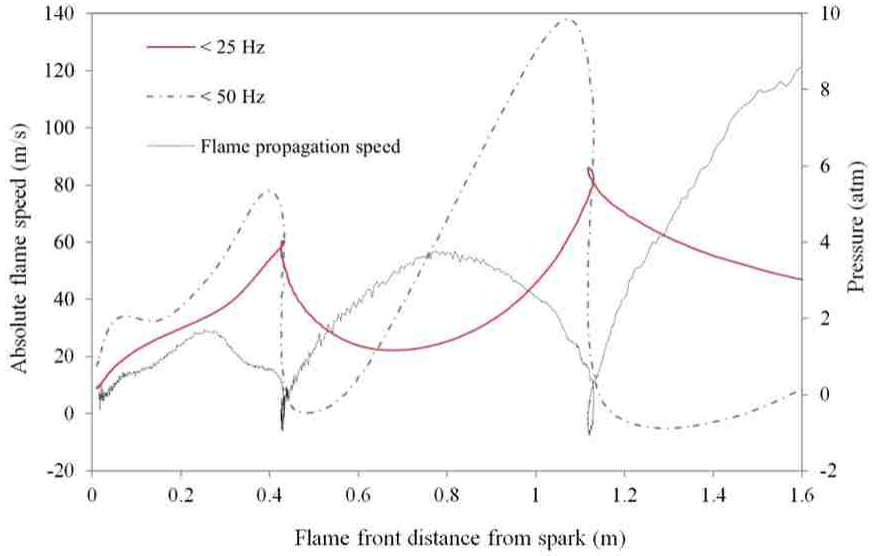

Figure 5.3: Experimental results for pressure at ignition end and absolute flame speed versus flame location (propane/air mixture, Φ =1.1, and opened end). The pressure data filtered with two low pass filters of 25Hz and 50Hz.

After ignition once the flame starts to propagate, a compression wave moves across the duct. From the open end of the duct, this wave reflects back as an expansion wave, which one could consider as one of the effective means behind the tulip flame formation. Also, this phenomenon may contribute to the backward flame movement (see experimetal data in Figures 6.2 and 6.3at 0.4 m & 1 m locations). This reversed movement of the flame has not been reported by other researchers. As the Figure 5.3 illustrates, the duct pressure oscillates along the flame propagation. This can cause the surrounding air enters the duct and push the flame backward.

The laminar combustion model could not capture flame reverse movement. This is due to the outlet boundary condition which stops reverse flow from surrounding to the duct.

Chapter 6

6 Results for fully opened end: Laminar combustion model

In this chapter, the results obtained from the laminar combustion model for the opened end case are presented. These results are compared with the experimental data. The reasons behind the tulip flame formation and the flame first inversion are discussed. Also, the results from all three methods including the laminar combustion model, experiment, and analytical approach are compared.

6.1 Laminar flame model versus experiment

Qualitative comparison of tulip flame formation and its lips collapsing in both numerical (laminar flame model) and experimental methods are depicted in Figure 6.1. The experimental results (frames a-e) are the flame front position as captured by high speed camera during experiments for the uniform propane/air composition field (Φ =1.1). In the numerical results (frames a´-e´), colours designate the temperature of the cold gas (blue) to the combustion products (red) from the simulation. All stages of flame development (spherical shape, flatting, dent creation (its growing and tulip formation) and lips collapsing) are almost identical in both experimental and numerical results. As expected the wrinkling factor ignores in laminar combustion model. Therefore, the numerical flame is smoother and much less wrinkled.

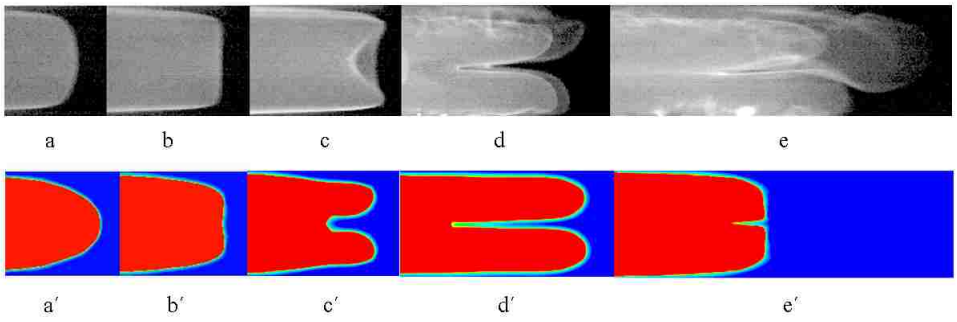

Figure 6.1: Qualitative comparison of tulip formation stages between numerical result (laminar flame model) and experimental one ($\Phi = 1.1$ and opened end). At bottom pictures (a´-e´), the colors designate the temperature from the cold gas (blue) to the combustion product (red).

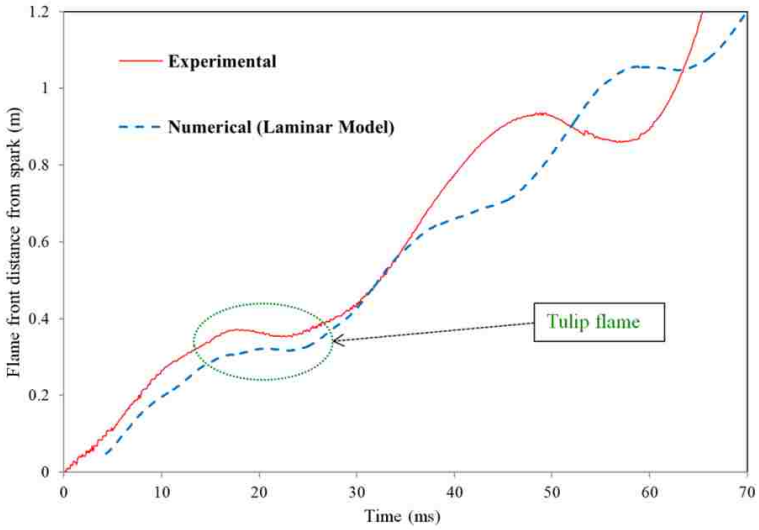

Figure 6.2: Laminar flame model versus experimental result for the uniform composition field ($\Phi = 1.1$), changes of the flame front position along opened end FPD centre-line versus propagation time.

Figure 6.2, compares the numerical result with the experimental ones quantitatively. The flame location and speed in the first 30 ms (before the tulip) for both are in a good agreement (correlation coefficient = 0.976). The model reasonably well captures the development of the tulip flame. The numeric is underestimated the experiment considerably after the tulip flame zone and up to t = 50 ms. These differences may be an effect of the turbulence induced in the unburned mixture

by the expanding flame.

Figure 6.3 plots the absolute flame speed versus the flame front distance from spark for the both numerical (laminar model) and experimental data (from Figure 6.2). The numerical model predicts the acceleration and deceleration of absolute flame speed although it simulates one more inversion (x > 1 m). As the figure shows, the numerical flame is generally slower. Both experimental and numerical model flames have almost similar flame speed up to the point x≈0.2 m. But the numerical flame speed starts dropping in a shorter distance from the spark point (x≈0.2 m) in comparison to the experimental flame (x≈0.3m). The deceleration of numerical flame absolute speed at first inversion zone onsets at x≈0.6 m, while the experimental flame deceleration occurs at x≈0.9 m.

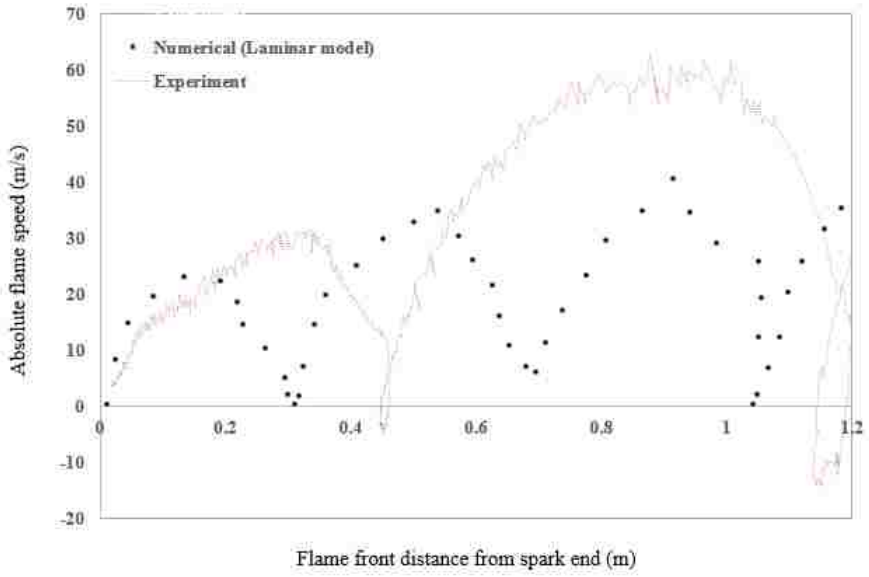

Figure 6.3: Changes of absolute flame speed along the channel centre-line versus flame front distance from spark for laminar flame model and experimental result (opened exit and mixture equivalence ratio $\Phi = 1.1$).

Figure 6.4, plots the normalized flow velocity ahead of flame and flame location versus normalized flame propagation time from the numerical simulation. The flow velocity is normalized by propane laminar flame speed (≈ 0.32 m/s), the flame front location is normalized by duct length, and propagation time is normalized by total

propagation time. Sample points are taken at varied distances ahead of the flame front. The critical velocity for the flow at the transition regime to turbulent condition (Re $\approx$ 4000) is calculated as 1.25 m/s (U/S_l $\approx$ 4). Considering this value and the results shown in Figure 6.4, one can notice that the flame feeding flow is laminar at two locations; at the ignition point and at the tulip formation point. Before the tulip flame forms, the flow is turbulent and then it becomes transitional for a short time period, before turning again into the laminar flow. While dent starts growing on the flame front surface, the speed of the flow ahead of flame increases as the flow transits back to the turbulent state. Unlike at the tulip point, the speed of unburned mixture flow ahead of the 1st inversion decreases, however the flow still remains turbulent. The laminar model under-predicts the experimental result regarding the flame speed after the tulip flame location. The laminar model does not consider the effects of turbulence on the burning velocity calculation and hence, the under-prediction. The turbulent model may provide a better results for the subsequent inversions. Another point worth mentioning is that the EBU model ignitor and generally Star CCM+ ignitors models are not capable of simulating the kernel flame grow process.The used model works based on instantaneous increasing of the temperature for limited pre-defined cells and does not simulate the kernel flame growth. Therefore, the flame initial stage (t $<$ 2 ms) does not show in Figure 6.2. Also, during this period of time (0-2 ms) the numerical flame is sensitive to the initial conditions. Therefore, several simulations with slight differences in initial conditions (k and epsilon) have been done to capture the right profile of kernel flame.

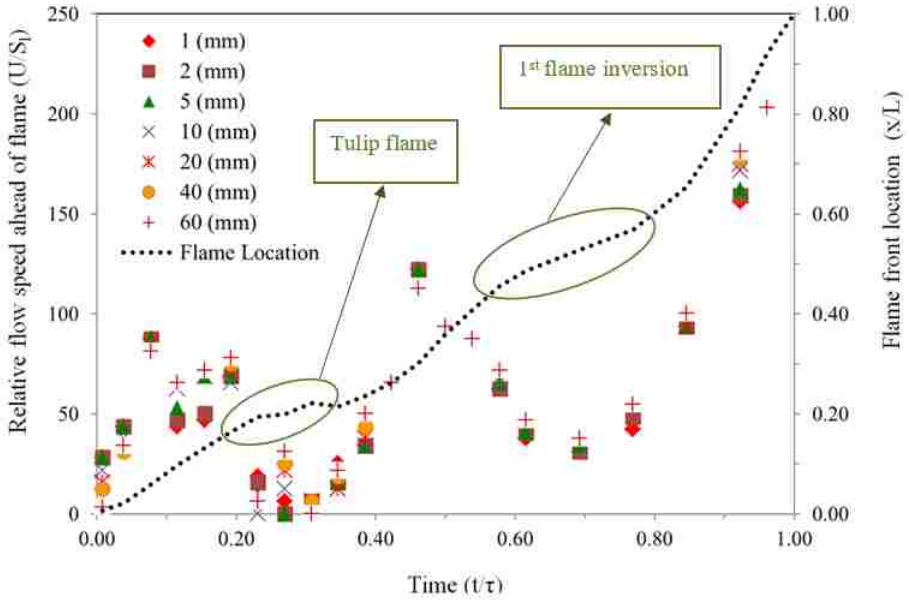

Figure 6.4: Normalized flow speed and normalized flame front location versus normalized flame propagation time from numerical results (laminar combustion model - opened end exit). Legends show the point distance ahead of flame.

6.2 Tulip flame

Figure 6.5 illustrates the flame surface (fuel mass fraction margin between 0 and 0.06) evolution during the tulip flame formation based on numerical simulation (using a laminar combustion model). Considering the equivalence ratio to be equal to 1.1, the mass fraction of propane should be 0.06 in the fresh mixture.

At t = 15 ms, the flame front surface becomes flat and the total flame surface area decreases.

At t = 15.5 ms, the flame front splitting process onsets. The central flame dent is now much deeper and much more pronounced at t = 16 ms.

As the flame upper and lower lips keep moving forward, the central dent remains stationary (t = 16.5-17 ms) until the merging of lips at t = 18 ms.

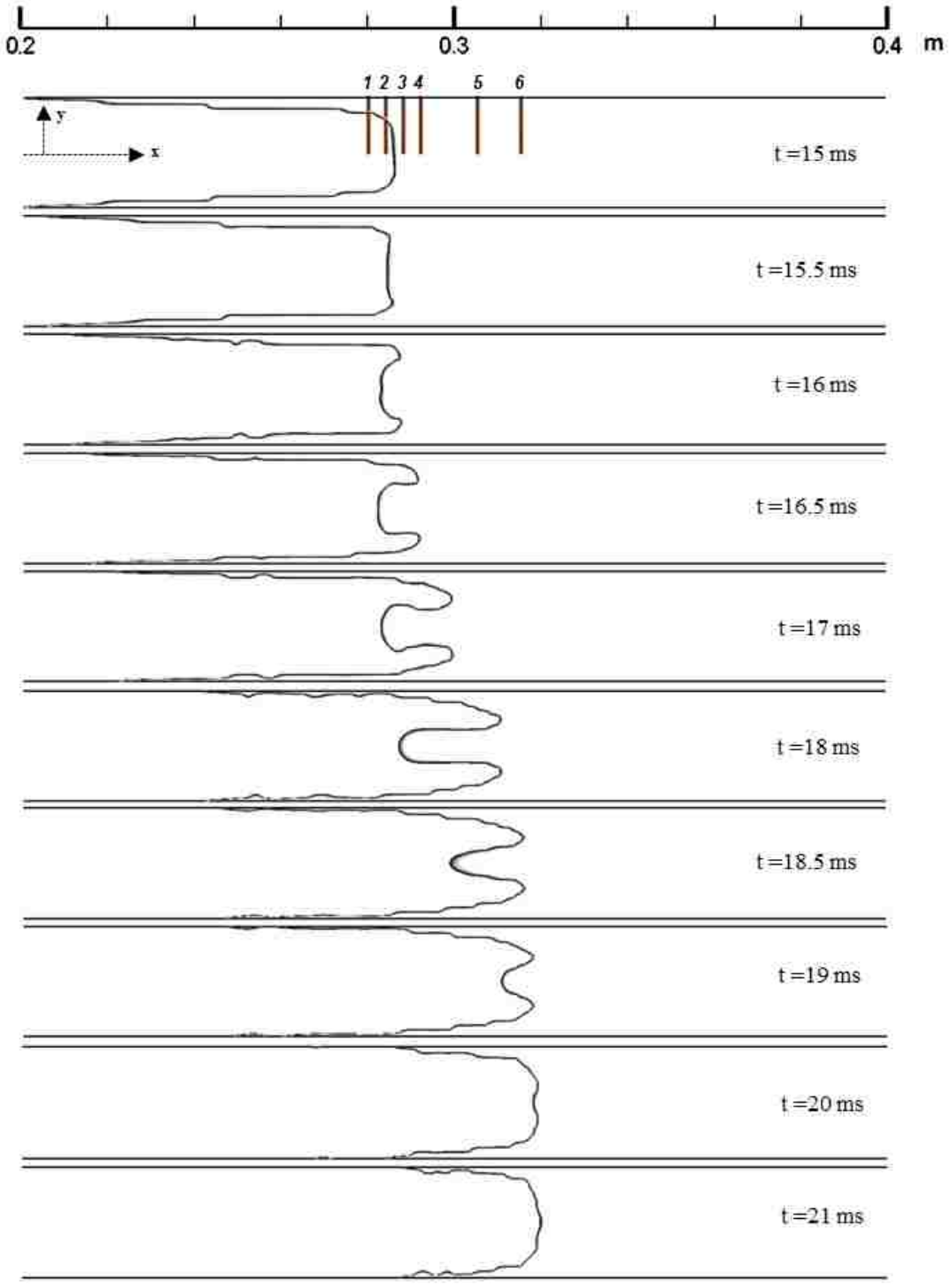

Figure 6.5: Flame surface (marked by the fuel mass fraction margin between 0 and 0.06) evolution during the tulip flame formation. Cross-section locations at x_1= 28 cm (x/L=0.1750), x_2= 28.4 cm (x/L=0.1775), x_3= 28.8 cm (x/L=0.1800), x_4= 29.2 cm (x/L=0.1825), x_5= 30.5 cm (x/L=0.1906) and x_6= 31.5 cm (x/L=0.1969).

As the smaller lips move forward, they collapse inward and this continues until the final gap closure at t = 21 ms. The visual inspection shows the total flame surface area decreases during this process.

At t = 19 ms, the flame lips are still present, however they are not as pronounced as in previous time steps.

At t = 20 ms, the flame lips are nearly fully collapsed and finally at t = 21 ms, the flame assumes a finger shape again.

Cross-sections x_1-x_6 are shown in this figure. In the following sections, distributions of several variables (velocity, pressure, mass fraction) will be shown along these cross-sections to describes the flame structure.

6.2.1 Velocity distribution at tulip flame formation zone

Figure 6.6 demonstrates the normalized velocity distribution around the tulip flame for x_1-x_6 cross-sections. The flame front will gradually cross these locations when the tulip flame forms.

At t = 15 ms, the flame front surface is mostly between the cross-sections x_2 and x_3 that are cross-sections where the flame assumes a flat profile. The velocity profiles for the cross-sections x_1 and x_2 that are behind the flame front are similar. Both of them have zero velocities close to the wall and then it goes to a region of much higher velocities, up to $y/H > 0.3$ and $y/H > 0.4$ respectively. These regions are still in the unburnt mixture area ahead of flame. Once these cross-sections enter the burnt mixture, the velocities are much lower all the way to the centre-line. In contrast, along the two cross-sections well ahead of the flame, at $x_5$and x_6, the velocity profile are almost mirror image of these at x_1 and x_2, lower for $y/H > 0.35$ and higher for $0 \leqslant y/H < 0.35$. The profile obtains a concave shape as the duct centre-line is approached. Cross-section x_3 has a smoother velocity variation than the others. Cross-section x_4 has a similar pattern as cross-section x_3. At this location lower

peak value and higher value at the centre-line are present. Looking more precisely, the 'V' pattern close to the wall is visible. The similar pattern can be seen in the other two cross-sections x_5 and x_6 ahead of the flame front. The velocity at the cross-section x_4 decreases gradually while the velocities at the cross-sections x_5 and x_6 are nearly constant when they cross the duct centre. The higher velocity values close to the wall for the cross-sections x_1, x_2, x_3 and x_4 explain the higher push by the flame at the lateral part in comparison to the flame centre.This can also refer to a total flame surface at the flame skirt. The order of velocity peak point from x_1 to x_6 is related to their distance from the flame surface.One important point refers to the 'V' pattern especially at the cross-sections x_5 and x_6. This can be due to the vortices formation in front of flame and attached to the wall [it will be shown later in Figure 6.9]. That would create negative velocity at those points and form the 'V' shape for the cross-sections x_5 and x_6.

At t = 15.5 ms the flame front starts moving backward, the velocity peak values close to the wall for the cross-sections x_1 and x_2 reduce a bit. After a 'Λ' shape close to the wall, the velocity profile becomes convex and increases as the duct centre is approached. The shape of cross-section x_3 remains almost unchanged. Despite the decrease in peak value close to the wall for cross-section x_4 it almost has the same pattern as at t = 15 ms. The main change is for the cross-sections x_5 and x_6. Velocity increases close to the wall, a wider 'Λ' shape and reduction to zero velocity close to the duct centre. This reduction from 10 m/s to 0 m/s (compared to t = 15 ms) is due to the flame front at the centre stalling.

At t = 16 ms the dent initiates and the flame locates between the cross-sections x_1 and x_3. The profile of cross-sections x_1, x_2 and x_3 do not change considerably. The cross-section x_3 shape looks similar to the flame surface at this moment. The main alteration can be seen in the cross-section x_4. The 'Λ' shape close to the wall becomes smaller and the next 'Λ' shape peak value increases. The cross-sections

x_5 and x_6 'Λ' shape peak value decreases with a slight increase in the velocity value after the peak compares to t = 15.5 ms.

At t = 17 ms, the tulip forms and the split grows through the flame centre. Now, the 'Λ' shape close to the wall for the cross-sections x_1 and x_2 becomes wider with same peak value with a minor decrease as the duct centre is approached. The velocity value decreases to zero at duct centre. The cross-section x_3 has a similar shape as the cross-sections x_1 and x_2, however with higher velocity peak value. Also, the 'Λ' shape is shifted away from the wall and approaches to the middle of the cross-section. The cross-section x_4 velocity profile has a similar pattern as the cross-section x_3, but with higher peak value. Now, the 'V' shape in previous time step is entirely disappeared. The cross-sections x_5 and x_6 loosed their 'Λ' form close to the wall. Their velocity profiles start from about $U/S_l \approx 15$ and increase steadily until they reach $U/S_l \approx 50$ and then, they keep this constant value as they reach the duct centre.

At t = 18 ms and the tulip flame has reached its maximum depth, and the flame lips merging begins. For the cross-sections x_1, x_2, and x_3 the 'Λ' shape close to the wall remains, but the rapid reduction in the values should be mentioned. Also, rather than a gentle reduction to zero, the velocity rises sharply and becomes constant until duct centre. The peak value for the cross-section x_3 is again higher than cross-sections x_1 and x_2. For the cross-section x_4, the 'Λ' pattern forms with two convex shapes with much smaller peak values. This is also analogous to the wave shape with gradual reduction rate from the wall to the duct centre. For the cross-sections x_5 and x_6, there is no change in the profile trend, however peak velocity values reduce.

At t = 19 ms, the collapsing process continues with the flame front passing through cross-section x_6. At this moment, cross-sections x_1, x_2 and x_3 velocity profiles are almost the same with the tendency to dilute the 'Λ' shape close to the wall. This diminished trend is more obvious for the cross-section x_4. For the cross-sections x_5 and x_6 vortices still exist in this area and the velocity reduces as the result of

eddies decay. More disturbance is present along the cross-sections. This can be seen much clearer for the cross-section x_6 profile.

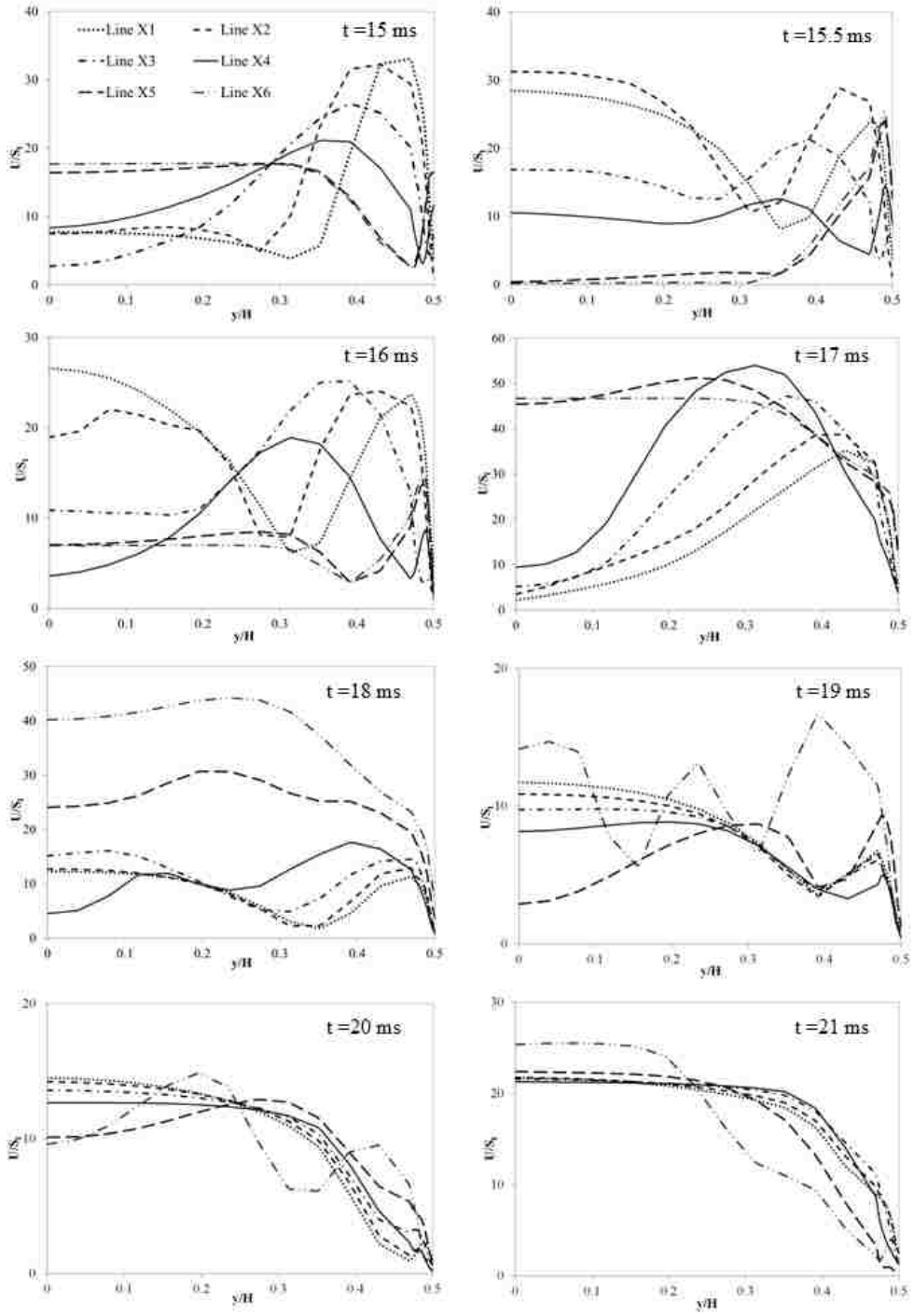

Figure 6.6: Normalized velocity distribution during the tulip flame along x_1-x_6 cross-sections from the numerical simulation (laminar combustion model). Note different range of the vertical axis at different times.

At t = 20 ms the collapsing is almost completed. The cross-sections x_1-x_5 all have a similar pattern. For these cross-sections, the velocity profile is increasing gradually to the mid of the cross-section and then remains constant until duct centre. The tendency of damping the disturbance and the movement to a similar velocity profile as the others can be seen for the cross-section x_6.

At t = 21 ms the finger shape flame forms again and all the cross-sections are located on the backside of the flame front. At this moment, all cross-sections have a similar shape as described for the cross-sections x_1-x_5 at t = 20 ms. This pattern is somehow similar to the flame front velocity profile at t = 15 ms except its magnitude.

Figures 6.7 and 6.8 plot the normalized velocity distribution and fuel mass fraction along the duct length at different times during the tulip flame formation for y/H = 0 (centre-line), y/H = 0.45 and y/H = 0.49 heights (both practically at the wall). The fuel mass fraction profile clearly identifies the unburned mixture region and the combustion products region and the flame front in between. The cross-section y/H = 0.49 shows the flame near the wall by excluding the wall boundary/initial conditions effects, however, the cross-section y/H = 0.45 illustrates the flame speed outside the mesh prism layers.

At t = 15 ms and distances less than x/L = 0.2, the velocity profiles for all three locations are similar. The differences occur at the flame front. At the centre-line (y/H = 0), from the front end of the duct, the velocity is increasing (up to x/L = 0.1) and then it remains constant at $U/S_l \approx 10$. Just before the flame front location, at x/L $\approx$ 0.2, there is a small reduction in velocity to $U/S_l \approx 5$, followed by the sharp velocity increase up to $U/S_l \approx 20$. For large distances, past the flame, the velocity rises gradually again (up to $U/S_l \approx 60$ at x/L $\approx$ 0.6). The velocity profiles for y/H = 0.45 and y/H = 0.49 are similar. For y/H = 0.49, the velocity increases sharply up to $U/S_l \approx 26$ (at x/L $\approx$ 0.12). Then the velocity goes through pulsation which causes a rapid rise, fall, and rise again (changing between

$U/S_l \approx 0 - 26$). The velocity keeps its constant value below $U/S_l \approx 5$ up to $x/L \approx 0.4$. The velocity increases again subsequently.

At t = 15.5 ms, the velocity along centre-line (y/H = 0) increases gradually before the flame front and then it immediately drops down to zero at the flame location. The velocity profile for the cross-section y/H = 0.45 splits into two regions. The first region is the section before the flame front. In this region, the velocity value is almost twice its similar profile in comparison to previous time step. At the flame location, the velocity increases and suddenly decreases to velocity values are less than at t = 15 ms (second region). It should be noted that the velocity rises after $x/L \approx 0.7$. The velocity profile along cross-section y/H = 0.49 follows similar trend and value as t = 15 ms in the first region before the flame front. The velocity elevates up to $U/S_l \approx 30$ and a 'Λ' shape can be seen for the rest of the profile.

At t = 16 ms while the tulip onsets, the cross-section y/H = 0 velocity profile does not change significantly in the first region before the flame front. The velocity value decreases in the second region after the flame. The same trend can be seen for the velocity profile along cross-section y/H = 0.45. For the velocity profile along cross-section y/H = 0.49, the velocity value in the first region decreases slightly when compared to previous cases.

At t = 17 ms as the flame split grows at flame centre, the cross-section y/H = 0 velocity profile gets its higher discrepancy at the flame location. It has Max value about $U/S_l \approx 50$ and Min value about $U/S_l \approx 0$. Small velocity drop just before the flame front, rapidly increase for a short distance and then gentle reduction to $U/S_l \approx 0$ at $x/L \approx 0.42$ can be seen. The cross-section y/H = 0.45 velocity profile changes a lot in comparison to t = 16 ms. It's profile now has a similar trend as y/H = 0 despite the fact that the cross-section y/H = 0 has small lips when it comes to velocity reduction after the flame location. The cross-section y/H = 0.49 velocity profile does not have clear trend beside that its pulsation increase before the flame location. It is similar

to the other two cross-sections at the flame location and afterward. One interesting point here is the point at which velocity decreases for each of the cross-sections after the flame front. It follows the general rule where the cross-section with higher velocity peak value drops down further away from the flame front location.

At t = 18 ms the flame lips merging starts. The same trend can be seen for the velocity profile along cross-section y/H = 0 as t = 17 ms until x/L $\approx$ 0.4. But at the duct end, the velocity rises in contrast to t = 17 ms. For the velocity profile along cross-section y/H = 0.49, almost the same trend remains as previous time step excluding two points. At this time the curve becomes smooth at the flame location and the lips shape has dissipated. Moreover, for the duct end similar to the cross-section y/H = 0 the velocity increases. For the cross-section y/H = 0.49, the velocity profile follows the same description as the cross-section y/H = 0.45 except that it still can be seen the pulsation before the flame front.

At t = 19 ms the flame lips merging process closes to its final stage. For all cross-sections, the velocity profile slows down with the similar trend as t = 18ms.

At t = 20 ms, the collapsing step is almost completed. The general trend for all the cross-sections since the last time step is the velocity elevating traveling from the left to right side of the duct. The all three velocity profiles do not change significantly in comparison with t = 19 ms. However, the velocity value in all three cross-sections are generally increasing.

At t = 21 ms, the flame finger shape forms again. For all cross-sections, the velocity profiles before x/L $\approx$ 0.7 increases in comparison to t = 20 ms. They keep the same trend as they were in t = 20 ms. After the x/L $\approx$ 0.7, the velocity falls for all three cross-sections.

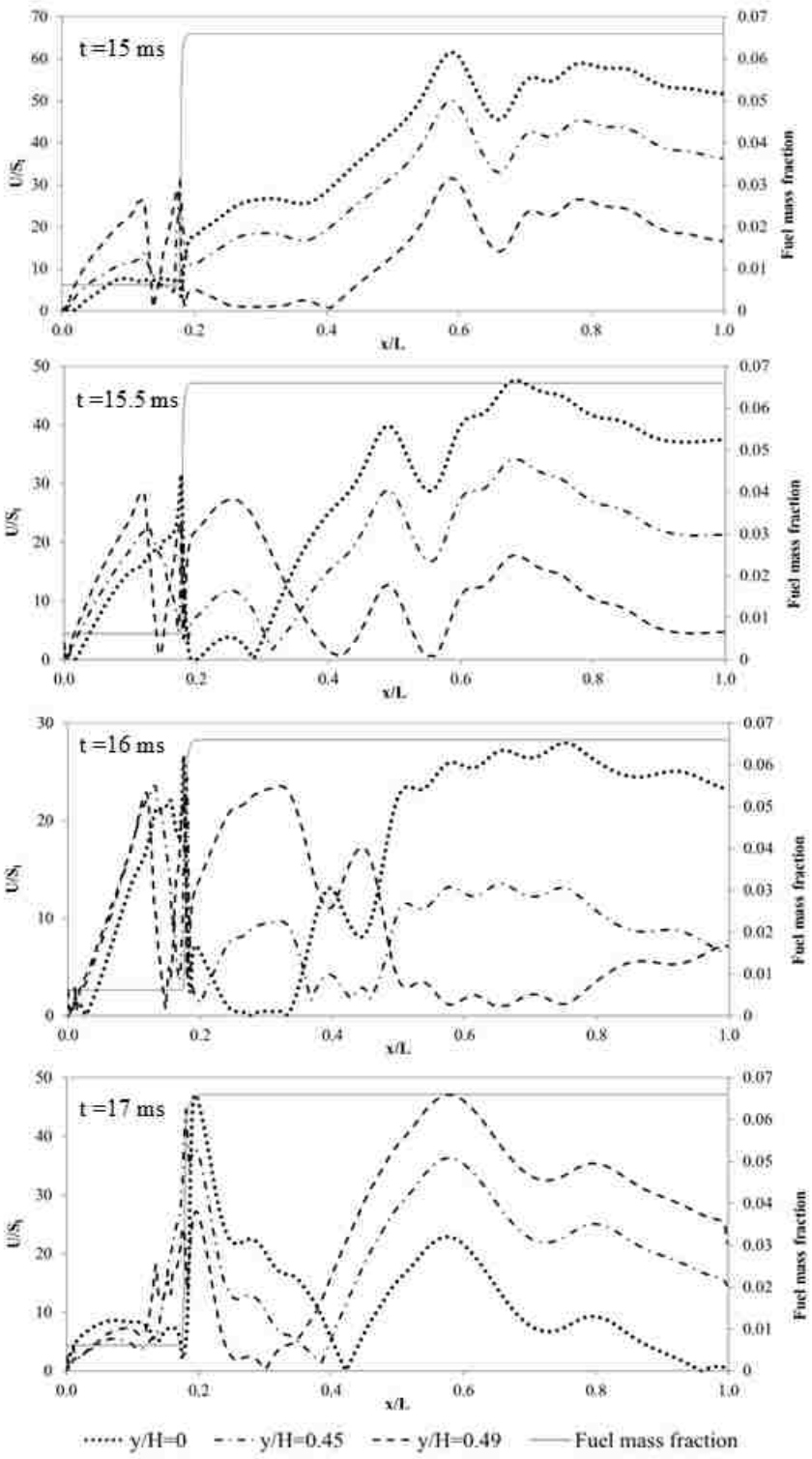

Figure 6.7: Normalized velocity distribution and fuel mass fraction along the duct length at different times during the tulip flame formation for y/H = 0, y = 0.45 and y/H = 0.49 cross-sections (part A). Note change of the vertical axis value from graph to graph.

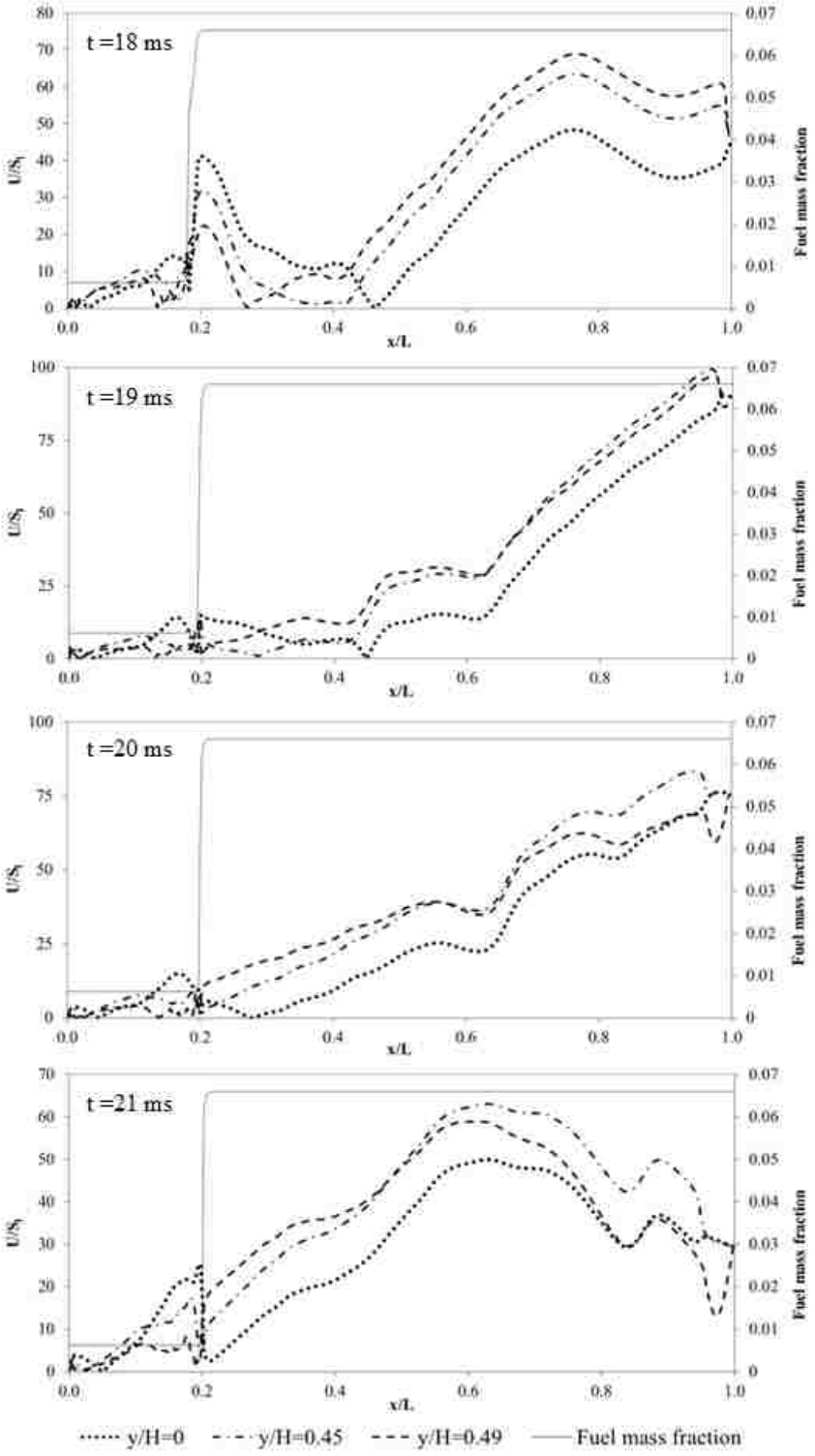

Figure 6.8: Normalized velocity distribution and fuel mass fraction along the duct length at different times during the tulip flame formation for y/H = 0, y = 0.45 and y/H = 0.49 cross-sections (part B). Note change of the vertical axis value from graph to graph.

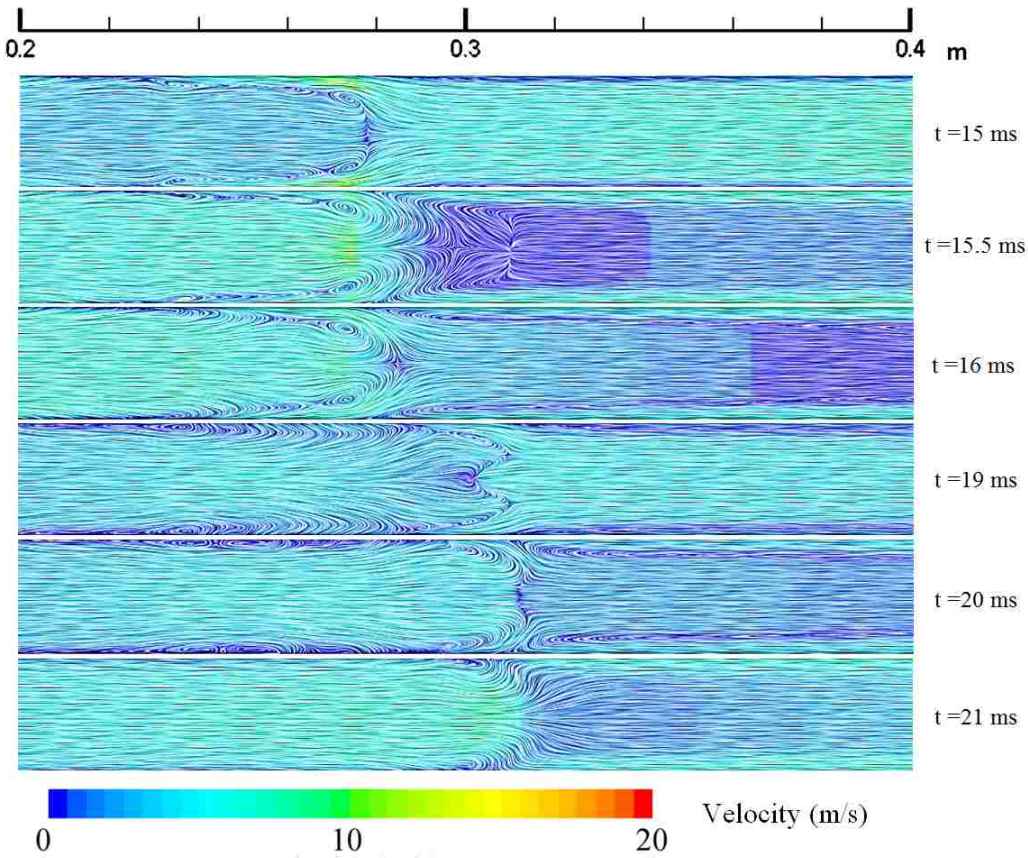

Figure 6.9: Velocity line integral convolution at the tulip formation zone.

Figure 6.9 shows the velocity line integral convolution (LIC) at the tulip formation zone from numerical results (laminar combustion model). At each time step of flame propagation and as the flame starts touching the wall vortices form along the top and lateral parts of the lateral flame.

These vortices can be seen at t = 15 ms, a moment before tulip onsets. Another important point is the creation of vortices ahead of flame and attached to the duct wall.

At t = 15.5 ms, the enlargement of vortices before flame front coupling with fluid motion (caused by the vortices ahead of flame) starts the dent in the flame front surface.

At t = 16 ms, the vortices ahead of flame are becoming larger, causing a larger

flame splits.

At t = 19 ms the vortices ahead and behind the flame becomes weaker, and the lips of flame start collapsing.

At t = 20 ms, the vortices behind the flame front and ahead of flame have almost equal size. This can finish the collapsing step. It also causes the flat flame.

Finally at t = 21 ms, the finger flame forms again by the help of remaining vortices behind the flame. This also helps the flame to move forward with a absence of resistance coming from eddies ahead of flame.

Figure 6.10, 6.11 and 6.12 show the normalized x component (horizontal) of velocity distribution during the tulip flame for the cross-sections x_1, x_3 and x_5 at the left side and their relevant velocity line integral convolution at the right side. These plots help to find the direction of flow velocity at each time step and the corresponding vortices effects prior and during the tulip flame formation.

At t = 14.5 ms, the flame front has a flat shape and it is tangential to the cross-section x_1. The x velocity component along all the three cross-sections is positive and all profiles have a similar pattern. Only the cross-section x_1 has slightly lower velocity right after the wall detaching point and as it approaches the duct centre.

At t = 14.75 ms, the flame front keeps its flat shape while it approaches the cross-section x_3. There is also elongation in the flame skirt since the last time step (t = 14.5 ms). The velocity profiles for the cross-sections x_3 and x_5 remain somewhat unchanged and there is a reduction in their magnitude about 20-25 units at all points. The profile along cross-section x_1 retains its trend from previous time step near the wall, however, there is a sudden drop in the velocity between $y/H \approx 0.3 - 0.4$ which is the duct interior. Velocity is then constant until it reaches the duct centre-line. This is the initial sign of the flow direction change.

At t = 15 ms, the flame front approaches cross-section x_3 and more of the flame skirt enlargement also can be seen in comparison to former time step. The cross-

section x_1 is now located on the backside of the flame front. The vertical velocity is increasing when moving towards the duct centre. The velocity then decreases as the duct centre-line is approached. Then, the vertical velocity assumes the negative value as passing the point y/H $\approx$ 0.35. This indicates an opposite direction of flow behind the flame front (burnt side). The velocity profile along the cross-section x_3 is influenced by the eddy created ahead of the flame front and forms tiny 'V' shape near the wall with inverse velocity direction. Moving away from the wall, the velocity direction changes to positive. The cross-section x_5 intersects the centre of the vortex ahead of the near wall flame section. Therefore, after a deep 'V' shape on the negative side, the vertical velocity gradually increases to positive at the point y/H $\approx$ 0.4 and as approaching the duct centre.

At t = 15.25 ms, the flame is almost in the same location as far as the cross-sections x_1 and x_3 are concerned. Since last time step, the flame front becomes more flat. The velocity profile along cross-section x_1 has a positive value and 'Λ' shape between y/H $\approx$ 0.35 – 0.5. When crossing the flame front (y/H $\approx$0.35), the vertical velocity becomes negative clearly differentiating between the flow direction ahead and behind of the flame front. This can be considered as the main reason for the formation of the tulip flame. The cross-section x_3 cuts through two different vortices. It is shaped by the eddy tip that is located ahead of flame and the nearby wall. A tiny 'V' shape velocity profile with a negative value at the wall is the result of this eddy. The other vortex is the larger one and it is located at the upper and lower flame corners. The rest of the cross-section x_3 is affected by this vortex. The velocity has positive direction up to the point y/H $\approx$ 0.3 and then it changes direction as the duct centre cross-section is approached . The cross-section x_5 is crossing through the eddy core, which is ahead of the flame front and nearby the wall. Reverse flow direction between the wall and point y/H $\approx$ 0.4 can be seen. Afterwards, the flow gets a positive value for the rest of the cross-section to the duct centre. It should be

noted that at this moment the vortex ahead of flame front starts moving away from the wall.

At t = 15.5 ms, the flame is almost in the same position as the previous time step, however it starts to travel backwards due to the effect of vortices. The velocity profile along cross-section x_1 has a positive value near the wall and in the vicinity of the flame skirt in the burnt gas. The velocity inverses direction around the duct centre. This shows the vortices effect on the flow path. The velocity profiles along cross-sections x_3 and x_5 remain unchanged since previous time step.

At t = 15.75 ms, the flame front inversion becomes deeper since t = 15.5 ms under combined effect of vortices described at t = 15.5 ms. The velocity profile for all three cross-sections is analogous to t = 15.5 ms except that the negative parts which now have higher magnitude.

At t = 16 ms, the centre of flame front continues its backward movement. The flame front location is still similar to t = 15.75 ms. At this instant the vortex core at fresh mixture (near the cross-section x_5), starts reaching the wall. This could be considered as the pushing effect of the flame tip which is trying to propagate forward. The velocity profile along cross-section x_1 retains its profile from t = 15.75 ms with greater magnitude in both positive and negative directions. The same trend applies for the other two cross-sections (x_3 and x_5).

At t = 16.5 ms, the flame lips are formed completely. Vortices at the flame corners are still present, but they cross the flame, becomes weaker and everything vanishes at later times. At the same time, the eddy ahead of flame and near the wall is also disappearing because of the flame lips propagation. The velocity profile along cross-section x_1 has a positive value from the wall until point $y/H \approx 0.35$ with 'Λ' shape between these points. The rest of the profile is in an inverse flow. The velocity profile along cross-section x_2 passes through the flame lips. It has positive magnitude up to $y/H \approx 0.2$ and then it assumes the negative value as it goes through the duct centre.

It shows the inverse flow direction on the duct centre-line which causes the flame splitting. The velocity profile along cross-section x_3 now has positive value similarly to t = 14.5 ms but with lower velocity magnitudes.

At t = 17 ms, the flame lips are propagating forward and their elongation can be clearly seen. Also, no vortices can be observed ahead of the flame front. Also, there is no inverse flow along any of the three cross-sections. For both cross-sections x_1 and x_3, the velocity profile has '$\bigcap$' pattern between the wall and the duct centre. For the cross-section x_5 which is still ahead of flame, there is a gradual rise in velocity from the wall to the point y/H $\approx$ 0.2. There is a slight reduction in velocity between y/H $\approx$ 0 – 0.2. Large velocity differences exist between the flow ahead of the flame tip (cross-section x_5 – point y/H $\approx$ 0.25) and the flow at the flame intersection on the centre-line (cross-section x_3 – point y/H $\approx$ 0).

At t = 17.5 ms, the flame tip reaches the cross-section x_5. The series of vortices form again almost along the flame skirt and partially at the flame front. These are the eddies which trigger the flame lips collapsing process. The velocity profile along cross-section x_1 has a similar pattern as the previous time step with lower velocity magnitude (about $U_x/S_l \approx 20$ units). The velocity assumes the negative value shortly after the y/H $\approx$ 0.4, which confirms the inverse flow inside the burnt areas. At the cross-section x_3 velocity reduction is much higher on the positive side (between the wall and point y/H $\approx$ 0.3) since the last time step. This difference is smaller on the negative side of velocity. The velocity profile along cross-section x_5 has a similar profile to t = 17 ms but with lower magnitude (about $U_x/S_l \approx 10$ units). This can be speculated as a temporary effect of flame lips converging.

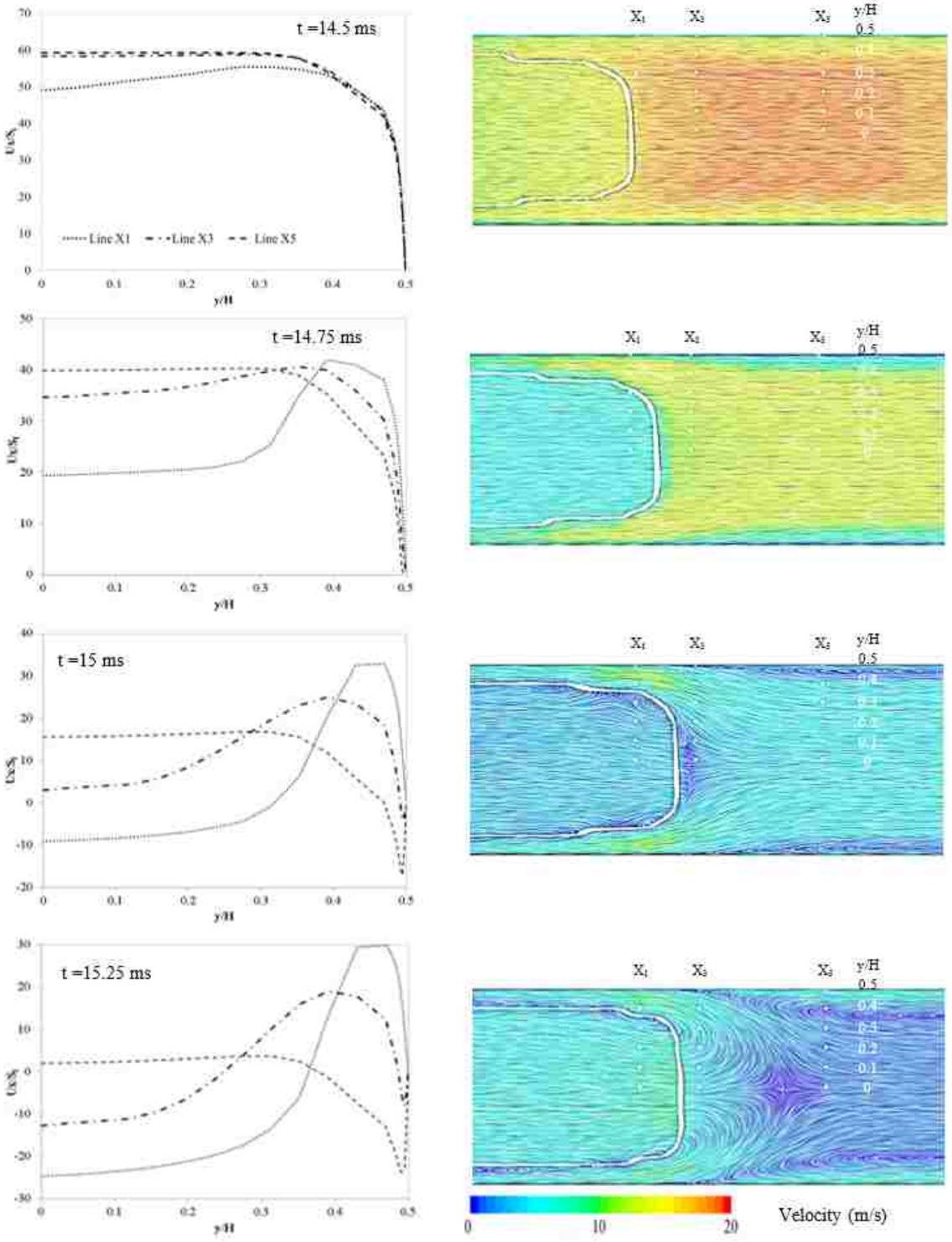

Figure 6.10: Normalized horizontal (x) component of velocity distribution during the tulip flame for the x_1, x_3 and x_5 cross-sections (left), the relevant velocity line integral convolution (right) (Part A).

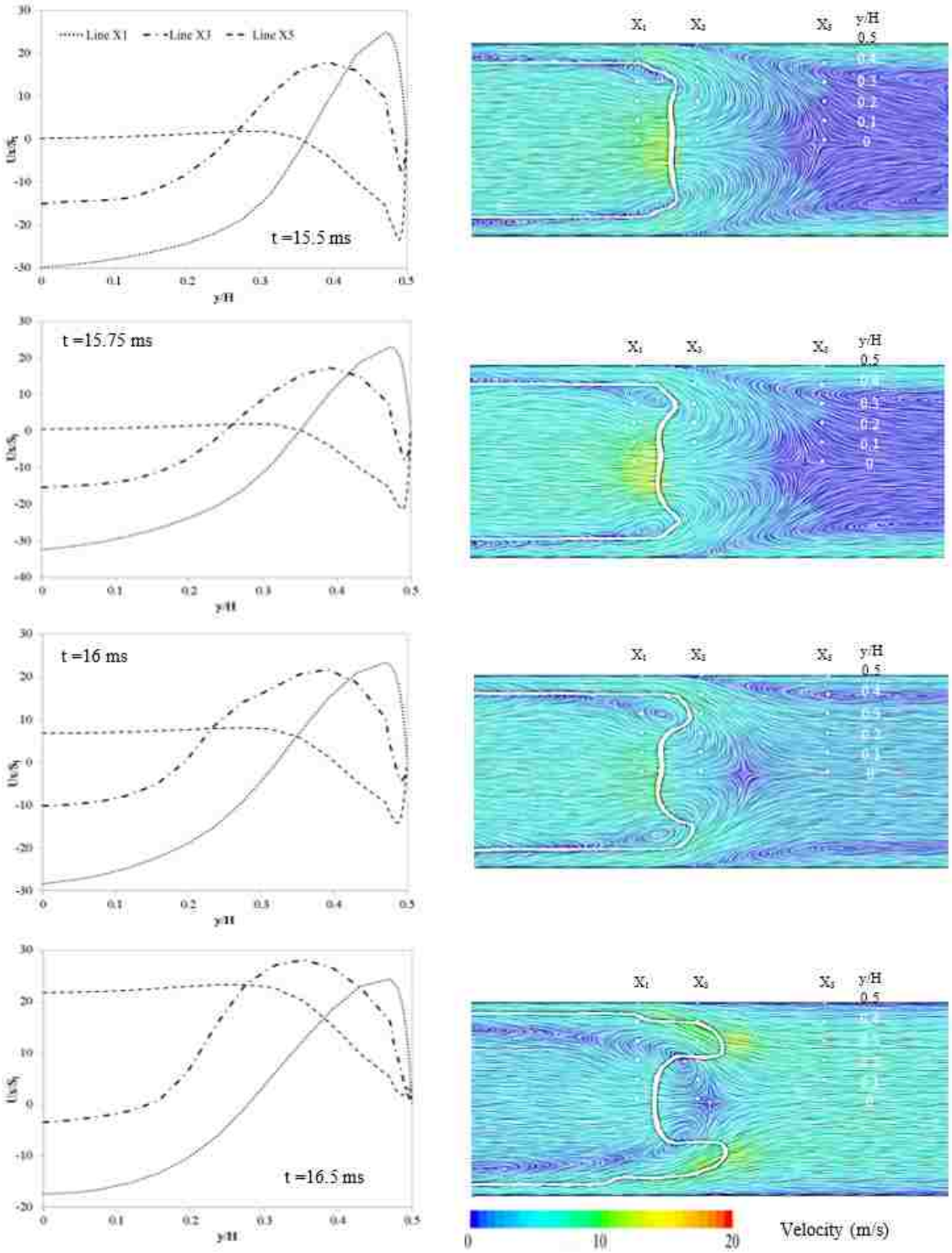

Figure 6.11: Normalized horizontal (x) component of velocity distribution during the tulip flame for the x_1, x_3 and x_5 cross-sections (left), the relevant velocity line integral convolution (right)(Part B).

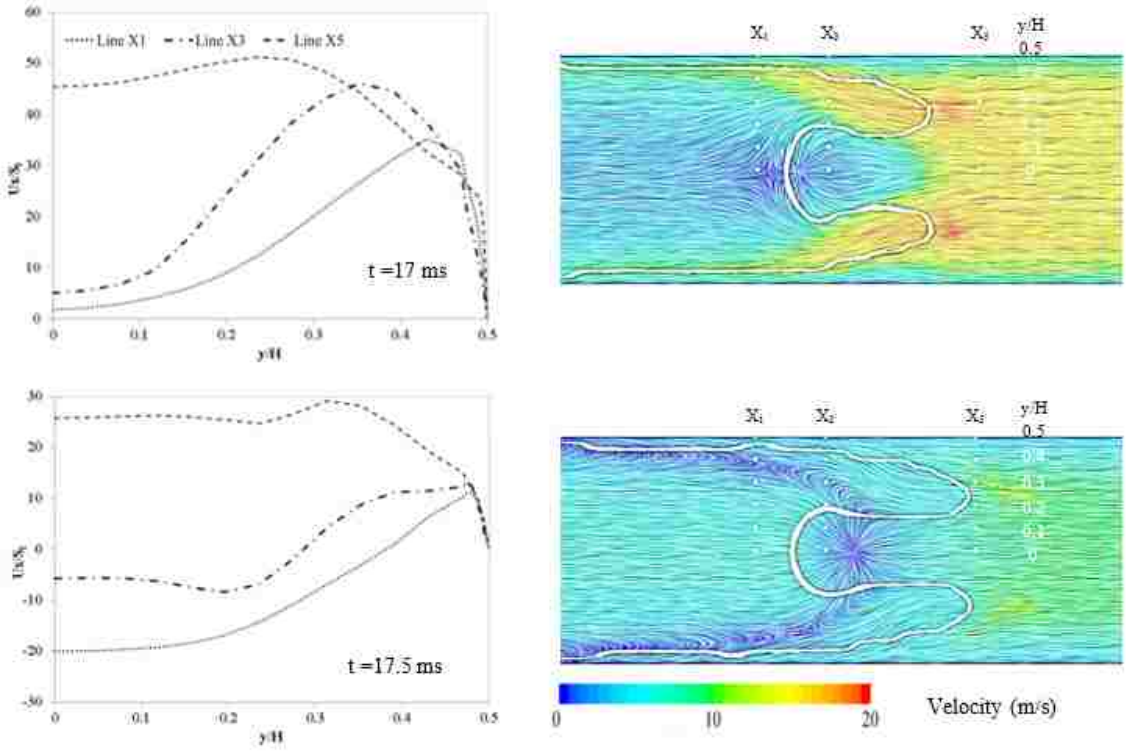

Figure 6.12: Normalized horizontal (x) component of velocity distribution during the tulip flame for the x_1, x_3 and x_5 cross-sections (left), the relevant velocity line integral convolution (right)(Part C).

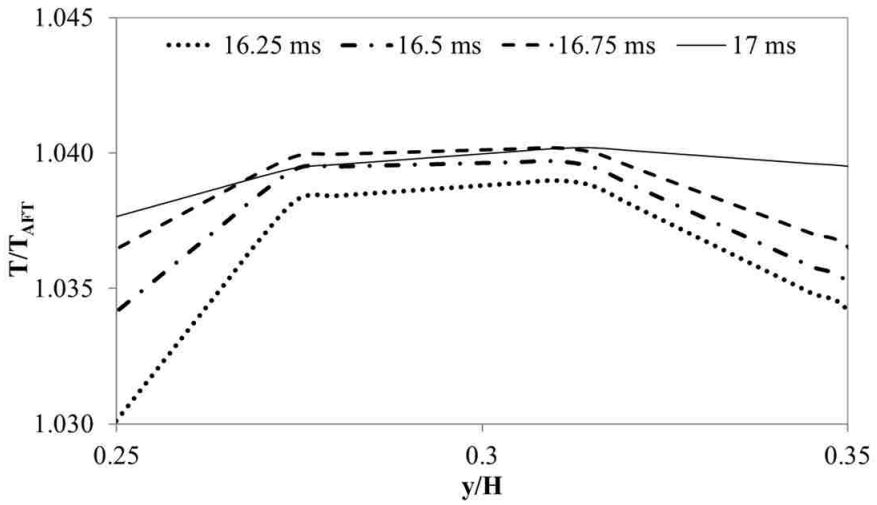

Figure 6.13: Normalized temperature during the vortices disappearance process for the cross-section x_2 at the vicinity of y/H = 0.3 location. The T_{AFT} is the adiabatic flame temperature and calculated to be 2265 K.

Figure 6.13 shows a normalized temperature during the vortices disappearance process for the cross-section x_2 at the vicinity of y/H = 0.3 location. The T_{AFT} is the adiabatic flame temperature which is calculated to be 2265 K. Considering the vortex reaction process between t = 16.5 ms and 17 ms in Figures 6.11 and 6.12, this plot is trying to find the vanishing rate and its effect on the flow. As expected, the eddy break-up should locally increase the flow temperature.

The point y/H = 0.3 of the cross-section x_2 is selected in a way to be in the vortex at the burnt gas. However, the temperature is high at the burnt gas region, and there is a general trend of temperature increase between t = 16.25 ms and 16.75 ms. At t = 17 ms as the next set of vortices start forming, a decrease in temperature occurs.

It is expected that the heat transfer from the flame forward movement increases the temperature continuously. Therefore, it is speculated that this slight oscillation in temperature magnitude can relate to the vortex disappearance and creation processes.

6.2.2 Pressure distribution at tulip flame formation zone

The figure 6.14 shows the normalized absolute total pressure distribution and fuel mass fraction at different times during the tulip formation at the duct centre-line (y/H = 0). The pressure has been normalized by the initial pressure at the duct. The mass fraction curves show the flame position and identify the reactants and products sides of the flame. For all-time steps, the constant lines of pressure can be seen on the product side of the flame. As the flame front passes through, rapid variations of the pressure are occurring in this region. Considering that the tulip formation starts at about t = 15 ms, the pressure decreases from its value at t = 13 ms to t = 15 ms. Then, it increases in the next time steps (from t = 15 ms to t = 20 ms).

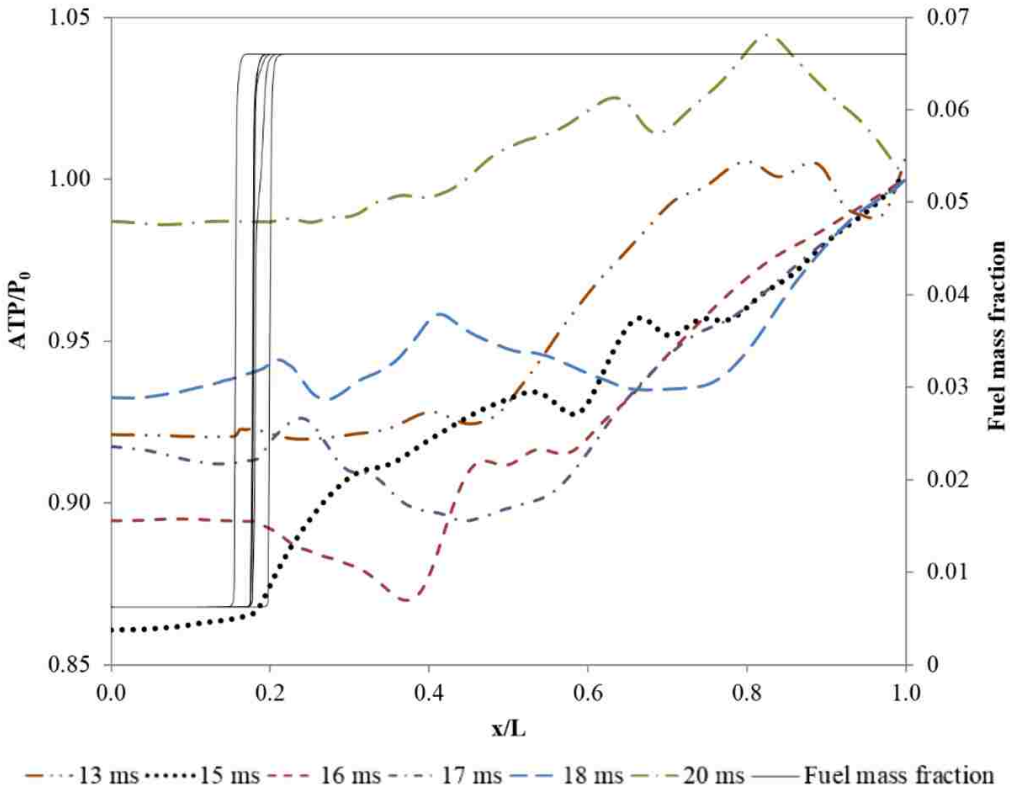

Figure 6.14: Normalized absolute total pressure distribution and fuel mass fraction at different times during the tulip flame formation for y/H=0 line (centre-line). P_0 is the initial pressure.

Figure 6.15 shows the absolute total pressure at different times between the flame-wall first touch and the tulip formation, and for the different points at the top wall side (based on numerical laminar combustion model). This plot gives a better understanding of the pressure wave (either compression or expansion wave) formation and consequently their effect on the creation of the tulip flame. To be able to explore this idea comprehensively, four points, x = 11, 15, 19 and 23 cm are chosen and plotted separately in Figure 6.16.

As Figure 6.16 illustrates, the compression wave is emitting to the wall as the flame approaching the wall (pressure rise before t $\approx$ 9.2 ms). After the first flame-wall touch (t $\approx$ 9.2 ms), the pressure reduces. In other words, after the touch, the expansion wave onsets. But this reduction does not take long (expansion wave is

not powerful enough) and it is overpowered by the next set of the compression wave. Therefore, the pressure wave starts increasing again. As time progresses, it is expected to have more area of the flame skirt approach and eventually touch the wall. The series of 'Λ' and 'V' shapes between t ≈ 9 – 10.2 ms are illustrating this idea. The interesting point can be brought up as the large strong pressure reduction occurs after t ≈ 10.2 ms which is approximately the same for all x locations (considering expected slight delay). Generation of these expansion waves continues until the tulip flame initiation (about t ≈ 14.8 ms). The superimposing of these expansion waves on themselves can lead to the flame flat formation (through instability of flame front) and finally the tulip flame.

Considering the vorticity Equation (6.1), specifically the second term on the right hand side that is called baroclinic torque. This term is responsible for the vortex generation from unequal acceleration as the result of the nonaligned density and pressure gradients [52].

$$\frac{D\omega}{Dt} = -\omega\left(\nabla.V\right) + \frac{\nabla\rho \times \nabla P}{\rho^2} + \left(\omega.\nabla\right)V + \frac{1}{Re}\left(\nabla^2\omega\right) \tag{6.1}$$

where ω is the vorticity vector (equal to the curl of the velocity field), V is the velocity vector, ρ is the density, P is the pressure and Re is the Reynolds number.

Figure 6.16 shows about 17 KPa (0.17 atm) pressure reduction just before the tulip flame formation. Based on the Shalaby et al. [53] and Teerling et al. [54] studies, the RT instabilities occur and subsequently, vortices form as the pressure wave amplitude is on the order of 1 KPa or higher. Xiao et al. [8] also arrived to this point in his results. Furthermore, the misalignment of the density gradient and the pressure gradient can also result in baroclinic torque generation, which in turn can intensify the vortex formation, especially at the curved flame surface.

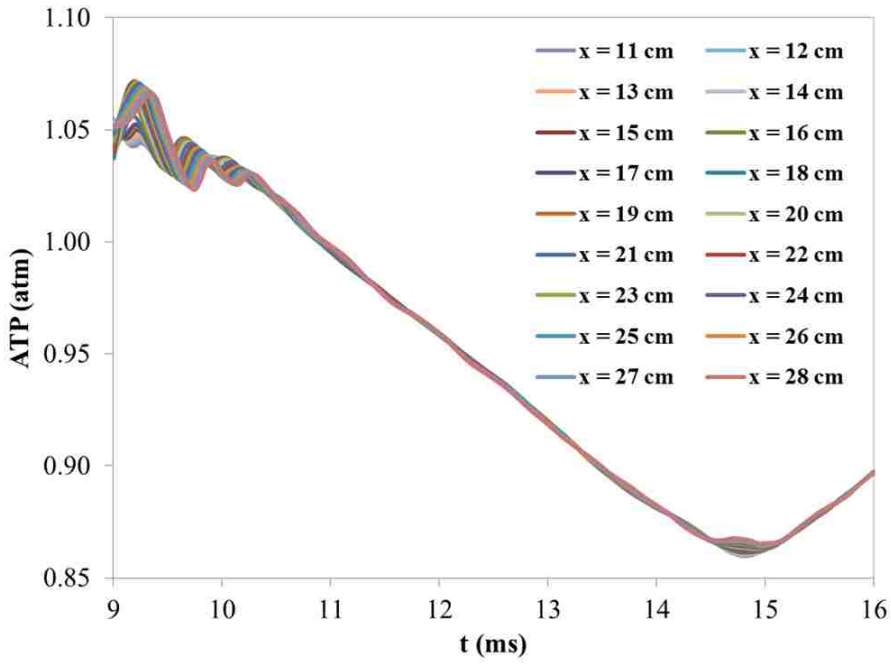

Figure 6.15: Absolute total pressure at different times between the flame-wall first touch and the tulip formation for the different points at the wall (x= 11 – 28 cm).

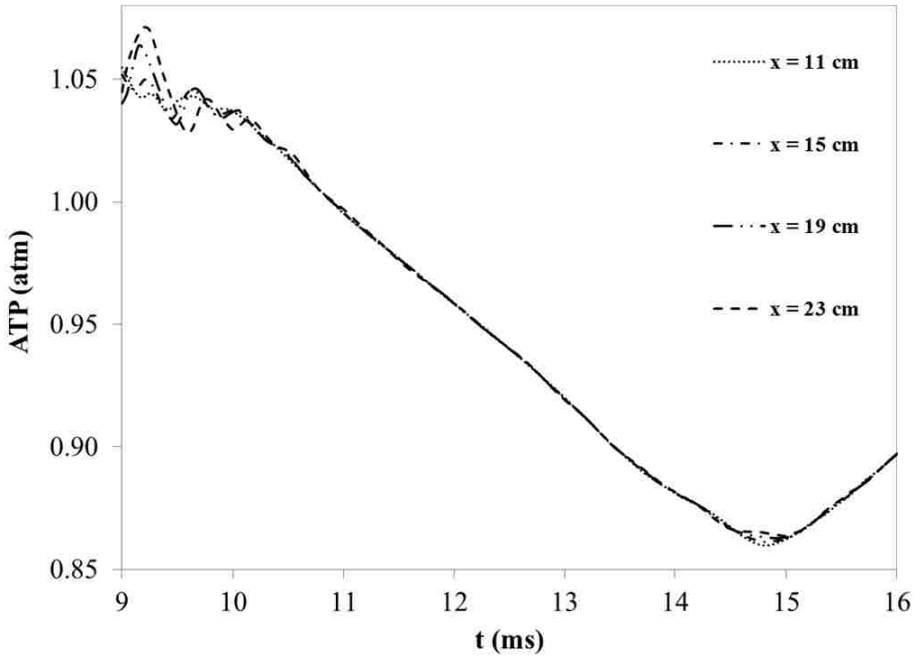

Figure 6.16: Absolute total pressure at different times between the flame-wall first touch and the tulip formation for the different points at the wall (x= 11 – 23 cm).

6.3 Flame-wall first contact

Figures 6.17 and 6.18 plot the normalized absolute pressure distribution at different times during the flame – wall first contact for x = 10.55 cm. The results are based on the numerical simulation (laminar combustion model). The pressure is normalized by initial pressure (P_0). Also, the H is the duct height. It should be noted that the pressure changes for small time steps (up to 0.001 ms) are very large. Therefore in order to show the pressure curve differences clearly at each time step, it is required to plot each time step separately rather than using one graph.

At t = 9.210 ms as the lateral part of flame is approaching the duct top wall, the pressure reduces gradually. Lower pressure is present close to the wall and the pressure rises as moving away from the wall. Then the pressure becomes constant for the rest of the dimension until duct centre point.

At t = 9.220 ms, the wall senses the approaching flame. The pressure has risen since the last time step.

At t = 9.240 ms, the pressure curve returns to its form at t = 9.210 ms but with higher pressure values.

At t = 9.260 ms, the pressure curve shows the same trend as the last time step. This is despite the fact that the pressure keeps increasing gradually at the duct centre (rather than keeping its constant value). The peak of pressure is now located at the duct centre. Again the pressure increases slightly in comparison to the previous time steps.

At t = 9.270 ms, the peak of pressure moves closer to the wall (y/H=0.4), and it decreases sharply at the duct centre. Another interesting point here is the pressure reduction along the entire height of the duct.

At t = 9.290 ms, the pressure generally decreases at all points. The pressure changes somewhat next to the wall and it is as high as the peak pressure at this time step. Also, a 'M' shape starts to form with a much lower value on the wall side.

At t = 9.292 ms, the pressure values keep decreasing at all points. Now the 'M' shape of the profile has a higher value on the right side compared to the last time step.

At t = 2.293 ms, the pressure decreases again at all points. The value of maximum at the wall side increases. By now, the profile curves noticeably. At t = 2.294 ms, the reduction of pressure continues. The pressure has the same trend as at the last time step, except for the centre point where the pressure is increasing.

At t = 2.296 ms, the pressure decreases along the height. The peak pressure occurs at the centre-line. The pressure close to the wall is reduced in comparison to the centre-line in contrast to what occurred in the last time step.

At t = 9.298 ms, the pressure reduces at all points retaining the same profile. The only difference is the pressure reduction at the wall side.

At t = 9.340 ms, the 'M' shape has disappeared completely. Pressure reduction occurs at all points in this time step as well. Moreover, in contrast to previous time step, the pressure close to the wall increases compare to other points. It assumes the 'Λ' shape close to the wall, and it is reduced at the duct centre following a straight line.

At t = 9.350 ms, the trend of pressure reduction at all points continues. The profile of 'Λ' shape close to the wall elongates and it forms 'U' shape in the duct centre. There are also two maximums, one at the centre-line and one at the wall.

At t = 9.400 ms, the trend of pressure reduction in all points continues. But the bottom of 'U' shape deforms into the 'ω' shape.

After multiple time steps at t = 9.420 ms, the pressure starts increasing at all locations and the profile resembles first time step in this figure (t = 9.210 ms).

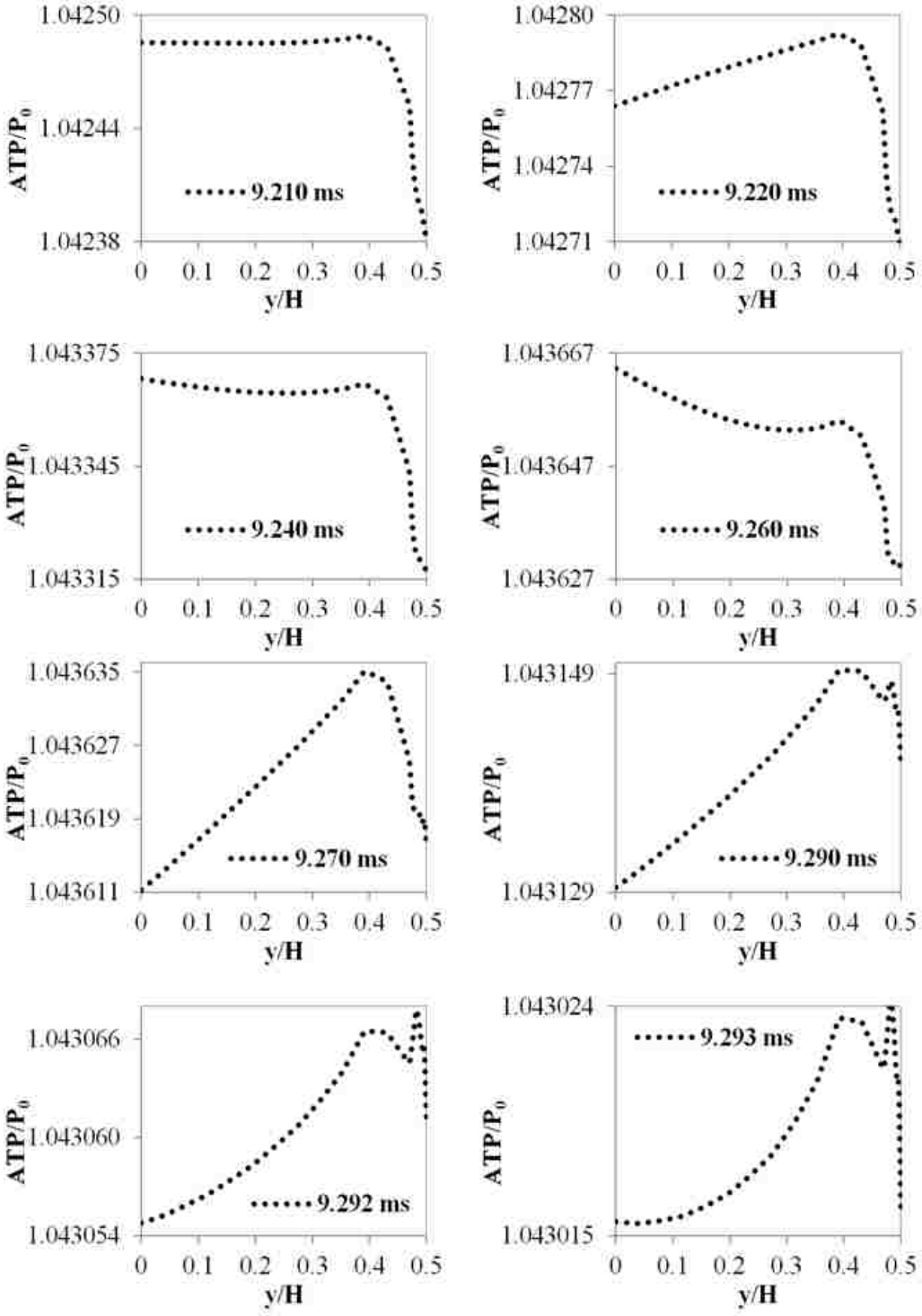

Figure 6.17: Normalized absolute total pressure distribution at the different time steps during the flame-wall touch for x/L=0.0659 cross-section (x=10.55 cm, the flame-wall first contact)(Part A).

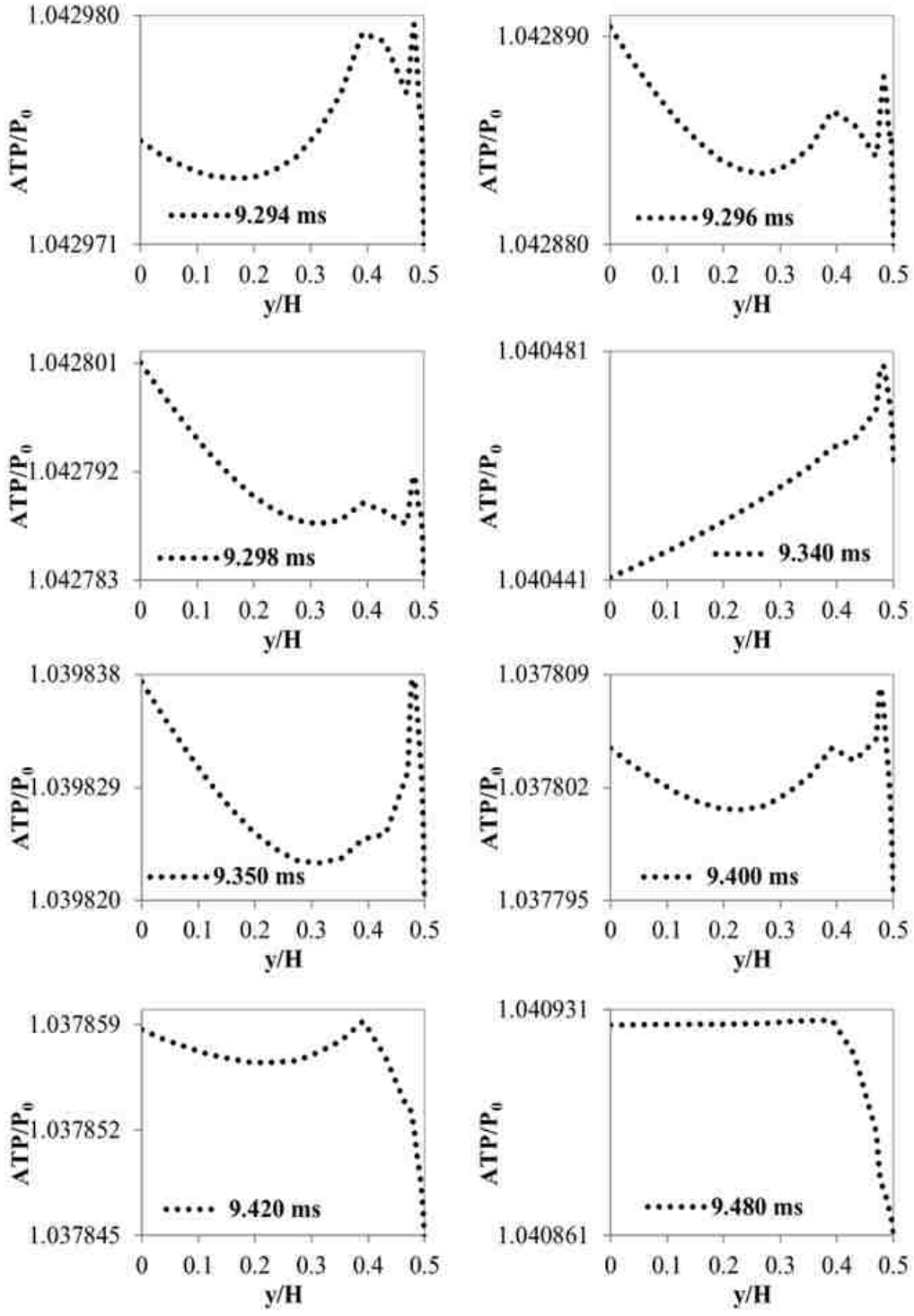

Figure 6.18: Normalized absolute total pressure distribution at the different time steps during the flame-wall touch for x/L=0.0659 cross-section (x=10.55 cm, the flame-wall first contact)(Part B).

At t = 9.480 ms, the pressure profile is back to the shape at the initial step (t = 9.210 ms). This can be considered as the end of flame-wall contact at its first occurrence. As the flame touches the wall, it creates the pressure wave which propagates to the duct centre. As the pressure wave develops it creates eddies at the flame edges as it was described in the previous section. These eddies contribute on the flame front shape changes and finally the tulip formation.

6.4 Collapse of tulip flame

Figures 6.19, 6.20, 6.21 and 6.22 show the velocity line integral convolution (top), the normalized x component of velocity for the x_3, x_4, x_5 and x_6 cross-sections (left) and the normalized y component of velocity for the y/H = 0.148 cross-section (right) during the flame lips collapse.

At t = 17 ms, the tulip flame depth is still increasing. All four cross-sections have a positive x direction velocity component (U_x). Although for the cross-sections x_3 and x_4, which are on the flame back side, the velocity increases gradually from the wall and then it reduces sharply as approaching the duct centre. The two cross-sections x_5 and x_6, which are in front of the flame, have constant value of U_x after gradual rise near the wall. Of interest at this instant is the y component of velocity along the duct length at the y/H = 0.148. This cross-section is parallel to the flame lip inner surface. The right graph demonstrates that the U_x velocity is oriented upwards from x/L=0.1775 until the almost midpoint between the cross-sections x_3 and x_4. The U_x velocity then becomes negative indicating the downward movement of the flame leading edge.

At t = 17.5 ms, the depth of the flame centroid well still increases since last time step. The $\overline{u}_x$ velocity magnitude drops for all four cross-sections. Now, the central parts of the cross-sections x_3 and x_4 have backward movement. The other two cross-sections x_5 and x_6 retain their profiles from t = 17.5 ms. The U_y velocity for the

cross-section y/H = 0.148 still has positive direction but with a lower value before the cross-section x_4. After passing the cross-section x_4, the velocity gets decreased at almost all points until the cross-section end.

At t = 18 ms, the depth of tulip well is at its maximum point. The U_x velocity for the cross-sections x_3 and x_4 are similar. Albeit, the cross-section x_3 which is tangential to the backside of the flame indentation becomes negative around y/H $\approx$ 0.3. The U_x profile along cross-section x_5 has the same profile but with a lower magnitude. TheU_x profile along cross-section x_6, which is now ahead and close to the flame front, has increased since the last time step. The U_y profile along cross-section y/H = 0.148 has upward direction, as the effect of vortices on that area, up to the cross-section x_5. The U_y then becomes negative ahead of the flame front tip.

At t = 18.5 ms, the U_x profiles along cross-sections x_3 and x_4 which are on the rear side of the flame have negative velocities at all points. The cross-section x_5 is crossing through the flame lips and it dissects different vortices. Therefore, the U_x profile gets a positive value between the wall and the point y/H = 0.4. Then it becomes negative as it is crossing the flame lip. The U_x profile along cross-section x_5 has a positive direction in the flame central part which indicates the forward movement of the flame at those locations. The cross-section x_6 is tangential to the flame tips and the U_x has a positive values at all of its points. The U_y velocity has upward orientation especially along the interior of the flame well.

At t = 19 ms, the merging process of flame lips continues and the flame tip crosses the cross-section x_6. For the cross-sections x_3, x_4 and x_5, which are located at the far rear side of the flame front, the profiles of the U_x velocities are similar. The U_x has a positive value near the wall and then it assumes the negative value for the rest of the cross-section while approaching the duct centre. Similar to the cross-section x_5 in the previous time step, the cross-section x_6 is crossing the flame tips. The U_x profile has positive value near the wall, it increases until y/H $\approx$ 0.4 and

then changes significantly in the unburnt mixture area that is still exist between the flame (shorter) lips. The U_x velocity then rises again as approaching the duct centre. The U_y velocity profile for the cross-section y/H = 0.148 has a negative value up to the mid-point of cross-sections x_5 and x_6(in the combustion products). The velocity then gets upward orientation.

At t = 19.5 ms, the flame centriod well moves forward. The U_x for the cross-sections x_3, x_4 and x_5 are almost similar to the previous time step with approximately the same magnitude. The profile of U_x along cross-section x_6 also retains its trends from previous time step, between the wall and the point y/H $\approx$ 0.2. The velocity then increases from $U_x/S_l \approx$ -13 to almost zero as reaching the duct centre. The U_y velocity profile along the cross-section y/H = 0.148 now has large region with a negative value. The U_y velocity profile just before the cross-section x_6 becomes positive.

At t = 20 ms and t = 21 ms the collapse of flame lips is in its final stage. The U_x velocity does not change considerably for all the four cross-sections in comparison to the previous time step. At t = 20 ms and t = 21 ms, the U_y velocity for the cross-section y/H = 0.148 has analogous trends and magnitudes. It has somewhat negative values around the x/L = 0.1775 for the cross-section x_5. For larger distances it rises gradually and becomes positive for a short distance and then it assumes negative values again at the end of this cross-section.

Between time steps 18 ms and 20.5 ms, the flame suddenly moves into the well interior and consumes the unburnt mixture, which was surrounded for a long time (since t = 17 ms) by the flame inner lips. The flow direction prevents the flame to enter this unburnt area (as described in details before). During this period, the enclosed mixture is always in contact with the flame hot surface (except at front points). That causes the temperature to rise due to the heat conduction which accelerates the weakened flow and it pushes the flame forward. Additionally, it is due to the "thermal

explosion" of the tulip flame interior as also evident by the foot moving combustion products to the back of the duct. In fuel the U_x of the local is higher than U_y forward.

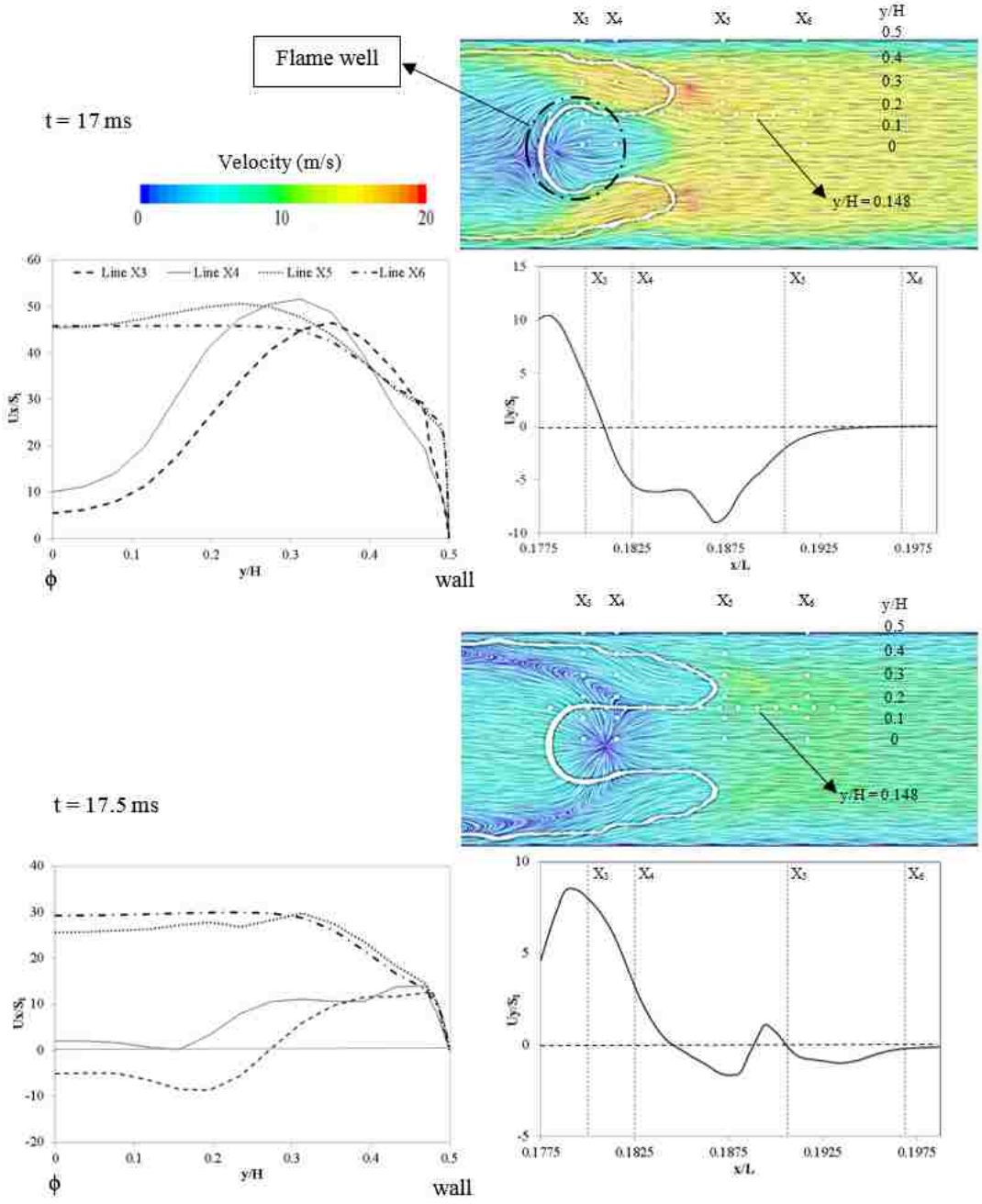

Figure 6.19: Velocity line integral convolution (top), normalized x component of velocity (U_x) for the x_3, x_4, x_5 and x_6 cross-sections (left) and normalized y component of velocity (U_y) for the y/H = 0.148 cross-section (right) during flame lips collapsing after tulip phenomenon (Part A).

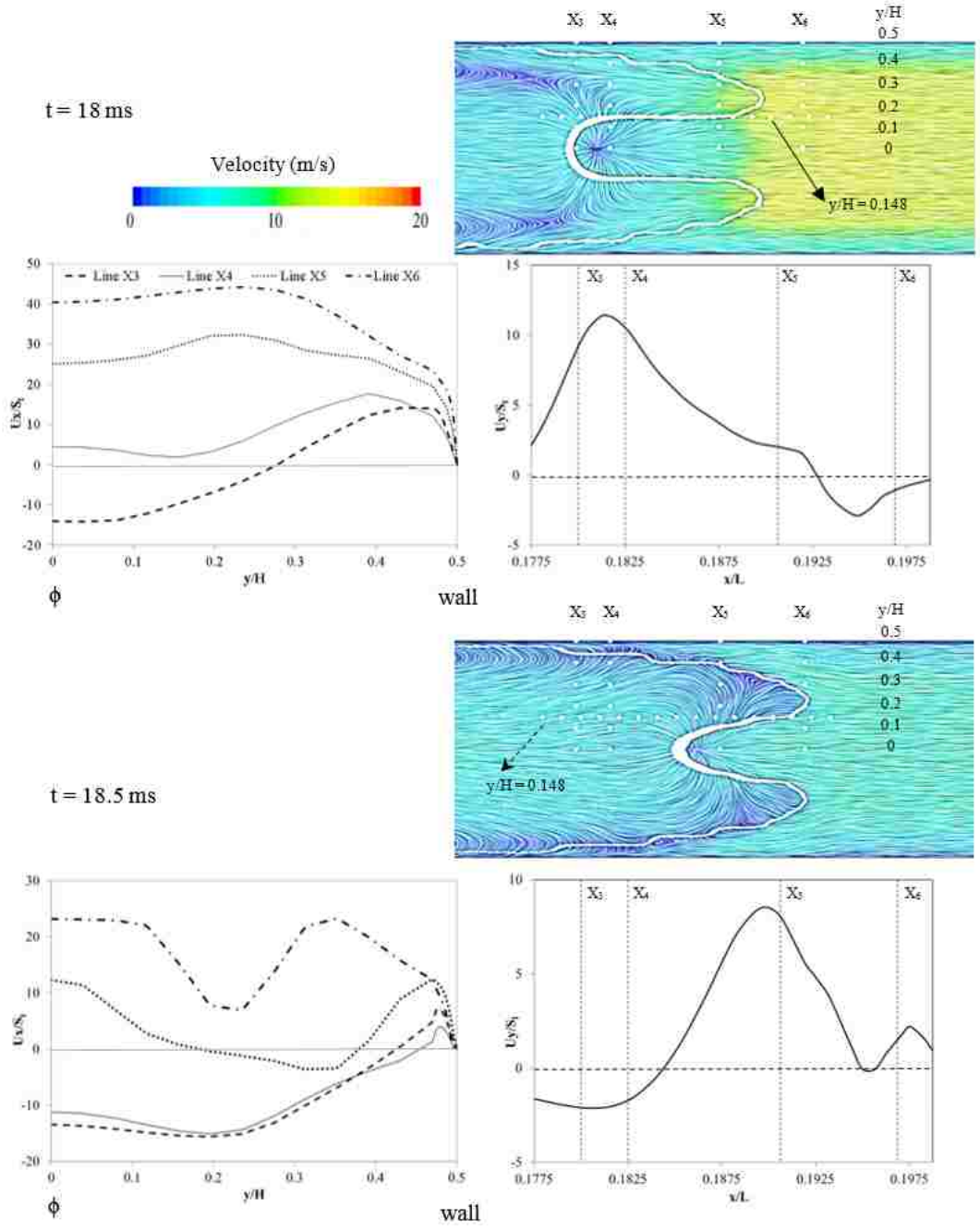

Figure 6.20: Velocity line integral convolution (top), normalized x component of velocity (U_x) for the x_3, x_4, x_5 and x_6 cross-sections (left) and normalized y component of velocity (U_y) for the y/H = 0.148 cross-section (right) during flame lips collapsing after tulip phenomenon (Part B).

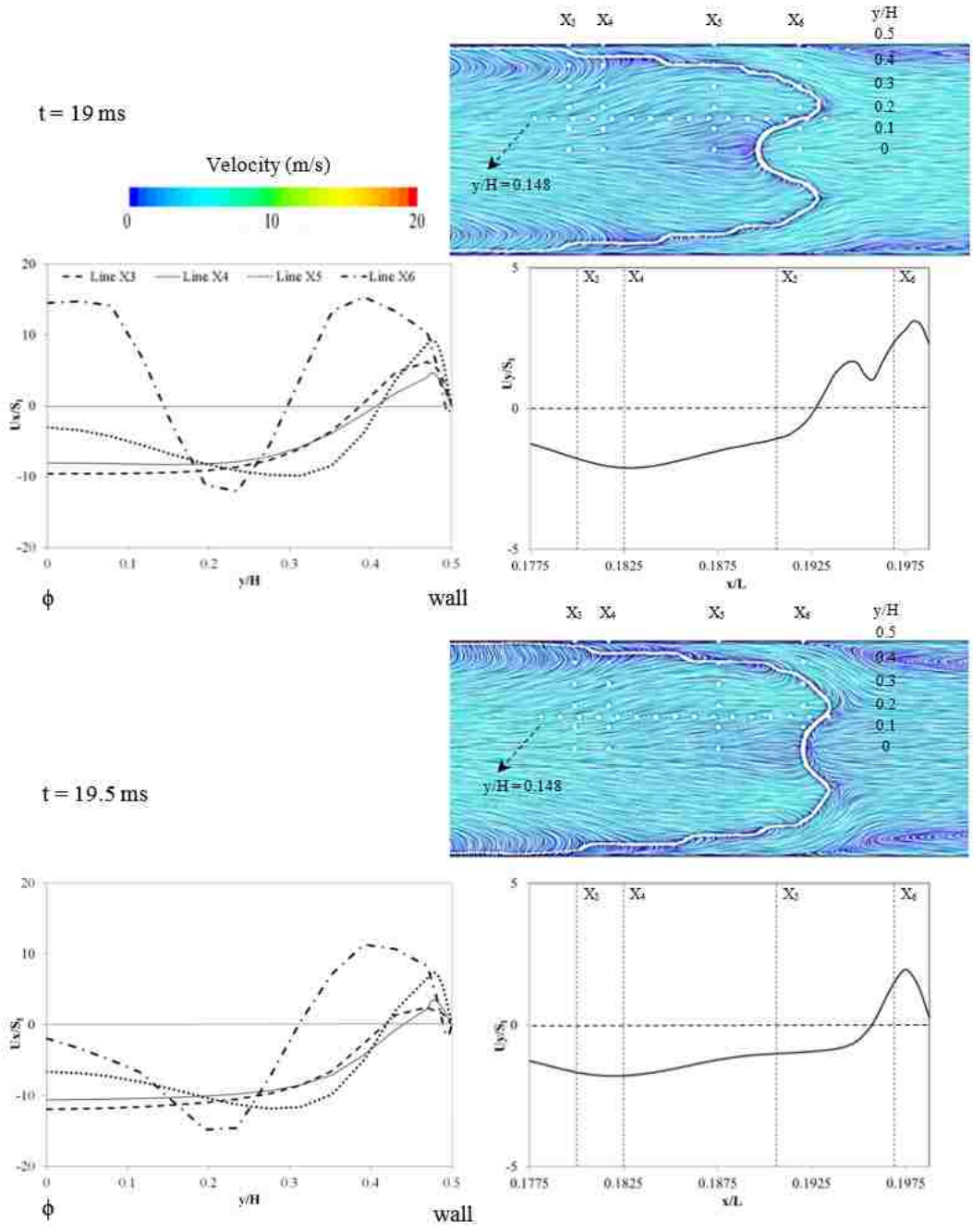

Figure 6.21: Velocity line integral convolution (top), normalized x component of velocity (U_x) for the x_3, x_4, x_5 and x_6 cross-sections (left) and normalized y component of velocity (U_y) for the y/H = 0.148 cross-section (right) during flame lips collapsing after tulip phenomenon (Part C).

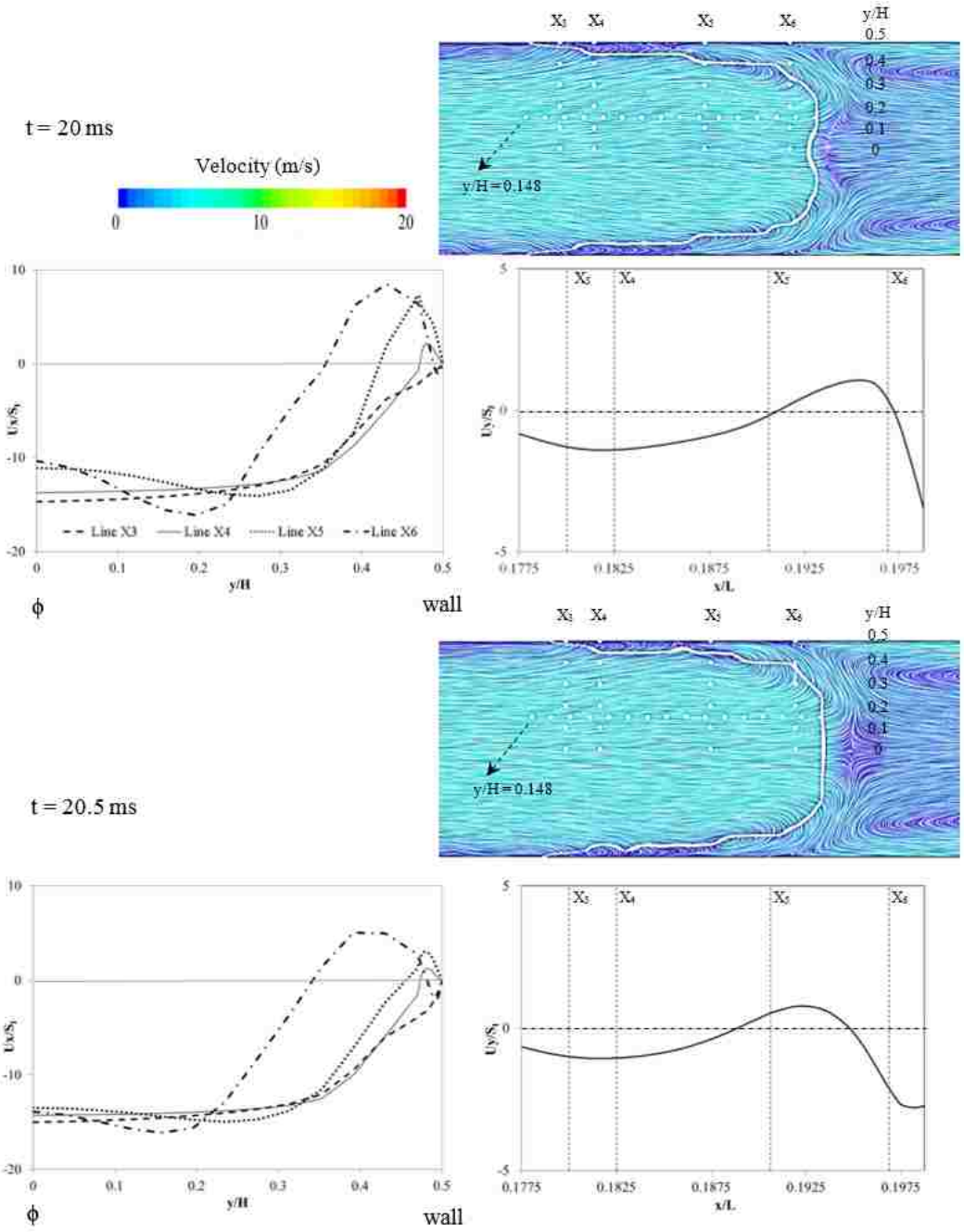

Figure 6.22: Velocity line integral convolution (top), normalized x component of velocity (U_x) for the x_3, x_4, x_5 and x_6 cross-sections (left) and normalized y component of velocity (U_y) for the $y/H = 0.148$ cross-section (right) during flame lips collapsing after tulip phenomenon (Part D).

6.5 First flame inversion

Figures 6.23 and 6.24 show the flame surface (fuel mass fraction margin between 0 and 0.06) evolution during the first flame inversion formation. The cross-sections x_7-x_{12} show in these figures will be used in the following graphs to explore the pressure and velocity distribution ahead, at and behind the first inversion flame.

At t = 38 ms the finger shape flame starts flattening. This flat surface is still present at t = 38.5 ms.

At t = 39 ms, an indentation appears in the flame front. From this instant until t = 40 ms, the flame moves forward while the indentation deepens. The depth of this indentation is not like the one on the tulip flame. This is one of the main differences between the first inversion and the tulip flame.

At t = 41.5 ms the flame propagates forward as the indentation becomes narrower. At the same time, the flame skirt reduces its size.

At t = 43 ms, the indentation disappears while the flame front becomes elongated. From t = 43.5 ms to t = 44 ms, the flame front does not change much as the flame front travels ahead.

At t = 46 ms, the flame centreal part moves very fast in comparison with the flame skirt.

At t = 48.5 ms, the flame front assumes the finger shape again. The flame speed increases at the last two time steps.

At t = 49.5 ms, the finger shape has formed completely. It should be noted that the flame finger shape at this time step (for the first inversion) is different from the flame finger shape of the tulip flame (t = 21 ms at Figure 6.5). The flame here has much longer skirt and it is narrower. This is the last stage on the first inversion phenomenon.

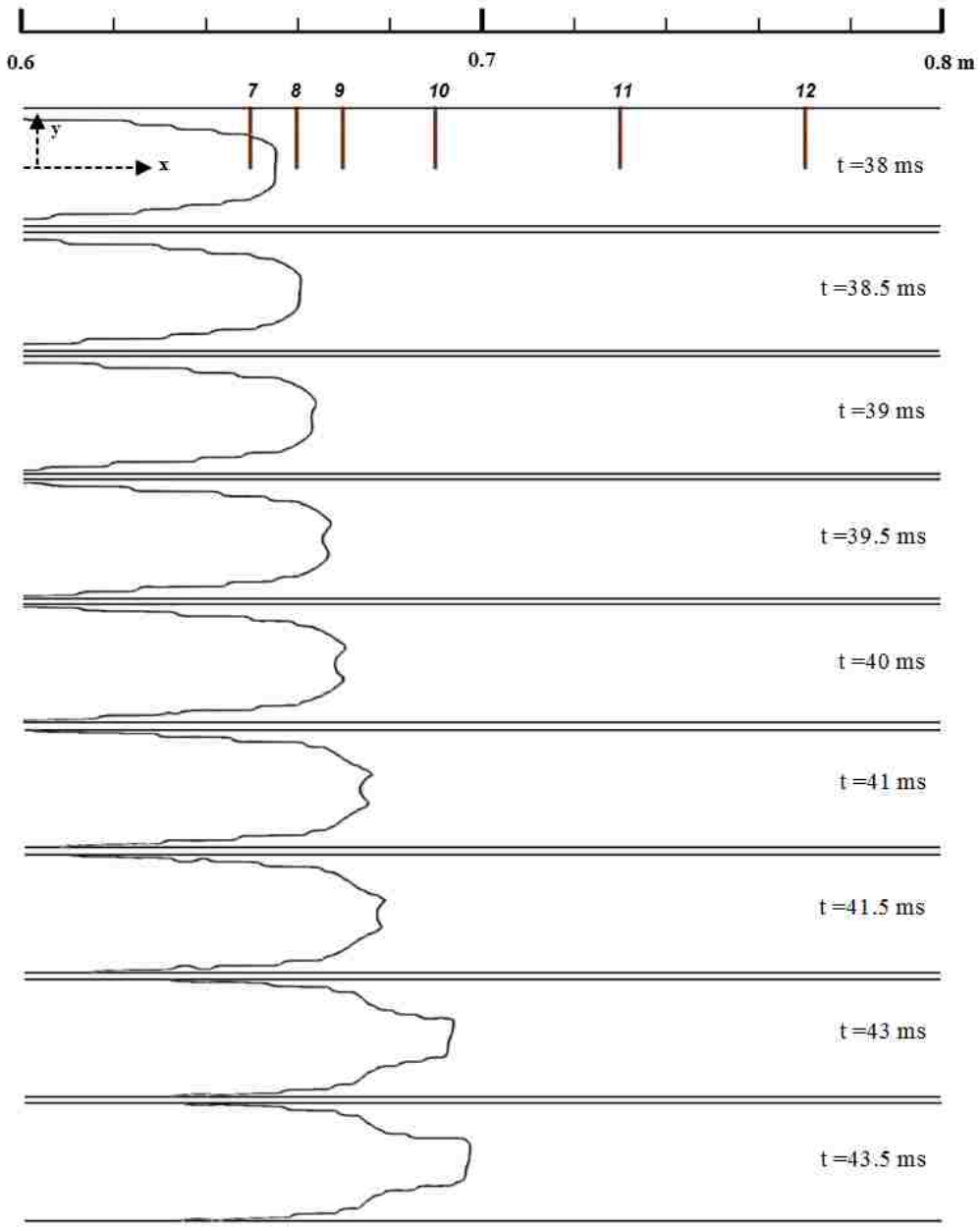

Figure 6.23: Flame surface (marked by the fuel mass fraction margin between 0 and 0.06) evolution during the first inversion formation. Cross-section locations at x_7= 65 cm (x/L=0.4063), x_8= 66 cm (x/L=0.4125), x_9= 67 cm (x/L=0.4188), x_{10}= 69 cm (x/L=0.4313), x_{11}= 73 cm (x/L=0.4563) and x_{12}= 77 cm (x/L=0.4813) (Part A).

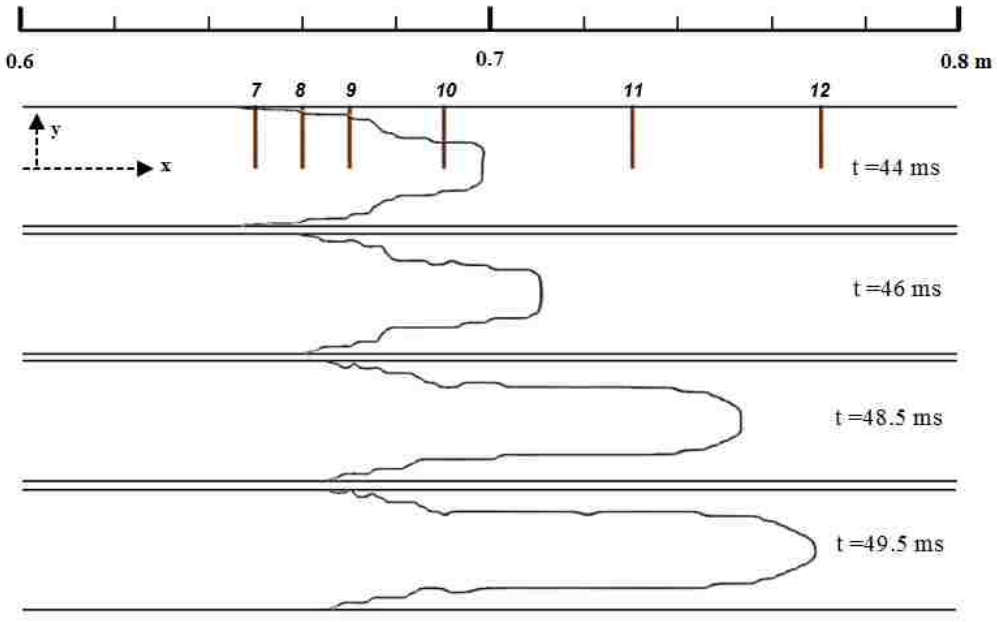

Figure 6.24: Flame surface (marked by the fuel mass fraction margin between 0 and 0.06) evolution during the first inversion formation. Cross-section locations at x_7= 65 cm (x/L=0.4063), x_8= 66 cm (x/L=0.4125), x_9= 67 cm (x/L=0.4188), x_{10}= 69 cm (x/L=0.4313), x_{11}= 73 cm (x/L=0.4563) and x_{12}= 77 cm (x/L=0.4813) (Part B).

6.5.1 Velocity distribution at first inversion zone

Figures 6.25 and 6.26 illustrate the normalized velocity distributions during the first inversion flame for x_7-x_{12} cross-sections. These are selected to illustrate velocity changes ahead and after the first inversion flame front.

At t = 38 ms the flame is in the transition process from the finger shape to the flat profile. The flame tip is located between the cross-sections x_7 and x_8. All the other cross-sections besides x_7 and x_8 are similar to the initial downstream. The flame front is approaching cross-section x_8 and the velocity profile reveals this effect. The velocity profile is similar to those at downstream, but velocity decreases slightly after y/H $\approx$ 0.3 while approaching the duct centre. The flame has already passed the cross-section x_7 and the velocity profile forms '$\bigcap$' shape near the wall and velocity becomes constant ($U/S_l \approx 20$) between y/H = 0 – 0.25.

At t = 38.5 ms the flame is crossing the cross-section x_8. The velocity profile along

cross-section x_7 shows the same distribution as at t = 38 ms, however, the velocity values drop by about 10 units. The velocity profile along cross-section x_8 changes from initial downstream to that at the cross-section x_7. The other four velocity profiles retain their downstream profile, however their magnitude decrease.

At t = 39 ms the flame front indentation appears between the cross-sections x_8 and x_9. The velocity profile along cross-section x_7 has the same pattern as at previous time step but with lower values between the wall and $y/H \approx 0.25$. The velocity is increasing rapidly up to $U/S_l \approx 13$ at $y/H \approx 0.2$ than becomes constant until the duct centre. The velocity profile along cross-section x_8 follows a similar trend as the cross-section x_7 with larger magnitude. The velocity profile along cross-sections x_9-x_{12} preserve their downstream pattern except at the wall. The 'Λ' shaped peak can be seen near the wall. The velocity values at those cross-section are reduced in comparison with the last time step.

At t = 40 ms the indentation deepens at the flame centre and the flame front is now located between the cross-sections x_9 and x_{10}. The flame leading tip is tangential to the cross-section x_9. At this time the flame front has passed through cross-section x_7. The velocity profile along cross-section x_7 is similar to that at the previous time step. Its velocity is lower between the wall and the cross-section middle point. After passing through cross-section middle point, it follows the trend at t = 39 ms with an increase of velocity by about 10 units. The velocity profile along cross-section x_8 follows the same trend as the velocity profile at cross-section x_7. For the velocity profile along cross-section x_9 has the same pattern and magnitude up to $y/H \approx 0.3$. Afterward, the velocity falls to almost zero as it approaches the duct centre. For the other three cross-sections, the velocity profiles are the same as at t = 39 ms with velocity dropping by 5 units.

At t = 41.5 ms, while the flame lips are merging, the velocity profile along cross-section x_7 retains its shape from the previous time step with a lower velocity between

the wall and y/H $\approx$ 0.3. Between the duct centre and point y/H $\approx$ 0.3, the velocity profile again retains the pattern as the previous time step, however, this time has a higher magnitude. The velocity profile at cross-section x_8 is similar to that at the cross-section x_7. The 'Λ' shaped peak at the cross-section x_9 is almost vanished. The velocity profile between the wall and y/H $\approx$ 0.2 has '$\bigcap$' shape now as velocity gradually rises to $U/S_l \approx 20$ when moving towards the duct centre. The profiles along other three cross-sections maintain the downstream profiles but the velocity magnitude decreases slightly.

At t = 43 ms the collapse process has been completed and the flame front is close to the cross-section x_{10}. The cross-section x_7 velocity profile has two parts. The upper part between the wall and y/H $\approx$ 0.3 shows the previous time step pattern, with higher the velocity by about 10 units. The upper part, the middle section between y/H $\approx$ 0.3 and centre has a similar profile as at the last time step with a reduction in value by 10 units. The same can be said about the velocity profile along cross-section x_8. The velocity magnitude for the cross-section x_9 falls but the profile has a similar trend as t = 41.5 ms. The cross-section x_{10} losses its 'Λ' shaped peak close to the wall but the rest of the distribution is similar to the last time step. The values of velocity are higher slightly when compared to the previous time step. The velocity profiles cross-sections x_{11} and x_{12} have the same trend as the profile along cross-section x_{10}.

At t = 43.5 ms the flame moves forward with the same flame front shape (see Figure 6.23). Near the wall velocity drops along the cross-section x_7, however maintaining its profile from t = 43 ms. The velocity profile along cross-section x_8 follows the same trend as at the cross-section x_7. The velocity profile along cross-section x_9 increases rapidly at the wall up to $U/S_l \approx 8$ then becomes constant at y/H $\approx$ 0.4. Then it increases up to $U/S_l \approx 20$ at the duct centre. However, its values are lower in comparison to the t = 43 ms. The velocity profile along cross-section

x_{10} now has 'Λ' shape near the wall. The velocity rises sharply up to $U/S_l \approx 12$ at $y/H \approx 0.3$ and afterward it drops rapidly at $y/H \approx 0.2$. Then, the velocity increases by a small amount and it remains constant until duct centre ($U/S_l \approx 5$). The velocity profiles along cross-sections x_{11} and x_{12} form 'Λ' shape between the wall and the point $y/H \approx 0.4$. After this point, the velocity profiles are similar to the last time step, however its values lowered by about 10 units.

At t = 44 ms the flame front moves further forward (see Figure 6.24). For the velocity profile along cross-section x_7, the '⋂' shape from previous time step changes to 'Λ' shape and reaches the wall (between $y/H \approx 0.48 - 0.5$). Beyond this point, the velocity profile is similar to the previous time step when approaching the duct centre but it is higher by 5 units. For the cross-section x_8, the velocity close to the wall increases sharply from zero to $U/S_l \approx 3$ and then forms a similar pattern as at t = 43.5 ms with a higher value (about 5 units) for most of the points. The velocity profile along cross-section x_9 has a similar pattern as described at the cross-section x_8 in this time step. The velocity profile cross-section x_{10} keeps its 'Λ' shape near the wall with slightly higher values in comparison with the previous time step. The velocity then increases linearly until $y/H \approx 0.3$, with its magnitude dropping in this part compared to the t = 43.5 ms. After that it rises again sharply up to $U/S_l \approx 22$ at $y/H \approx 0.18$, and it stays constant until reaching the duct centre. The velocity profile along cross-section x_{11} is the same as to the last time step between $y/H \approx 0.3$-0.5 by about 5 units higher value. Then it rises gradually when approaching the duct centre. In this section, the velocity magnitude is decreased about 10 units in comparison to the last time step. The velocity profile along cross-section x_{12} has the same profile as the cross-section x_{11}. The velocity magnitude along cross-sections x_{11} and x_{12} are close at this time step.

At t = 46 ms the flame front is between the cross-sections x_{10} and x_{11}. The velocity profile along cross-section x_7 shows an extended 'Λ' shape between

y/H $\approx$ 0.3 and wall. Then it rises until duct centre up to U/S_l $\approx$ 15. The velocity values are lower for all the points. The velocity profile along cross-section x_8 has similar values as t = 44 ms between the wall and point y/H $\approx$ 0.45, then it drops gradually until U/S_l $\approx$ 3 at y/H $\approx$ 0.35. Afterward, the velocity increases gently to about U/S_l $\approx$ 12 at duct centre. The velocity is reduced from y/H $\approx$ 0.45 to duct centre compare to the previous time step. At the cross-section x_9 velocity profile forms '$\bigcap$' shape between the wall and y/H $\approx$ 0.3. Then the velocity increases to about U/S_l $\approx$ 10 when approaching the duct centre point. The magnitudes are reduced in comparison to the t = 44 ms. The velocity profile along cross-section x_{10} forms 'Λ' shape between the wall and duct centre, with the peak velocity value located in the middle of the cross-section (U/S_l $\approx$ 15). The velocity magnitude near the wall is reduced in comparison with the previous time step. The velocity profile along cross-section x_{11} keeps its shape near the wall from prior time step. However, it increases somewhat when approaching the duct centre assuming a constant value between y/H $\approx$ 0 – 0.2 (U/S_l $\approx$ 34). Generally, most of the points have higher velocity value compared to t = 44 ms. The velocity profile along cross-section x_{12} has similar velocity magnitudes and pattern as the cross-section x_{11} in this time step.

The flame elongates substantially between t = 46 - 48.5 ms and assumes a finger shape. At t = 48.5 ms the flame front begins to form a finger shape with an extended skirt. The flame front is approaching the cross-section x_{12}. The velocity profile along cross-section x_7, which is now behind the flame front starts returning to the initial downstream profile. The velocity values increase slightly near the wall (up to U/S_l $\approx$ 13) and then drop to about U/S_l $\approx$ 1 at y/H $\approx$ 0.2. They are greater than at the previous time step. Next, the velocity rises gradually to about U/S_l $\approx$ 3 at the duct centre. In this part, velocity has lower magnitude compared to the previous time step. The velocity profile along cross-section x_8 follows similar trends as the

cross-section x_7. The velocity profile along cross-section x_9 forms 'Λ' shape between the wall and point y/H ≈ 0.1. Afterward, the velocity assumes its constant value of $U/S_l \approx 0.5$ until the duct centre. The velocity profile and its value are similar to the cross-sections (x_7 and x_8). The velocity along cross-section x_{10} rises gradually from the wall to the duct centre. At most points, the velocity is higher than for the prior time step. The velocity profile along cross-section x_{11} at this time step is similar to t = 46 ms. The velocity profile along cross-section x_{12} also follows its pattern at last time step but it has higher magnitude about 20 units except near the wall.

At t = 49.5 ms the finger flame front shape formation is completed and the flame front has passed through cross-section x_{12}. The velocity profile along all cross-section follows the same trends as at the previous time step near the wall. However, after a short period of constant velocity, it rises gradually as approaching the duct centre ($U/S_l \approx 24$) with a convex shape. The velocity profile along cross-section x_8 has similar trends and values as at the cross-section x_7. The velocity magnitude rises in comparison with the previous time step. The velocity profile along cross-section x_9 starts forming the initial downstream pattern. Although there is still a slight 'U' shape near point y/H ≈ 0.3. The velocity at all points is higher in comparison to t = 48.5 ms. The velocity profile along cross-section x_{10} increases gently from the wall to the cross-section middle point, and then it almost stays constant until reaching the duct centre ($U/S_l \approx 15$). The velocity in all points of the cross-section x_{11} is reduced compared to the previous time step. The velocity profile is now similar to the initial downstream profile. The velocity profile along cross-section x_{12} has higher velocity magnitude compare to the other cross-sections as it is closer to the flame front. It also retains its pattern from the previous time step while the velocity values raise about 10 units in most of the points.

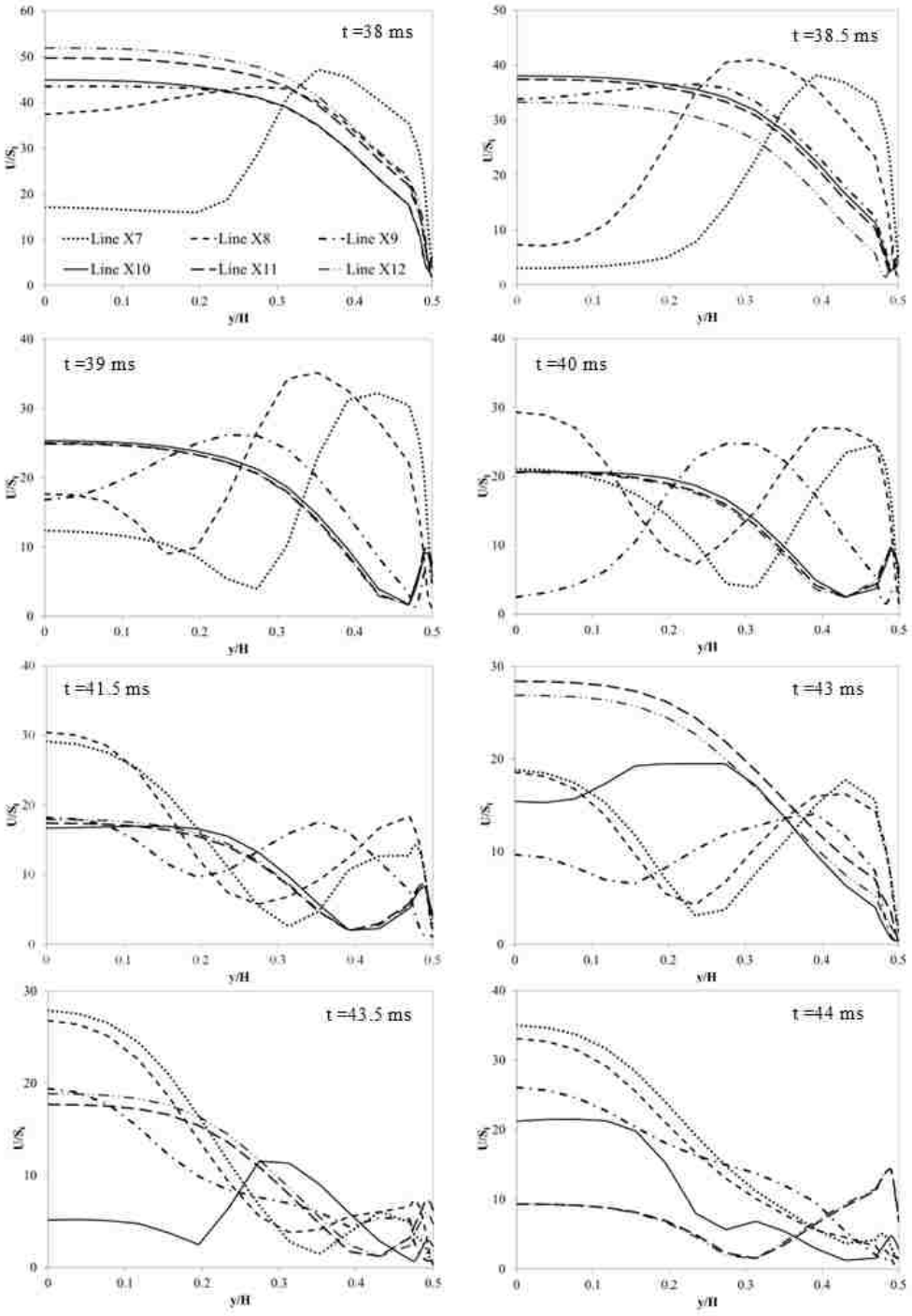

Figure 6.25: Normalized velocity distribution during the first inversion for x_7-x_{12} cross-sections (Part A).

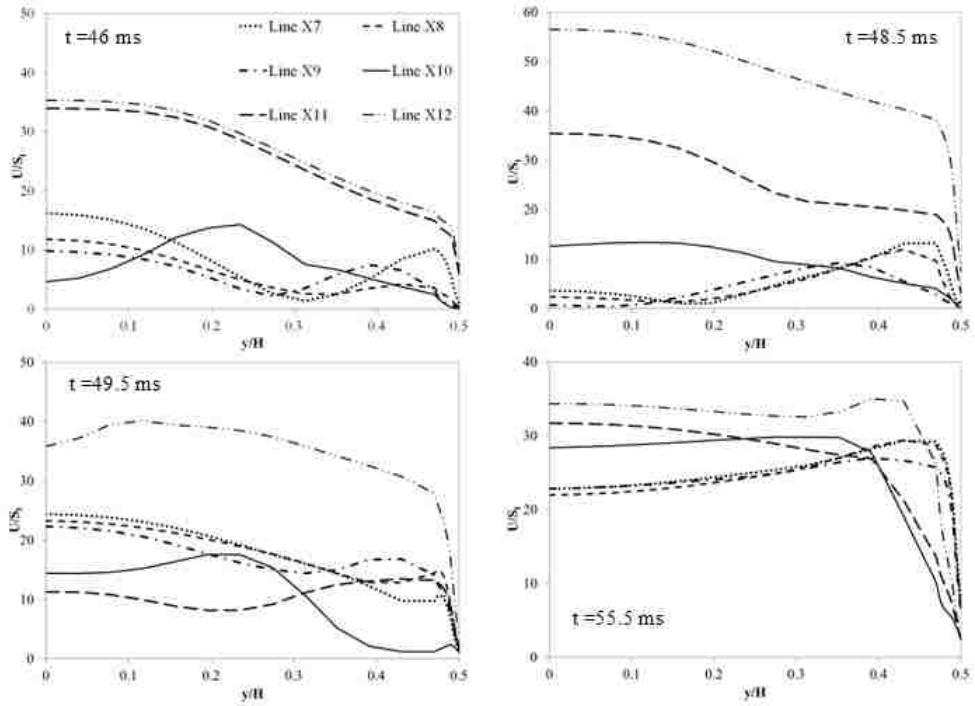

Figure 6.26: Normalized velocity distribution during the first inversion for x_7-x_{12} cross-sections (Part B).

At t = 55.5 ms the flame front is far in front of the cross-section x_{12}, all the velocity profiles along cross-sections x_7-x_{12} almost return to somehow the 'initial downstream' pattern. At this point, the flame skirt reduces considerably as most parts of the flame skirt touch the wall. The flame front maintains its finger shape.

Figures 6.27, 6.28 and 6.29 show the normalized velocity distributions and fuel mass fractions along the duct during the first inversion flame formation for y/H = 0, y = 0.45 and y/H = 0.49 longitudinal cross-sections for times from 38 ms to 49.5 ms. These three longitudinal cross-sections are picked in a way to demonstrate the flame speed at the duct centre line and close to the duct wall. The cross-section y/H = 0.49 shows the flame near the wall by excluding the wall boundary/initial conditions effects, however, the cross-section y/H = 0.45 illustrates the flame speed outside the mesh prism layers.

At t = 38 ms while the flame front is at x/L $\approx$ 0.4, the velocity profiles for the

cross-sections y/H = 0.45 and y/H = 0.49 are the similar in combustion products. Besides the low maximum '$\bigcap$' shape between x/L $\approx$ 0 – 0.2, the velocity profile generally increases when approaching the flame front. There is a rapid rise of velocity (approximately 20 units) at the flame front. That rise is followed by an equally rapid drop for y/H = 0.45 and y/H = 0.49. Only at the y/H = 0 the velocity keeps on increasing in the unburnt mixture.

At t = 38.5 ms the flame is still in about same location (x/L $\approx$ 0.4). On the product side of the flame front, all three velocity profiles have analogous trends. The '$\bigcap$' shape from previous time step is extended from the spark point to x/L $\approx$ 0.3. The velocity at the centre-line (y/H = 0) reduces to zero on the burnt side. Then it rapidly rises to about U/S_l $\approx$ 40 and it almost stays at this level in the fresh mixture for the remainder of the duct. For the cross-sections y/H = 0.45 and y/H = 0.49, the velocity profiles are somewhat different. The velocity reduces to zero at x/L $\approx$ 0.31 and then it increases to U/S_l $\approx$ 30 close to the flame front in the products region and then drops at the flame. In the fresh mixture, the velocities are much lower than those at the centre-line (y/H = 0).

At t = 39 ms the split starts growing in the flame front centre. The flame is almost in the same position as last time step. At the cross-section y/H = 0, peak velocity at the flame location is reduced in comparison to previous time steps (U/S_l $\approx$ 25). However, the profile trend is similar to that in the previous time step. For the cross-sections y/H = 0.45 and y/H = 0.49, the profiles are the same as the cross-section y/H = 0 in the products area. The peak velocity for both cross-sections at the flame location decreases when compared with t = 38.5 ms. In contrast to the centre-line, the other two velocity profiles are much lower on the fresh gas side.

At t= 40 ms, the flame split grows through the flame centre, but there is little change in flame front location. At the cross-section y/H = 0, velocity increases gradually from the ignition site to U/S_l $\approx$ 15 at x/L $\approx$ 0.2. Then it assumes 'Λ'

shape between x/L $\approx$ 0.2 – 0.4. The velocity peak for 'Λ' shape is U/S_l $\approx$ 30 and it is followed by a drop to U/S_l $\approx$ 20. In contrast to previous time steps, it is the first time that the velocity on the centre-line drops and rises at flame front. And this behavior will be repeated in the next few time steps (until t = 48.5 ms) when the flame moves quickly forward. Just before the flame front location, the velocity rises again to about U/S_l $\approx$ 30. At the flame location, there is a sharp reduction to U/S_l $\approx$ 5 and it increases to U/S_l $\approx$ 20. The velocity profiles for cross-sections y/H = 0.45 and y/H = 0.49 are approximately the same, with the difference that the velocities for the y/H = 0.49 have lower magnitudes at most of the locations. The velocity pattern develops gradually from the spark point until x/L = 0.2.

At t = 41.5 ms the flame lips collapsing process is initiated and the flame front moves forward. The cross-section y/H = 0 profile is similar to that at t = 40 ms with a lower magnitude of velocity on the burnt gas side. At the flame front, the velocity first increases to about U/S_l $\approx$ 33 and then it reduces to about U/S_l $\approx$ 5, and then increases again to its value from the product side. The velocity profile along cross-section y/H = 0.45 maintains its pattern from the last time step with lower velocity up to the point x/L $\approx$ 0.2. Thereafter, it fluctuates up to x/L$\approx$0.7. The velocity profile along cross-section y/H = 0.49 has a similar trend as the cross-section y/H = 0.45 with lower velocity magnitudes. The peak velocities for all three cross-sections at the flame location are lower compared to t = 40 ms.

At t = 43 ms the flame lips merging is completed and there is a remarkable change in the velocity profile along the y/H = 0 cross-section. All velocities in the products are lower and velocities in the unburnt mixture are higher (particularly close to the flame front). Even more interestingly, the y/H = 0 velocity profile in the next time step t = 43.5 ms returns to its pattern from t = 41.5 ms time step (higher velocities in the product and lower velocities in the reactants at the flame front vicinity. The velocity profile along cross-section y/H = 0 retains its profile from the last time

step with a lower magnitude in the fresh gas area. There is a sharp rise in the velocity profile close to the flame (up to $U/S_l \approx 20$). The velocity then experiences a rapid reduction to almost zero and eventual sharp increase up to $U/S_l \approx 30$ in the fresh mixture area. The velocity profiles along cross-sections y/H = 0.45 and y/H = 0.49 retain their pattern from the last time step except for locations far away from the flame front in the fresh mixture.

At t = 43.5 ms the flame assumes a flat shape at the front and moves ahead slightly. Along the centre-line (y/H = 0) the velocity profile is remarkably similar to t = 41.5 ms (two-time steps back). The velocity profile along cross-section y/H = 0 increases gradually before the flame front up to $U/S_l \approx 28$ at x/L $\approx$ 0.41. At the flame front, the velocity falls to almost zero before returning to $U/S_l \approx 18$. For the both y/H = 0.45 and y/H = 0.49 cross-sections, the velocity fluctuates all along the duct length with lower velocity magnitudes.

At t = 44 ms the flame moves forward while retaining its shape. The cross-section y/H = 0 velocity profile is similar to the profile at t = 43.5 ms with higher velocity values in the products and almost the same in the fresh mixture. Both of the velocity profiles at cross-sections y/H = 0.45 and y/H = 0.49 have an approximately the same pattern as at previous time step on the product side, with somewhat higher velocities.

At t = 46 ms the flame advances while the size of flame skirt increases. The velocity profiles for all three cross-sections are similar to t = 38 ms. They are lower on the product side of the flame, and much higher on the fresh mixture side. The velocity increases gradually until $U/S_l \approx 10$ at x/L $\approx$ 0.1. Then it reaches a nearly constant value before the flame front in products area. Afterward, the velocity rises to $U/S_l \approx 16$ until a sudden reduction to $U/S_l \approx 2$ at the flame front. Then, the velocity increases to about $U/S_l \approx 35$. In the fresh mixture, the velocity oscillates while its magnitude is changing between $U/S_l \approx 30 - 40$ as approaching the duct end. Along the y/H = 0.45 and y/H = 0.49 cross-sections, velocity fluctuates

on both sides of the flame front, however with the more regular pattern on the fresh mixture side.

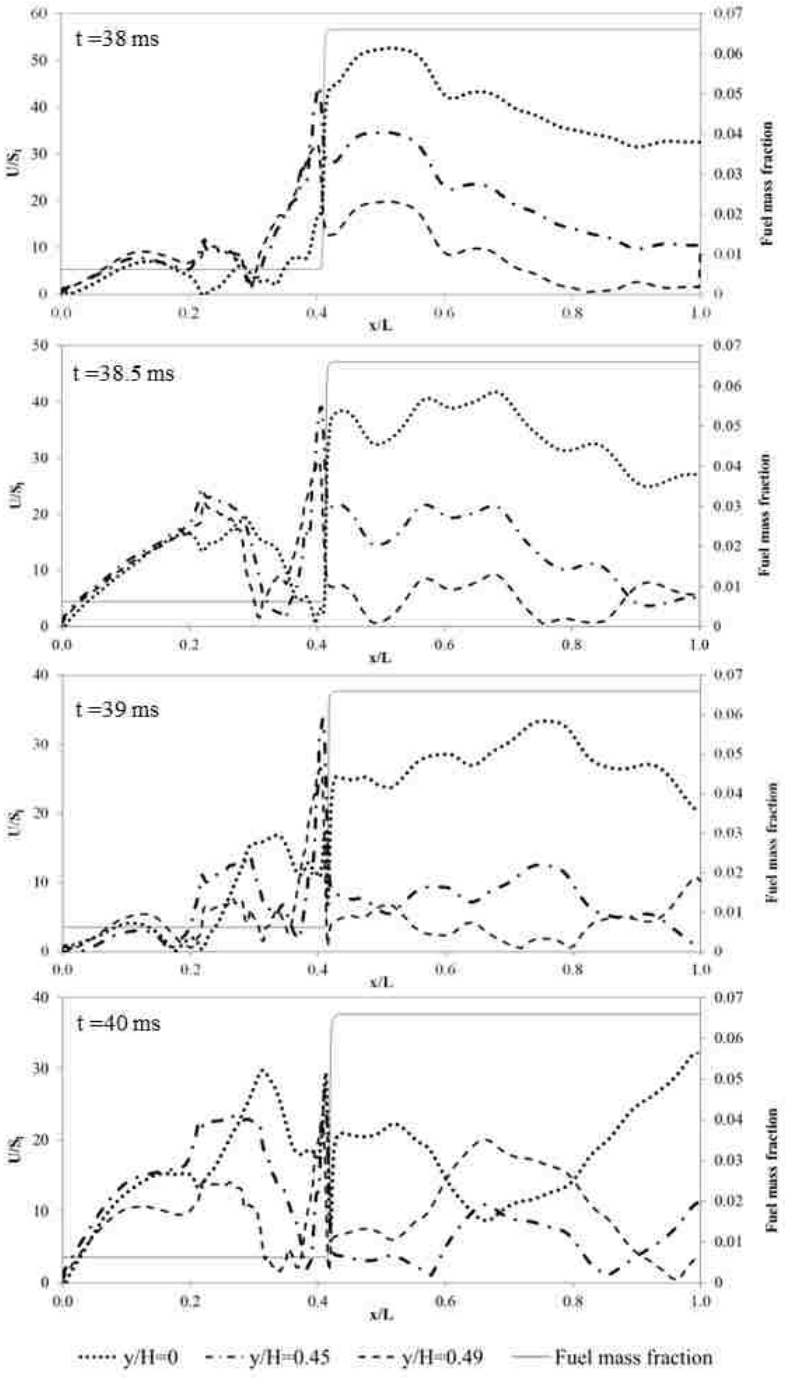

Figure 6.27: Normalized velocity distribution and fuel mass fraction along the duct length at different times during the flame first inversion formation for y/H = 0, y = 0.45 and y/H = 0.49 cross-sections (Part A).

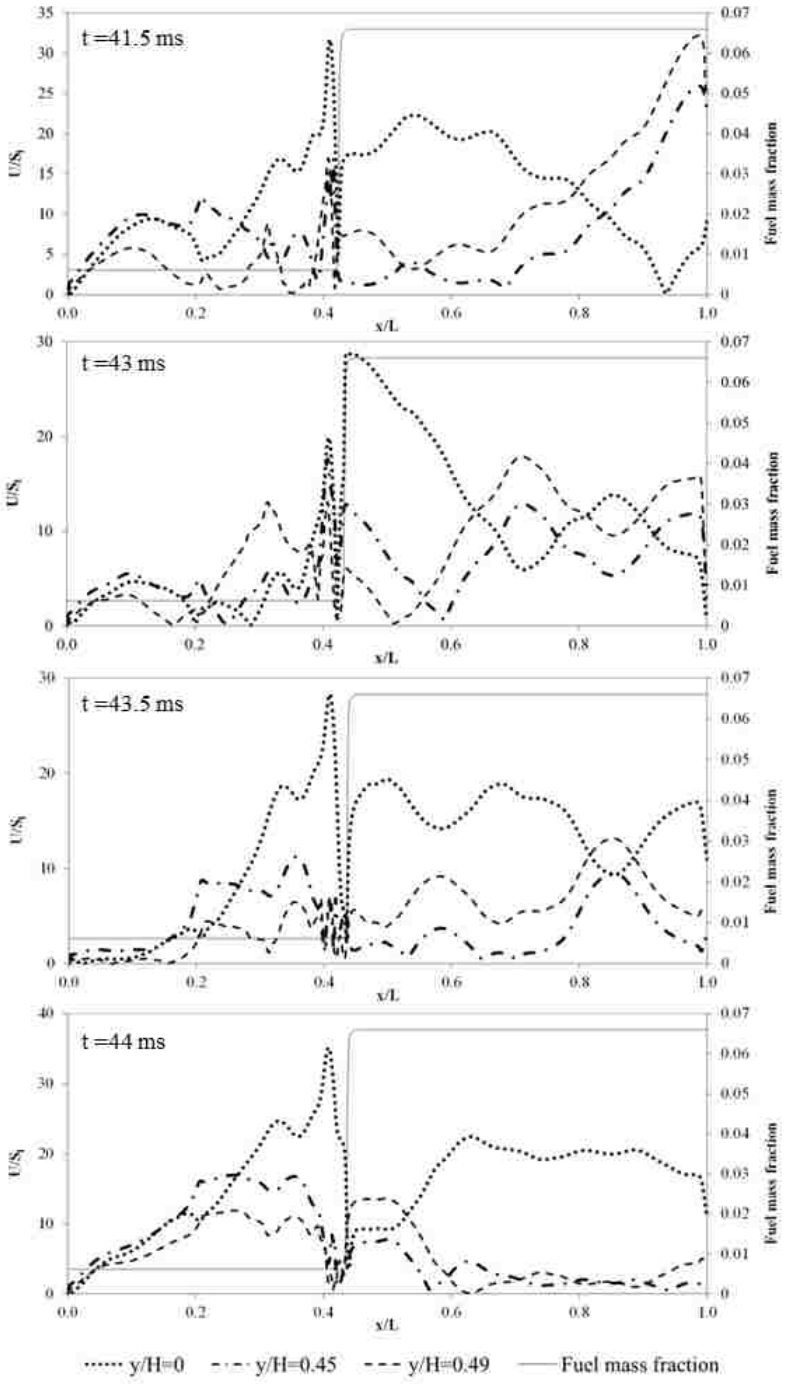

Figure 6.28: Normalized velocity distribution and fuel mass fraction along the duct length at different times during the flame first inversion formation for y/H = 0, y = 0.45 and y/H = 0.49 cross-sections (Part B).

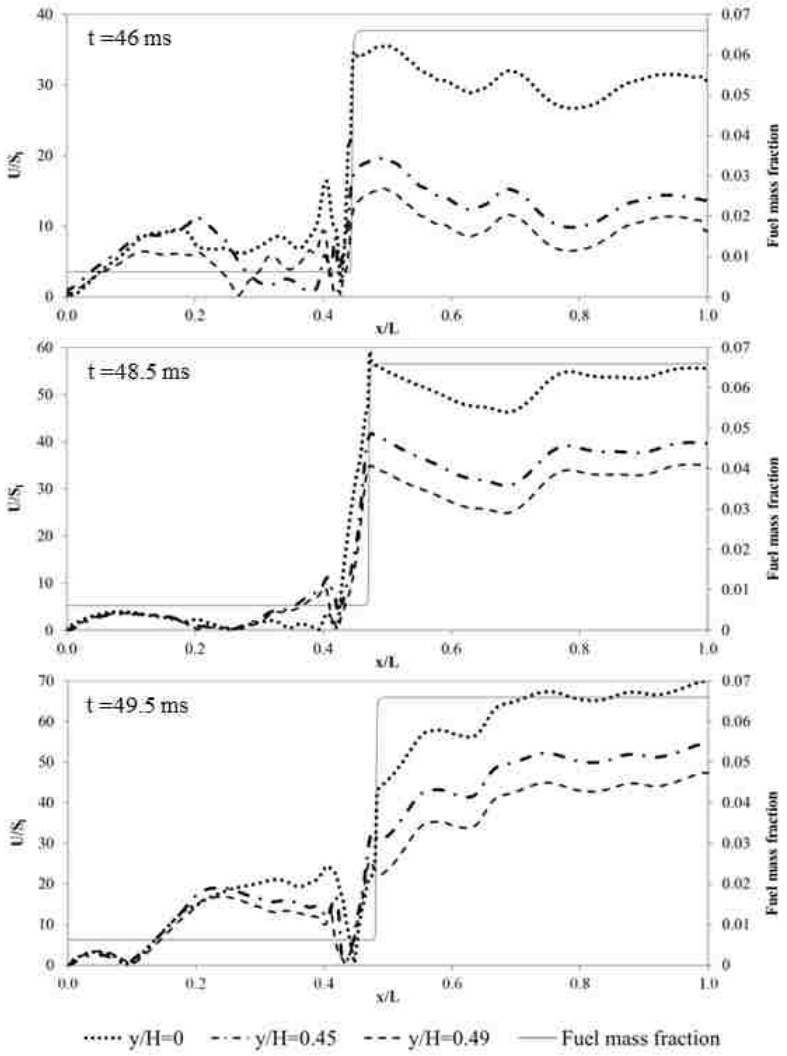

Figure 6.29: Normalized velocity distribution and fuel mass fraction along the duct length at different times during the flame first inversion formation for y/H = 0, y = 0.45 and y/H = 0.49 cross-sections (Part C).

At t = 48.5 ms, the flame front moves close to the x/L $\approx$ 0.5 cross-section and the flame forms finger shape. All three velocity profiles look almost like a step-change pattern. Very low in the products, quickly increasing shortly before the flame and staying on that level in the fresh mixture.

At t = 49.5 ms the flame has propagated half length of the duct and the finger shaped flame is formed completely. All three velocity profiles are similar at most locations. The velocities in the fresh gas are much higher than these in combustion

products.

Figure 6.30 illustrates the velocity line integral convolution at the flame first inversion zone. Qualitative similarities exist between this case and that of tulip flame formation (Figure 6.9). This is especially for time steps from t = 38 ms to t = 41.5 ms in Figure 6.30, and time steps t = 15 ms to 21 ms in Figure 6.9. Larger differences exist after t = 43 ms for which more complex flame front surface can be seen (Figure 6.31).

At t = 38 ms the flame skirt touches the wall. In the subsequent time frames t = 38.5 ms and t = 39 ms, a series of vortices form along the flame surface can be observed. These vortices at t = 40 ms are developed and enlarged enough to couple with the vortices which have been formed ahead of flame in the fresh mixture since t = 39 ms to initiate the dent at the flame front centre.

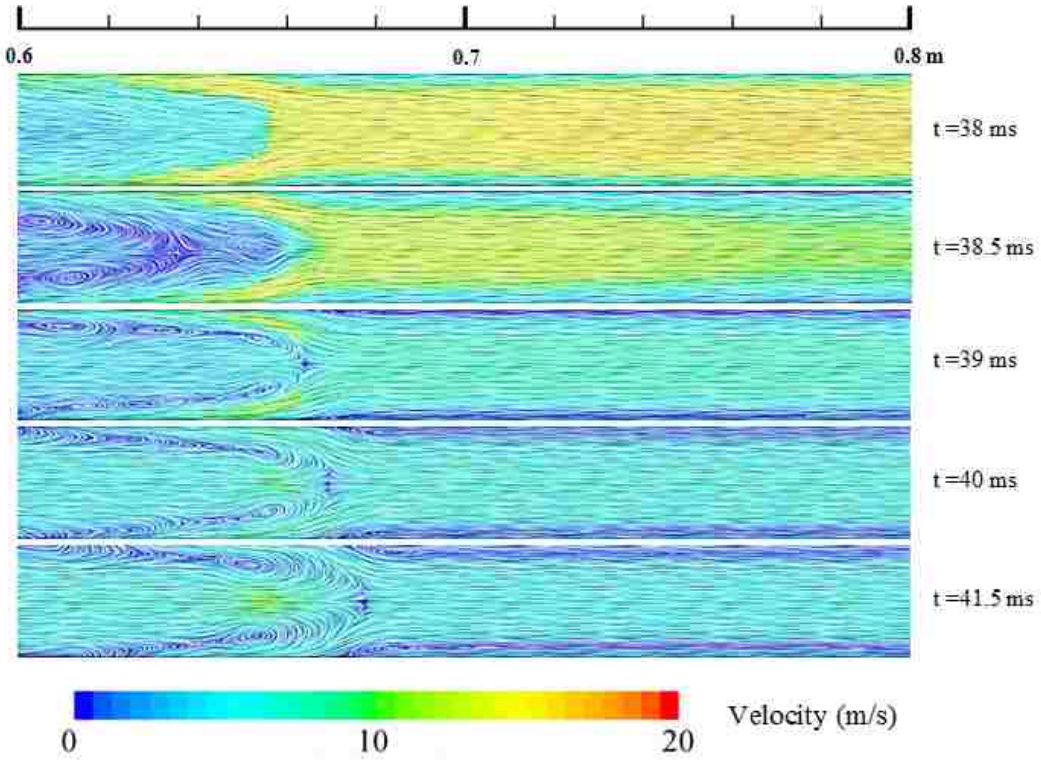

Figure 6.30: Velocity line integral convolution at the first inversion zone (Part A).

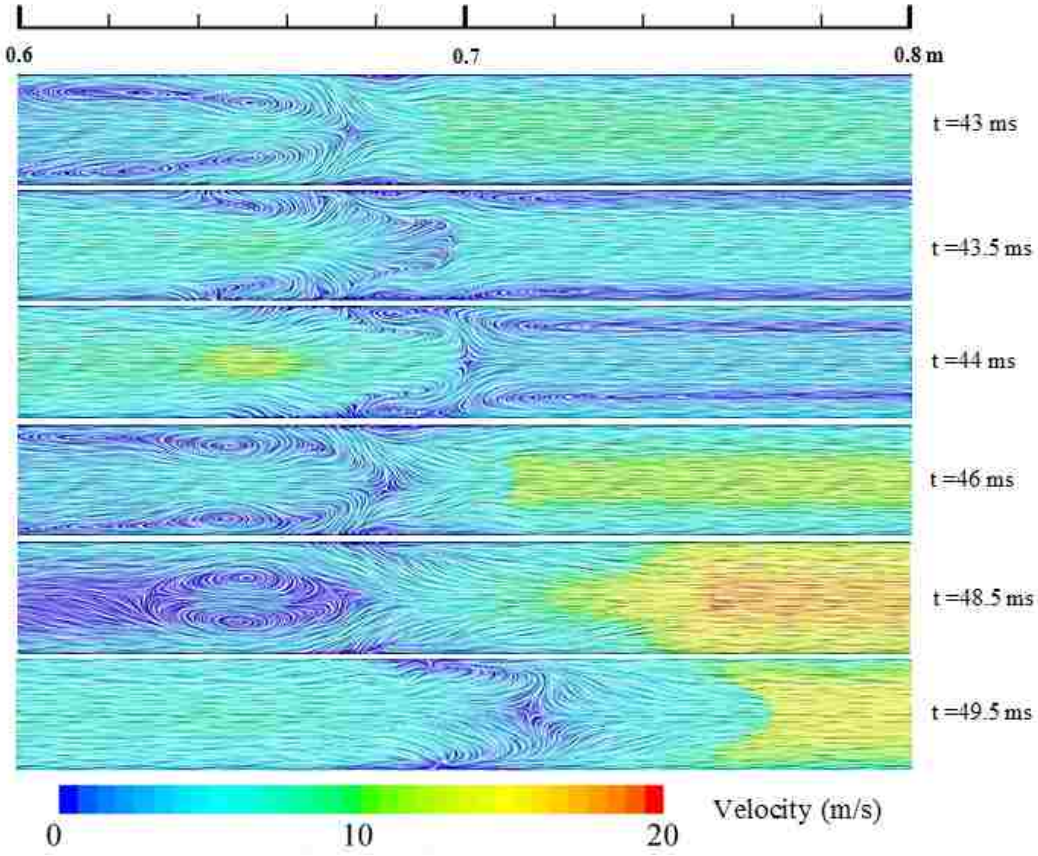

Figure 6.31: Velocity line integral convolution at the first inversion zone (Part B).

At t = 40 ms, the vortices ahead of the flame in the fresh mixture (near the duct top and bottom walls) become larger and consequently make the split deeper. These eddies at the front and behind the flame contour are larger in comparison to those that formed during the tulip flame creation (see Figure 6.32).

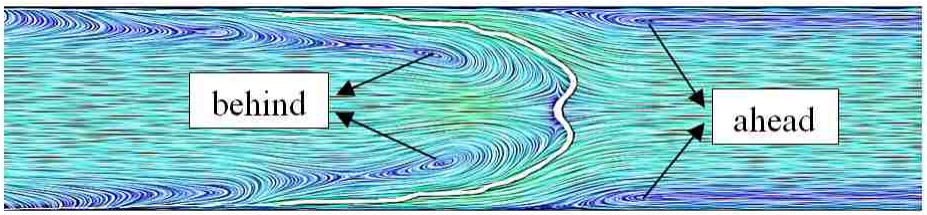

Figure 6.32: Flame surface (marked by the fuel mass fraction margin between 0 and 0.06) and velocity line integral convolution at t = 40 ms.

At t = 41.5 ms, the vortices in front of the flame are still growing. Behind the

flame in product side, the cores of vortices are leaving the flame front (Figure 6.33).

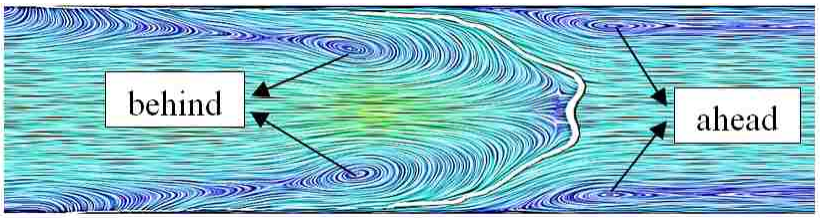

Figure 6.33: Flame surface (marked by the fuel mass fraction margin between 0 and 0.06) and velocity line integral convolution at t = 41.5 ms.

At t = 43 ms (see Figures 6.31 and 6.34), the flame front vortices become weaker and the vortices behind the flame push the flame forward. This is the first main difference between the tulip and the first flame inversion. In contrast to the tulip flame, the vortices ahead of flame develop again at t = 43.5 ms (Figure 6.35). This causes the flame front to detach more from the wall, making the flame front much narrower.

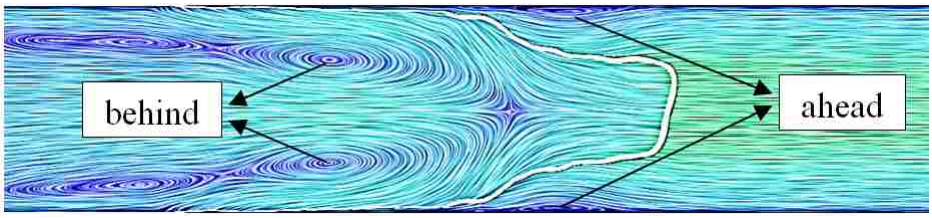

Figure 6.34: Flame surface (marked by the fuel mass fraction margin between 0 and 0.06) and velocity line integral convolution at t = 43 ms.

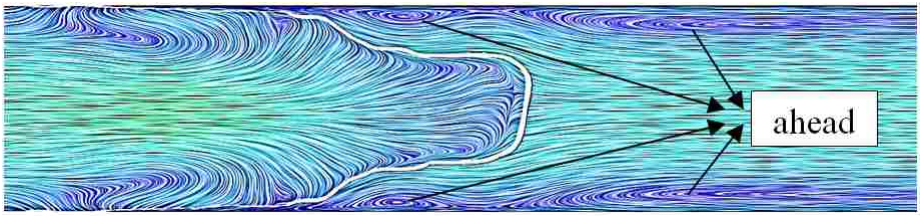

Figure 6.35: Flame surface (marked by the fuel mass fraction margin between 0 and 0.06) and velocity line integral convolution at t = 43.5 ms.

At t = 46 ms, the eddies in front of the flame vanish and backside eddies push the flame forward again (Figure 6.36).

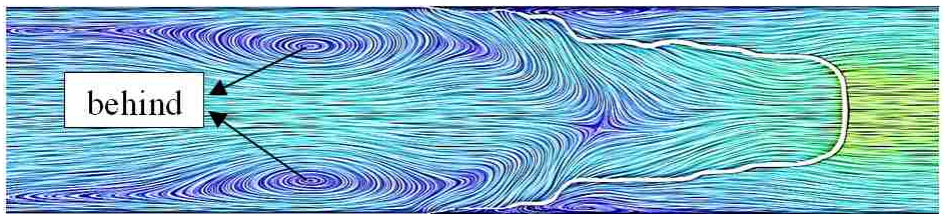

Figure 6.36: Flame surface (marked by the fuel mass fraction margin between 0 and 0.06) and velocity line integral convolution at t = 46 ms.

At t = 48.5 ms, the back side vortices from t = 46 ms move inverted, where to end another (see Figure 6.37). However, they are now well behind the flame front which reduces their effect on the flame front. They completely disappear at t = 49.5 ms. Now the flame has entered a similar state to that at the end of tulip flame sequence. This point can be considered as the final stage of first inversion flame evolution.

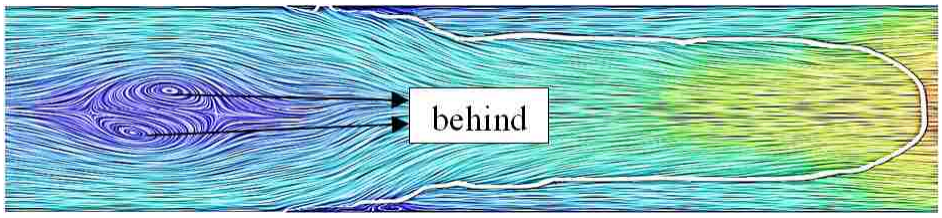

Figure 6.37: Flame surface (marked by the fuel mass fraction margin between 0 and 0.06) and velocity line integral convolution at t = 48.5 ms.

6.5.2 Pressure distribution at first flame inversion zone

Figure 5.34 shows the normalized absolute total pressure (P_{ATP}) distribution and fuel mass fraction at different times during the first inversion formation for y/H=0 cross-section (centre-line). P_0 is the initial pressure. Similarly to the tulip flame zone (see Figure 5.17), the data have the same range of pressure ratio. Also, the general trends for times on t = 38 ms to t = 43 ms of the pressure changes during the first inversion flame are following those for the tulip flame formation.

At t = 38 ms, while the flame front changes from the finger shape to flat flame, the pressure increases gradually in front of the flame front. At the flame front, there

is a step-like pressure rise. After that, the pressure keeps growing with oscillations until the duct end.

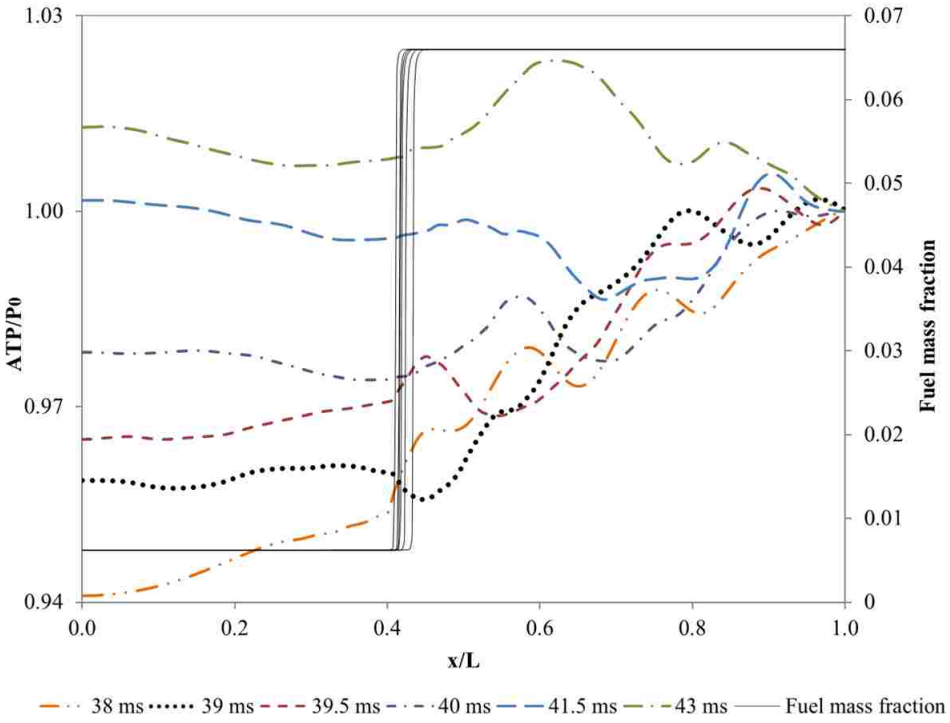

Figure 6.38: Normalized absolute total pressure (P_{ATP}) distribution and fuel mass fraction at different times during the first inversion formation for y/H=0 cross-section (centre-line). P_0 is the initial pressure.

At t = 39 ms and as the dent is created at the flame front centre, pressure has almost a constant value in combustion products. There is a pressure drop across the flame front and then the pressure keeps increasing with oscillations are seen in the last time step.

At t = 39.5 ms the pressure gradually rises on the products side. There is a small pressure increase at the flame front and the similar trend from the previous time steps is followed.

At t = 40 ms, the flame split has reached its maximum size. Likewise, a lower pressure before the flame front can be seen. Then the pressure rises gradually and proceeds to the duct end with oscillations.

At t = 41.5 ms, the lips of flame begin to collapse. The pressure is almost constant in the products, changes slightly across the flame and in the fresh mixture area.

At t = 43 ms the merging process is completed. The similar pattern as the last time step can be seen until x/L $\approx$ 0.5. Then, rising pressure to a local maximum followed by oscillations.

6.6 Comparison with analytical and experimental results

Table 6.1 reports on the location and time of the three different steps in the flame development stages; 1) spherical shape, 2) flame-wall touch, and 3) tulip formation starting point from the numerical simulation (laminar combustion model), the experiment, and the analytical approaches (by Clanet [14] and Bychkov [12]). The X_{sph} for all the methods except numerical approach is the same. As mentioned earlier, there is no spark model (growth of kernel flame) in Star CCM+. Therefore, the numerical values for time and location of the spherical stage are not shown. Regarding the t_{sph}, both analytical models are estimated lower values in comparison to the experiment.

The flame skirt contacts the wall at about 22 cm from the spark point in the experiment (X_{wall}). The numerical model underestimates this point by about 13%. The Clanet & Searby equation is off by about 27% while the Bychkov model has more than 50% error. The corresponding time for the flame-wall touch in the experiment is about 15 ms (t_{wall}). The numerical result and the Clanet model are far about 33%. The obtain time from the Bychkov equation has more than 50% error. One should remember is the difficulties in extracting the right moment of the flame-wall touch in the experiment. This is generally due to the challenges in identifying the flame front from the recorded movie frames.

Regarding the tulip flame location (X_{tulip}), the Bychkov model calculates the closer value (45.9 cm) to the experimental data (43 cm). The numerical tulip flame happens in a shorter distance from the spark point in comparison with the all other

approaches. The Clanet & Searby model estimation is about 16% higher (50.1 cm). The tulip flame forms at 28 ms in the experiment (t_{tulip}). The numerical flame occurs in a quicker time (16 ms) in compares to the experimental flame. The tulip flame formation times base on the analytical approaches are much closer to the numerical results rather than the experimental data. The numerical flame is faster than the experimental data. The adiabatic boundary condition in the numerical simulation should be considered as one of the main reasons for this discrepancy.

Table 6.1: Flame characteristics; times and locations in the experiment, numerical simulation (laminar combustion model) and analytical models when Φ=1.1.

	X_{sph} (cm)	t_{sph} (ms)	X_{wall} (cm)	t_{wall} (ms)	X_{tulip} (cm)	t_{tulip} (ms)
Experimental	0.625	5.6	22	15	43	28
Numerical (Laminar model)	-	-	19	9.5	31.5	16
Analytical (Bychkov)	0.625	2.6	10	7	45.9	9.6
Analytical (Clanet & Searby)	0.625	3.9	16.2	10.16	50.1	12.9

Chapter 7

7 Results for fully opened end: XiDymFoam model

In this chapter, the results obtained from the XiDymFoam combustion model for the opened end case are presented. The results from XiDymFoam model for both RANS and LES methods versus the experimental data are compared.

7.1 XiFoam-RANS results versus experimental data

The methods to compute Xi and S_l, are outlined in Table 7.1 for the semi-2D calculations:

Table 7.1: Simulation matrix for the XiDymFoam model (semi-2D, RANS, Φ=1.1).

Case	Xi model	S_l model
I	Algebraic	Unstrained
II		Equilibrium
III		Transport
IV	Transport	Unstrained
V		Equilibrium
VI		Transport

Figure 7.1 shows results in terms of flame front location from the spark versus time for the cases I, II and III of Table (7.1). Results are the same for all three cases before the first inversion location. The dynamic of numerical and experimental profiles are very much the same. There is a stagnation in the flame movements in both numeric and experiment when the tulip flame develops. In simulation the flame is at x ≈0.35 m from t = 13 ms to t = 25 ms, in experiment the flame is at x ≈ 0.40 m from t = 30 ms to t = 35 ms in the tulip flame area. In simulation the flame stays at x ≈ 0.6 m from t = 32 ms to t = 38 ms, in experiment it stays (even moves backward) at x ≈ 1 m for t = 55 ms to t = 60 ms for the inversion area development.

In between these locations, the flame accelerates in both experiment and numerical simulation. Generally, all three cases (I, II and III) overestimate the experimental results. The correlation coefficient (CC) values after the tulip for all cases are higher compared to before tulip formation (see Table 7.2). Also, the positions of the tulip flame and the 1st inversion are closer and occur earlier to the spark point compared to the experimental data.

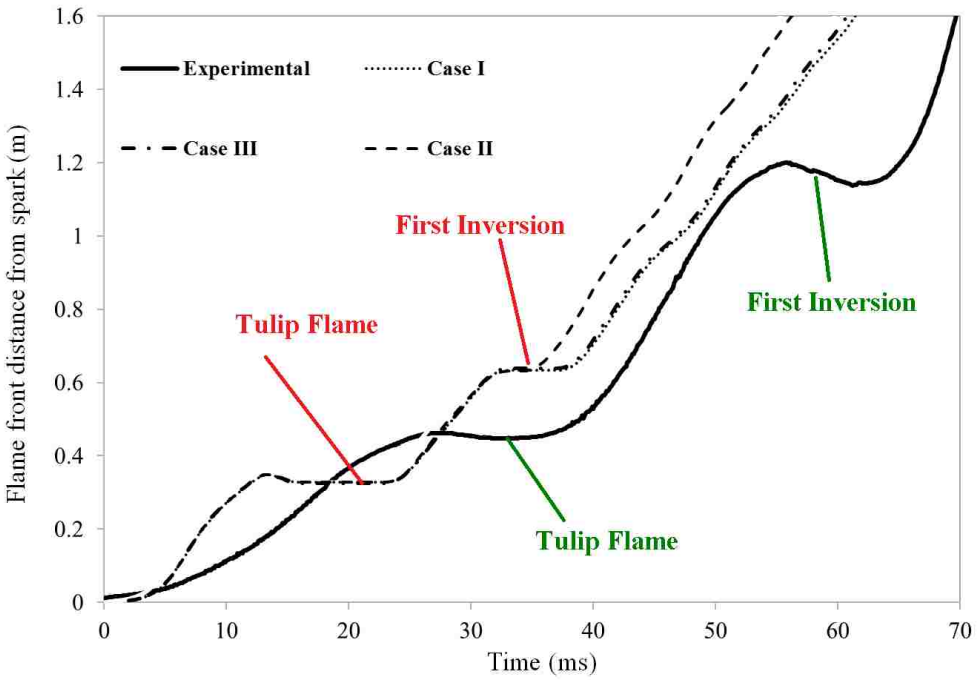

Figure 7.1: Experimental data versus numerical results employing XiDymFoam and algebraic Xi model while for all cases: Φ =1.1, k =1.5 m^2/s^2, ε =0.1 m^2/s^3 and Xi*ShapeCoef* = 0.25.

Figure 7.2 show the cases IV, V and VI of the Table (7.1). The similar trends for all three cases at the tulip flame formation point. Also, the dynamic profile of cases IV and V, and the experiment are similar. There is a stagnation in the flame movements in both numeric and experiment when the tulip flame develops. The time and locations of these stagnation points are the same as the cases I, II and III. The case VI (transport Xi model & transport S_l model) captures the flame first inversion better than the other two cases. There is a longer duration time of the

tulip formation/collapse compare to the algebraic cases (I, II and III). All three cases overestimate the experimental result. The correlation coefficient (CC) for these three cases are showed in Table 7.3.

Table 7.2: The correlation coefficient (CC) values for the cases I, II and III.

Case	I	II	III
CC value before tulip flame < 30 ms	0.849	0.849	0.849
CC value after tulip flame > 30 ms	0.967	0.971	0.963

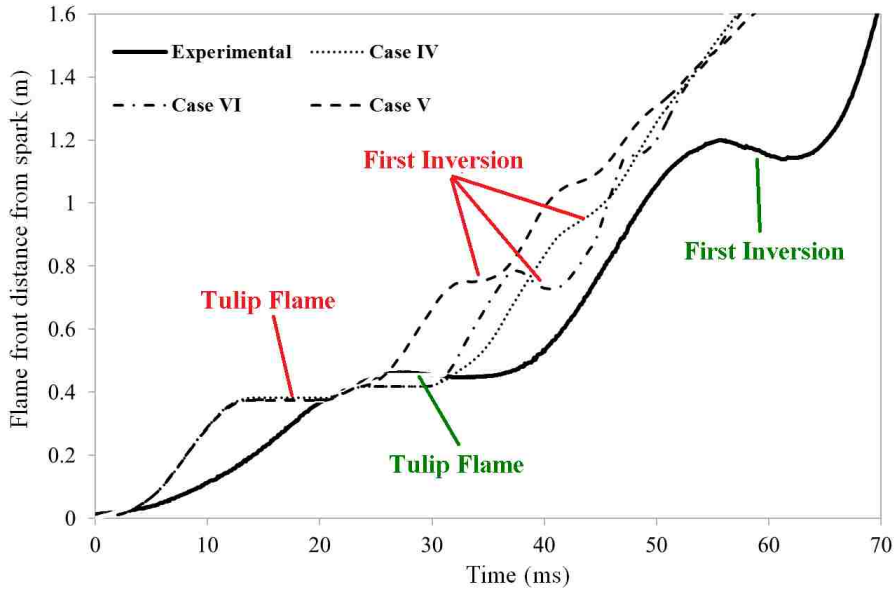

Figure 7.2: Experimental data versus numerical results employing XiDymFoam and transport Xi model while for all cases: Φ =1.1, k =1.5 m^2/s^2, ε =0.1 m^2/s^3 and Xi*ShapeCoef* = 1.

Table 7.3: The correlation coefficient (CC) values for the cases IV, V and VI.

Case	IV	V	VI
CC value before tulip flame < 30 ms	0.834	0.885	0.839
CC value after tulip flame > 30 ms	0.958	0.966	0.943

7.2 XiFoam-LES results versus experimental data

Figure 7.3 plots the flame position along the duct centre-line versus the flame propagation time for the experimental and numerical results. Results for both, the XiDymFoam-semi-2D and the XiDymFoam-2D models are plotted. Both models qualitatively could simulate the experiment well. Particularly where the attached images of the flame front surface of tulip flame and flame first inversion are concerned.

Qualitatively (flame front shape development), the 2D case and experiment are almost identical before the tulip flame formation. Qualitatively, the semi-2D case underestimates somewhat (at t = 10 ms, $\triangle x$= 0.08 m) the experiment in this region (speed wise). However, the flat flame front and the tulip flame occur much sooner in both 2D and semi-2D cases ($\approx$ 5 ms) in comparison with the experimental data ($\approx$ 15ms). In the downstream region, the flames in the numerical models travel faster and overestimate (speed wise) the experiment. The wrinkling of flame surface and the first flame inversion occur at a shorter location, but the same time in the simulation.

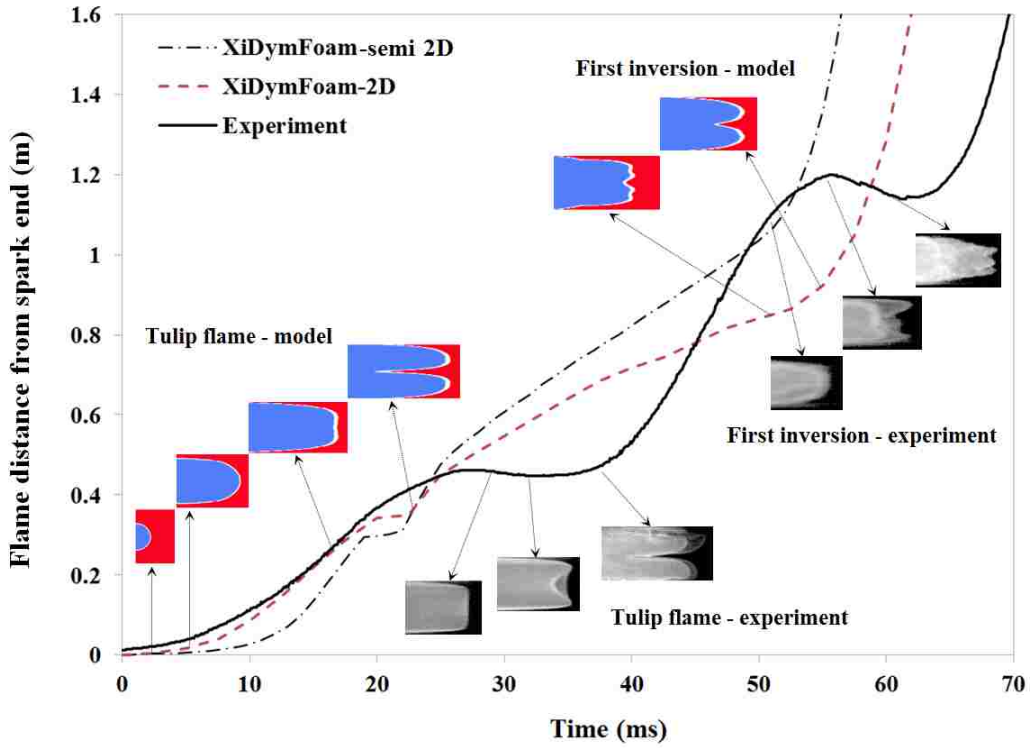

Figure 7.3: Comparison between XiDymFoam (LES cases) and experimental results for the premixed propane-air flame (Φ= 1.1); the flame position (at duct centre-line and referencing to the spark point) versus the flame propagation time. The flame surface shape at the tulip location and the flame first inversion region for both experimental and numerical (through progress variable scalar) methods are also illustrated.

The absolute flame speed versus the flame position at duct centre-line around the tulip formation region is illustrated in Figure 7.4. During the flame acceleration period (up to x = 0.25 m), the 2D case reproduces the flame propagation speed more accurately, and the speed values are close to the experimental data. The flame deceleration starts sooner in the simulation and the tulip forms at the shorter location ($x \approx 0.3$ m). Also, both of the numerical models did not predict the backward movement of the flame seen in the experiment at $x \approx 0.45$ m. The flame first inversion happens for both numerical models right after the tulip flame collapsing with higher speed in comparison to the experimental flame. Both 2D and semi-2D models underestimate the flame speed after $x \approx 0.5$ m considerably.

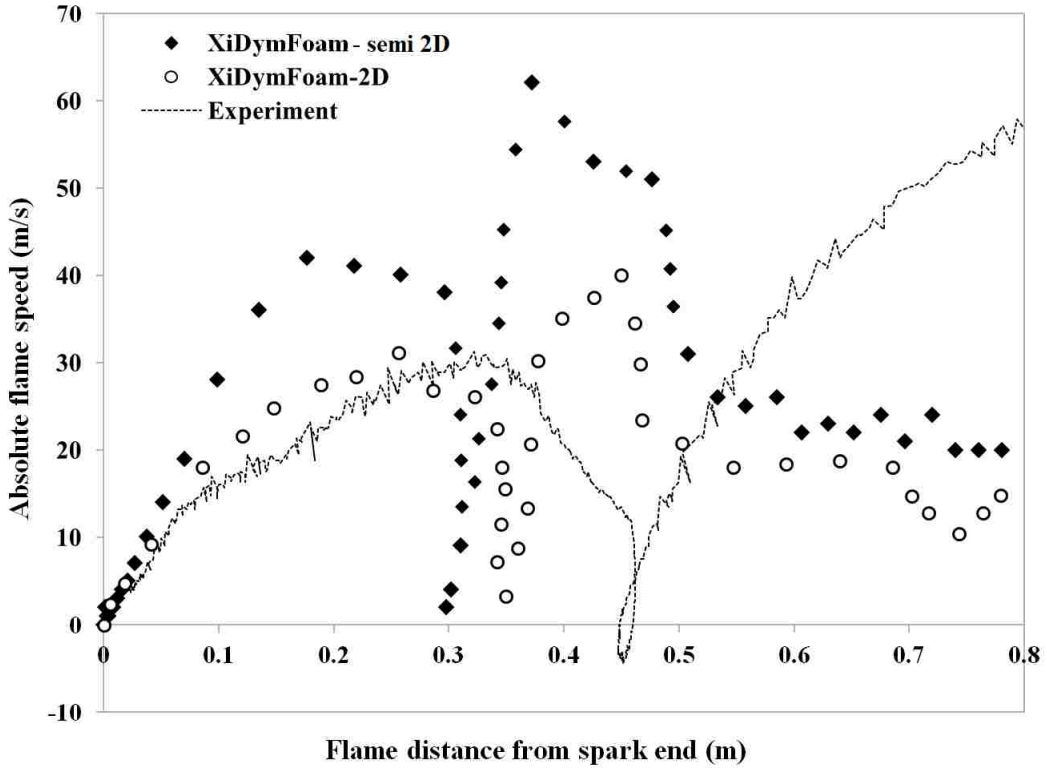

Figure 7.4: The absolute flame speed versus the flame position at duct centre-line (and referencing to the spark point) for both numerical (XiDymFoam, LES, 2D, and semi-2D) and experimental data during the tulip flame formation.

Chapter 8

8 Results for fully opened end: TFCDymFoam and FSCDymFoam models

In this chapter, the results obtained from the TFCDymFoam and FSCDymFoam combustion models for the opened end case are presented. The results are compared with the experiment.

8.1 TFCFoam and FSCFoam numerical models versus experimental results

Figure 8.1 shows the results from TFCDymFoam and FSCDymFoam in comparison to the experimental data for the rich (Φ= 1.1) premixed propane-air mixture (k =1.5 m^2/s^2, ε =0.1 m^2/s^3 and Xi*ShapeCoef* = 0.25). The flame position at the duct centre-line is shown in time. Similarly to the previous sections, the progress variable margin is used to define the flame front surface in numerical simulation.

The FSCDymFoam model replicates the experiment almost exactly up to and in the tulip flame zone (first 35 ms). This may be attributed to the capability of FSCDymFoam model for modeling of premixed laminar flame. The tulip flame and the formation of finger flame are initiated sooner in FSCDymFoam model versus the actual flame. The flame first inversion also occurs earlier and at a closer distance to the spark point.

The TFCDymFoam overestimates the experiment during first 20 ms of the flame propagation. The flat flame front and tulip flame formation start much earlier (at about 10 ms) compared to the experiment. The same trend can be seen in the first inversion flame development and location. As expected the total time for the

complete flame propagation of the TFCDymFoam model is predictably shorter, due to turbulence features of the model than in the experiment. Both the TFCDymFoam and FSCDymFoam models fail to capture the flame (flow) reverse movement at the tulip flame and the first inversion zone. This is a deficiency of using these models that should be noted.

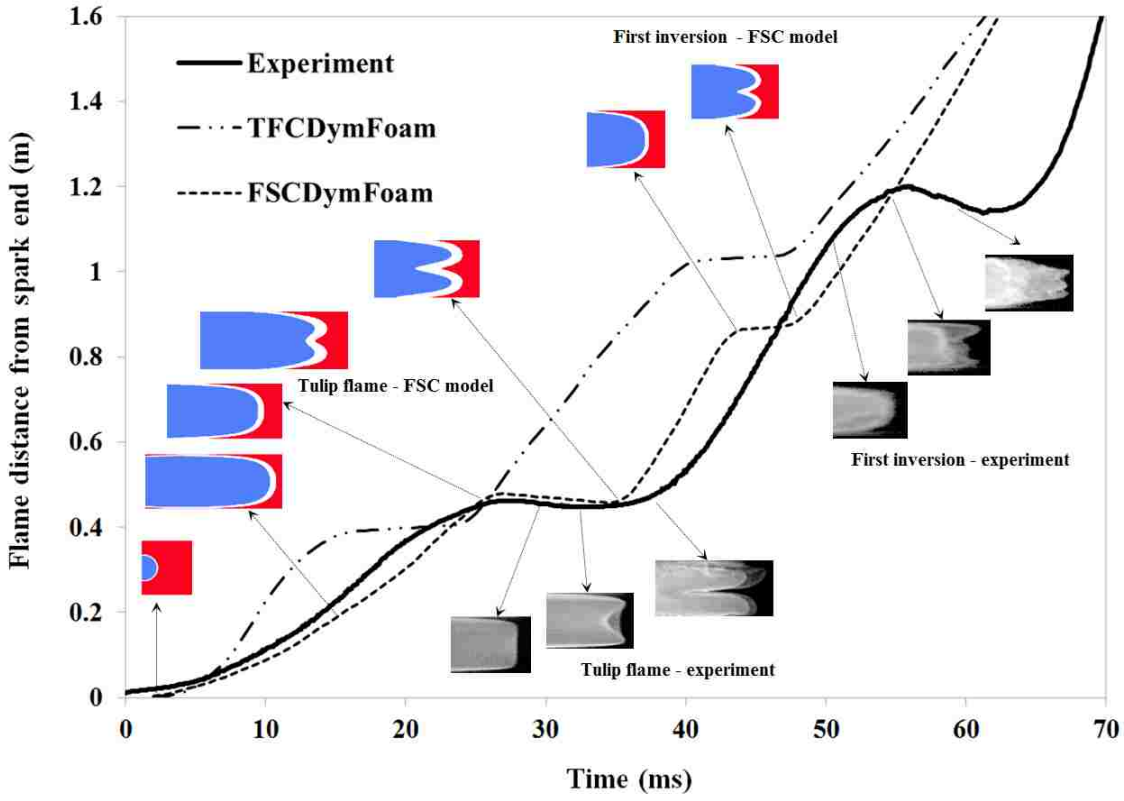

Figure 8.1: Comparison between TFCDymFoam and FSCDymFoam (RANS) and experimental results for the premixed propane-air flame. The flame position (at duct centre-line and referencing to the spark point) versus the flame propagation time. The flame surface shape at the tulip location and the flame first inversion region for both experimental and numerical (through progress variable scalar) methods are also illustrated.

Figure 8.2 shows the flame absolute speed (propagation speed) for TFCDymFoam model, FSCDymFoam model and experimental results (the same as Figure 8.1).

The dynamic of flame movement, after the tulip flame collapse (speeds are the same) and also after the inversion, is well captured by the FSCDymFoam model.

The subsequent acceleration and deceleration of the flame speed can be seen clearly in both discussed zones. The FSCDymFoam flame accelerates and decelerates with a similar manner and values as the experimental one up to the x ≈0.5 m (where the tulip flame collapses). The model also predicts the flame acceleration before the first inversion, but the flame declaration occurs in a shorter distance (about 0.9 m) compares to the experiment (about 1.2 m).

Both models have analogous trends as the empirical data at most points except near the duct outlet. Unlike for the initial stages of flame propagation (ahead of the tulip flame formation area), the TFCDymFoam and the FSCDymFoam models reproduce the experiment relatively well. The flame (flow) reverse movement and consequently the negative absolute flame speed (at the tulip flame and the flame first inversion regions) are not captured using either model. The propagation speed does reach the value zero, however, negatives are never produced.

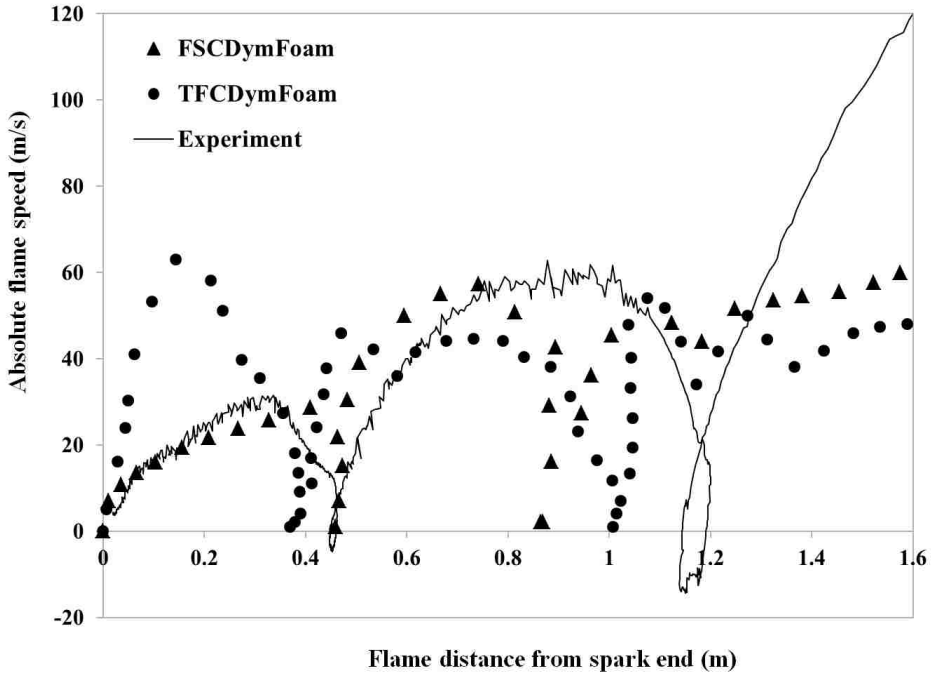

Figure 8.2: The absolute flame speed versus the flame position at duct centre-line (and referencing to the spark point) for both numerical (TFCDymFom and FSCDymFoam) and experimental data.

Chapter 9

9 Results for fully closed end: Laminar combustion model

In this chapter, the results obtained from the laminar combustion model for the closed end case are presented. These results are compared with the experimental data.

9.1 Laminar flame model versus experiment

Figure 9.1, depicts the flame front location along the duct centre-line for both the experiment and the simulation (laminar combustion model) for the closed exit end. In both cases, the tulip flame is formed around 20 cm from the spark plug, however at different times.

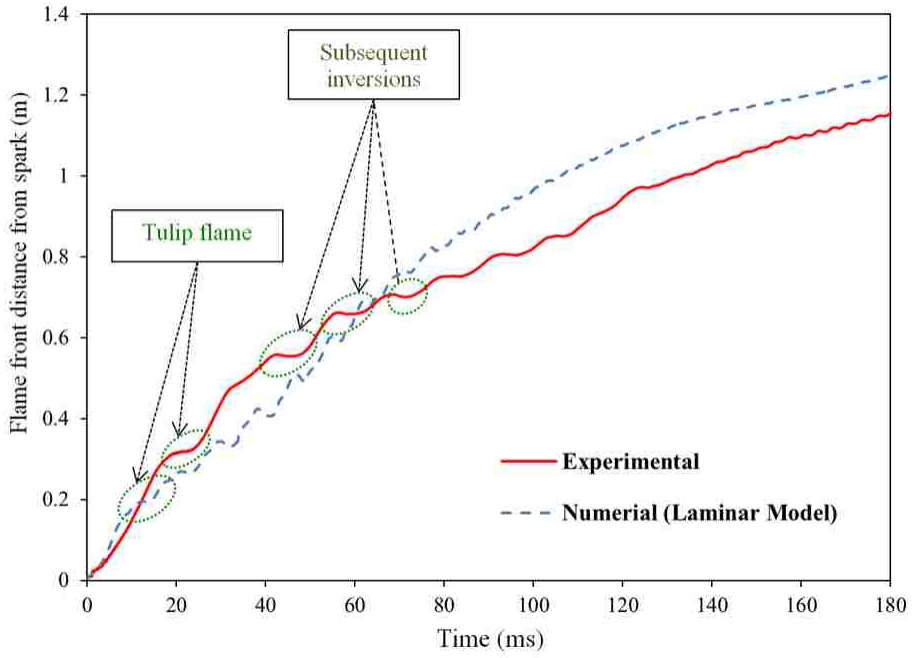

Figure 9.1: Numerical versus experimental results for the uniform composition field ($\Phi = 1.1$), changes of the flame front position along FPD centre-line for closed end.

The numerical model shows a lower flame propagation speed in comparison to empirical data up to t = 65 ms and then its speed becomes slightly higher. In the experiment, after a short distance, tongues of the tulip flame collapse and the finger shape is recreated again. This process is repeated several times, it occurs many more times than with an opened end before the flame reaches the FPD end. Much lower speed are produced as well. These subsequent inversions are not as deep as in the tulip flame. Due to increased pressure in the entire duct, the fluctuations induced by flame movement are suppressed decay and eventually the flow ahead of the flame front becomes laminar. Therefore, the laminar model can predict the flame speed more accurately in comparison with opened end cases (correlation coefficient = 0.986).

To investigate this more, the normalized flame speed (by propane laminar flame speed $\approx$ 0.32 m/s) and the normalized flame front location (by duct length) versus normalized propagation time (by total propagation time) for the numerical results are plotted in Figure 9.2. In this graph, the legends indicate the sample points distance ahead of the flame. Similar to Figure 6.4, the critical line of $U/S_l \approx 4$ should be considered for transition to a turbulent flow. Unlike the opened end case, there are clearly aggregations of sample points close to the critical line in the area of the tulip flame and for some inversions. The flow speed ahead of the flame even becomes much slower once the flame clears 60 % of duct length (and at 60 % of propagation time). The similarity of the opened end and the closed end sharply after the ignition time and just before the tulip formation starting point can be noticed.

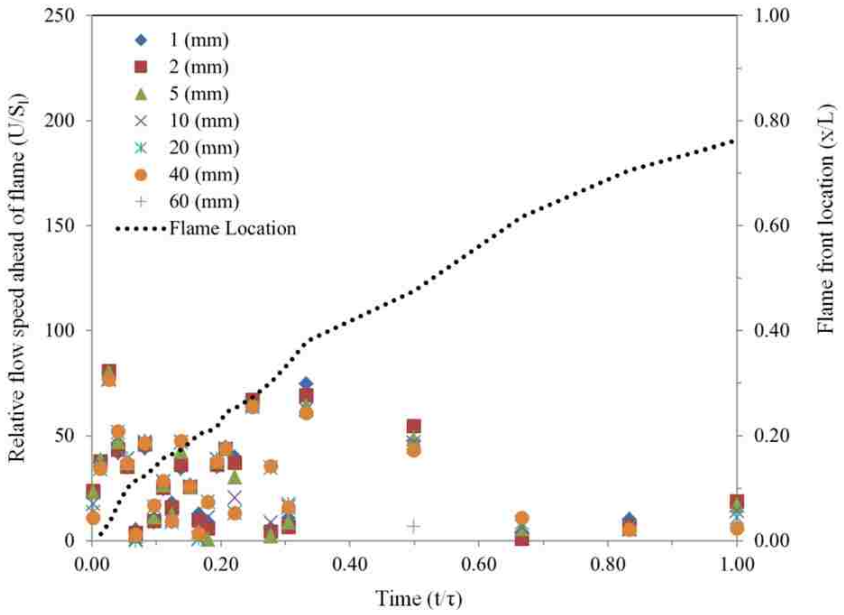

Figure 9.2: Normalized flow speed and normalized flame front location versus normalized flame propagation time from numerical results (laminar combustion model – closed end). Legends show the point distance ahead of flame.

9.2 Flame propagation speed trend

Figure 9.3, shows the absolute flame speed for the closed end and the opened end cases versus flame location. For the closed end, the position of tulip flame and subsequent inversions are located closer to the spark point in comparison with the opened end. There is a number of interesting differences and similarities.

In both cases, the flame propagates through a series of acceleration and periods. The speed are about the same shortly after the ignition.

In the closed end, there is a large number of acceleration and deceleration periods, and only initial few resemble the opened end case. With the exception of the initial (after ignition) period, the flame speeds are lower and decrease progressively as the flame propagates in the duct. Past the x $\approx$1 m, the flame moves forward with high-frequency oscillation. This suggests that the absolute flame speed at the laminar conditions is decreased by the increase in pressure [36].

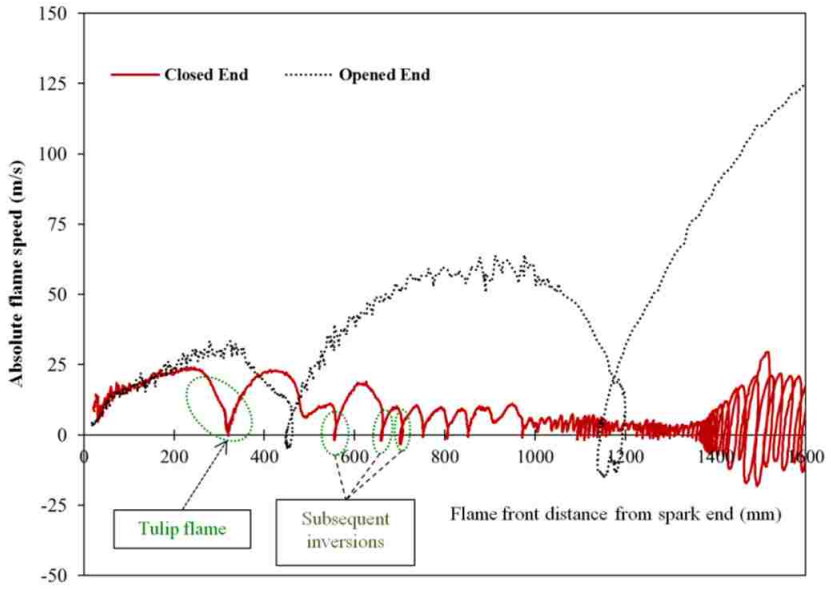

Figure 9.3: Changes of absolute flame speed along the channel centre-line; fully closed exit, mixture equivalence ratio $\Phi = 1.1$ (experimental result). Fully opened end case is also plotted for comparison.

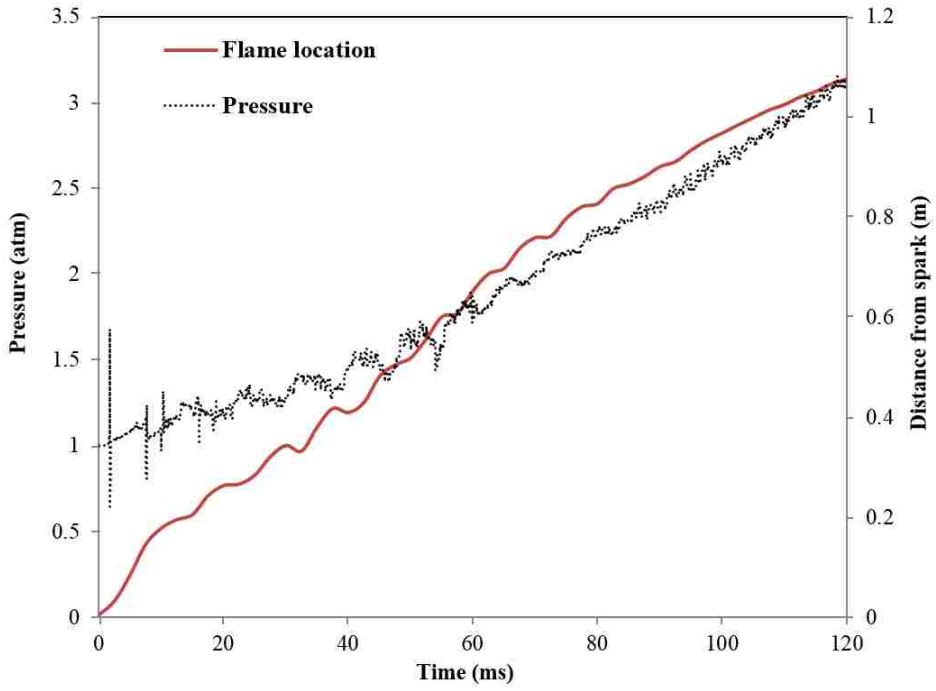

Figure 9.4: Flame location and pressure variation at the ignition site versus propagation time from the numerical simulation (laminar model) for closed end case ($\Phi = 1.1$).

This total pressure rise in the duct is shown in Figure 9.4. As the flame speed is much lower, in this case, the pressure waves play a more important role on flame inversions development. As the Figure 9.4 shows, the pressure difference between t = 0 - 120 ms (when x $\approx$ 0 - 1.1 m), is about 2 atm. This much of pressure with a delay (due to the pressure wave propagation) will be the pressure for the whole duct and it decreases the flame speed and it causes all those flame oscillations near the duct end.

Chapter 10

10 Results for fully closed end: Thickened flame model (TFMDymFoam)

In this chapter, the results obtained from the thickened flame model (TFMDymFoam) for the closed end case are presented. These results are compared with the experimental data.

10.1 Thickened flame model (TFMDymFoam) results versus experimental results

Figure 10.1 shows the premixed propane-air ($\Phi = 0.8$) flame front development from the kernel flame to the tulip flame formation point. The 3D model has been used in this part. The laminar TFMDymFoam model can simulate all stages which are involved in the tulip creation qualitatively well. At t = 5 ms, the flame still has its spherical shape. As the flame develops, it touches the top and bottom walls and the flame forms the finger shape (t = 15 ms). At t = 32 ms, the flame skirts have already touched the front and back side walls but the flame front still maintains its finger shape. At t = 45 ms, the flame front surface becomes flat. The dent initiates at the flat front surface at t = 55 ms and this split grows continuously until forming the tulip flame (t = 75 ms).

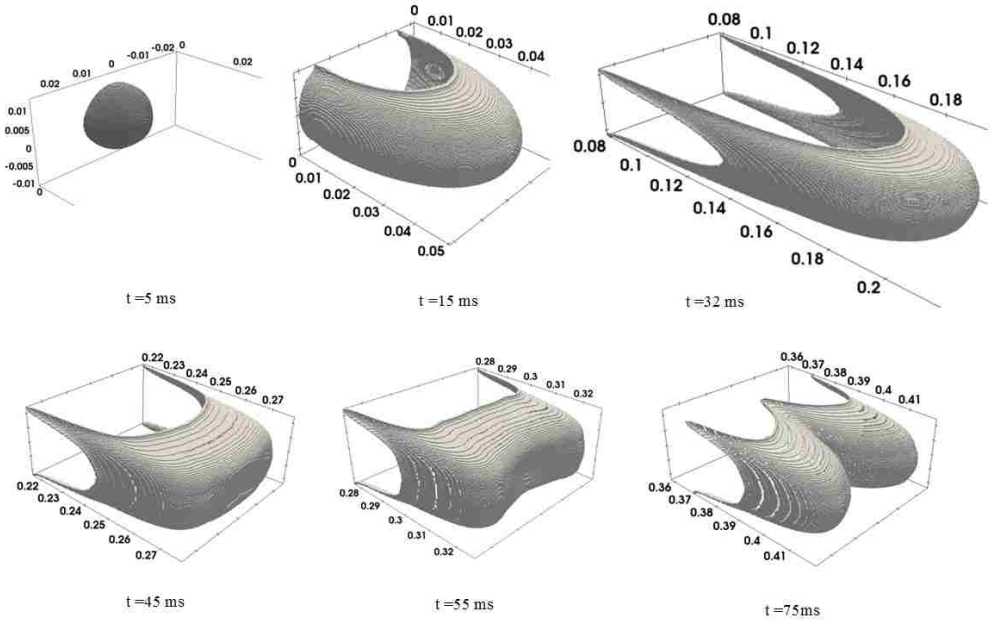

Figure 10.1: Premixed propane-air flame front surface development from kernel growing to the tulip formation point ($\Phi = 0.8$ - closed end). This is based on the regress variable margin (0.10 – 0.55). Unit on the length axis are meters.

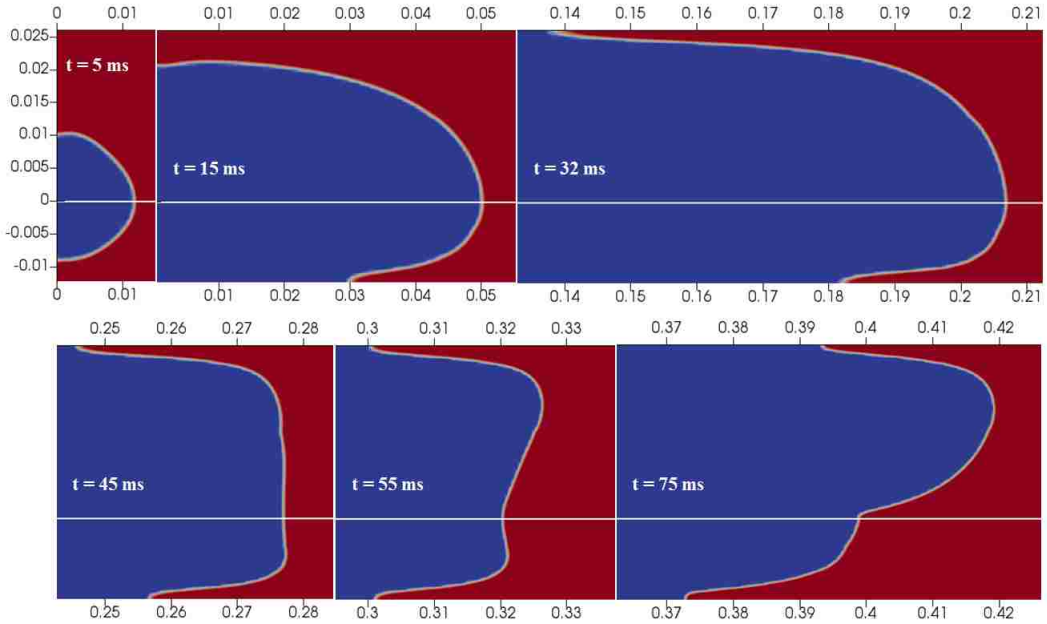

Figure 10.2: Sequence of the premixed propane-air flame cross-section and the duct vertical centre plane, from kernel growing to the tulip formation point ($\Phi = 0.8$ - closed end). This is based on the regress variable margin (0.10 – 0.55). Unit on the length axis are meters.

Figure 10.2 illustrates the sequence of premixed propane-air flame cross-section and the duct vertical centre plane for the same time steps as Figure 10.1. The split (tulip) is much deeper and clear on the wider side of the duct. The flame and the top-bottom walls contact area are much larger than the flame and side walls contact areas. This would confirm again the critical role of the flame-wall contact area on the tulip flame formation.

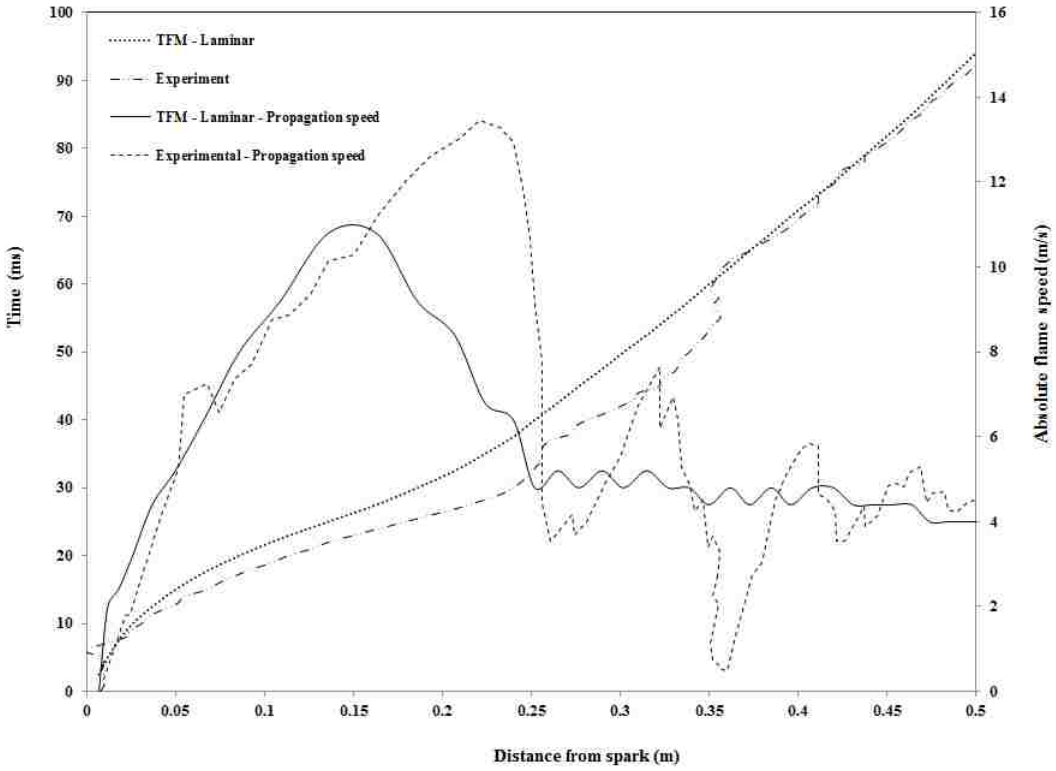

Figure 10.3: Comparison between laminar TFMDymFoam and experimental results for the premixed propane-air mixture ($\Phi = 0.8$ - closed end), flame propagation time (left) and flame absolute speed (right) versus flame tip position (referencing to the spark point).

Figure 10.3 shows both experimental and numerical results for the flame propagation time and the absolute flame speed versus the flame tip position (with reference to the spark point). The TFMDymFoam can predict the experiment at the initial stage of flame propagation after the spark up to x = 0.05 m. Afterward, the model underestimates the experiment up to the point x = 0.35 m. The largest discrepancy can be

seen in tulip area formation. Also, the model can not simulate the flame semi-stall states at x$\approx$ 0.25m and x $\approx$ 0.35m. In terms of flame absolute speed, the general trend for the TFMDymFoam model and the experiment are similar. But between point x $\approx$ 0.15 - 0.25 m, the differences between two results increases. The top propagation speed for the experiment is about 13 m/s, however, the numerics can only predict 11 m/s. After point x $\approx$ 0.25m, the propagation speed for the experimental flame has greater fluctuations compared to the TFMDymFoam results. Setting the laminar condition for TFMDymFoam model may be the cause of this effect as the influence of flame speed increase by the possible turbulent feeding flow is ignored in this calculation.

11 Conclusion and recommendations

This chapter introduces the summary of the work, the conclusion of the results and the recommendations for future studies.

11.1 Summary

The objective of this study is to investigate the premixed (propane-air) flame propagation in the long length straight rectangular duct. This propagation includes different phenomena such as the tulip flame formation and the flame subsequent inversion/inversions. The duct outlet condition do not affect on the tulip flame formation, but it has a direct influence on the number and the location of subsequent inversion/inversions.

In the past, many works have been done on the tulip flame formation and the reasons behind this phenomenon. In this study numerical simulation has employed for the detailed study of this phenomenon, the facts behind its creation and its effects in flame propagation speed.

Also, this study extend to the subsequent inversion/inversions which was seldom explored in previous research works. The flame feeding flow and flame-wall interchangeable interactions during flame propagation is discussed. Emphasis of these discussions are on the tulip flame and first flame inversion for an open end outlet condition because the flame propagation in open end duct/tube can be more complex in terms of the feeding flow conditions.

Alternation of the flame feeding flow condition from laminar to turbulent (and vice versa) during the flame propagation in the duct, prompted the idea of testing different laminar and turbulent combustion models (such as XiFoam, TFC, and TFM). Furthermore, validation of FSC model (which claims that it has the capability of capturing both laminar and turbulent flame by switching between these two

cases automatically) was attempted. The first part of the numerical simulation has been done using the Star CCM+ (the EBU model but limiting to Arrhenius reaction rate:: Semi-laminar). For the second part, the OpenFOAM code (XiFoam) was utilized. The TFCFoam, TFCDymFoam, FSCFoam, FSCDymFoam, TFMFoam and TFMDymFoam models for all 2D, semi-2D, and 3D geometries were all made based on the XiFoam model.

The analytical works published by other research groups [12, 14, 25, 50, 51] were adopted and modified for the rectangular channel and the results are utilized as another datum for the obtained experimental and numerical data.

11.2 Major findings and conclusions

- For the open end case after the ignition, the spherical flame starts growing. Quickly afterward, the flame accelerates and assumes a finger shape where the flame total surface increases significantly. The flame continues to grow until the substantial lateral part of the flame skirt touches the wall. The flame deceleration acts on and the surface of flame front becomes flat. The flame total surface decreases considerably and the flame absolute speed reaches zero (and even it gets negative value at the experimental case). Thereafter, a dent at the surface of flame front keeps growing through the flame centre and splits the flame front into two flame lips. This phenomenon has been named a tulip flame [20].

- As the dent grows the tulip flame becomes deeper, the front part of the flame starts to accelerate once again. At the same time, the formed flame lips start to collapse. The flame again assumes the finger shape. This time the flame has higher propagation speed and longer lateral skirt in comparison with the former tulip flame zone. The longer flame skirt causes the larger flame total surface. When the flame again touches the wall, the total burning surface gets reduced

and the absolute flame speed decreases to almost zero (again a negative value in experimental result can be seen). The flame front obtains the flattened profile however it is not as smooth as it used to be at the tulip flame zone. The dent appears on the flame front surface and it starts growing. This time, the dent does not go as deep as the tulip flame and the formed lips are much smaller and they are more wrinkled. This phenomenon is called the first flame inversion.

- Once again, the lips start collapsing and the flame assumes the finger shape. For the fully open outlet case, the flame accelerates and leaves the duct at high speed (in the order of 100 m/s). For the fully close outlet case, the flame undergoes more subsequent inversions. These flame inversions are similar to the first flame inversion, however they are not as deep as the flame first inversion. The absolute flame speed observed in this zone is generally about 5 m/s with maximum flame speeds not exceeding 20 m/s.

- Unlike the tulip flame, the subsequent inversions (including the first one) can not repeat each other quantitatively (respect to the location and time) for the different experimental trials. It is speculated that this relates to the chaotic turbulent behavior of the feeding flow. The same flame behavior similar to the tulip flame formation can be seen in all these trials (Qualitative comparison). In other words, the gentle flame deceleration, and the subsequent flame acceleration happen for all those inversions in all experimental trials.

- The numerical result shows that the feeding flow ahead of flame front goes through different conditions during the flame propagation. These conditions are assessed based on the flow speed and consequently the local Reynolds number. At the initial stage of flame propagation (ignition and flame kernel growing) the flow is laminar. As the flame transits to the finger shape, the flow condition changes to transitional and turbulent. When the flame contacts the wall, the

flow returns back to the transitional and the laminar state and then the flame front profile becomes flat. After the collapsing of flame lips, the flame begins to accelerate and the flow rapidly enters the transitional and turbulent conditions again. The same process repeats for the flame first inversion for the open end outlet case. Although, rather than the laminar condition, the flow has the transitional condition at the first flame inversion point. The flow is incapable of entering a laminar state. After the first flame inversion collapsing, the flow again progresses back to the turbulent condition. For the closed end case, after the tulip flame lips merge, the flow is mostly transitional and laminar for the rest of the flame propagation until the end of duct (including the subsequent inversions).

- The flame condition should follow the feeding flow state. Therefore, when the flow ahead of flame is laminar, transitional or turbulent one can expect that the flame also has similar state respectively. This is the main assumption behind employing the laminar and turbulent numerical combustion models in this study.

- The main force for propelling the flame forward is the resultant of burning gas volume. Consequently, as the flame propagates through the duct, the volume of the burned gas increases and therefore increases the propelling force at the rear of the flame. The flame surface area also has a direct impact on the burning rate where the higher the flame surface area, the greater the burning rate. Therefore, the wrinkles which are caused by turbulent eddies at the flame surface increase the burning rate. Moreover, the density gradient between the burnt and fresh gasses provides diffusion forces for the flame forward movement. The last two mentioned force influences are not significant in compare with the first one.

- The numerical results (semi-laminar model - Star CCM+) show as the flame

skirt touches the wall a series of vortices/eddies are created. Unequal acceleration is the result of the nonaligned density and pressure gradients have direct influence in the formation of these vortices/eddies. Pressure gradients at the tulip zone are a result of the flame-wall contact and are typically 17 kPa in magnitude. The RT instabilities occur which cause vortices to form where the pressure wave amplitude is on the order of 1 kPa or higher. The generated vortices go along the flame skirt and reduce the propelling effect which is caused by the burning gas behind the flame front. The direction of the eddies/vortices are opposite of the main flame direction at the duct centre. The vortices/eddies creation ahead of the flame front and at wall vicinity is also observed which causes a reduction in the flame absolute speed in these areas. This reduction continues until a flattened profile of the flame while a dent appears at the flame front centre. At this point, the instabilities and the vortices/eddies effects are coupled and make the dent grow deeper. The flow direction prevents the flame to go over the split unburnt area and the enclosed mixture is always in contact with the flame hot surface (except at front points). This causes a temperature rise in this area due to the diffusion which suddenly repels the weakened flow effect and it pushes the flame forward. The flame lips collapsing is considered as the results of this step.

- After the flame lips collapsing and the flame finger shape formation, there is no effective vortices/eddies ahead or behind the flame front. The burnt gas propelling force moves the flame forward again. This phenomenon at the tulip formation zone also occurs another time at the first flame inversion in open end case. In this case because of the much higher volume of burnt gas, the vortices/eddies can not make the flame front split as deep as the tulip flame. Furthermore, as the feeding flow is mostly in transitional and turbulent condition, it is expecting to have more small eddies rather than bigger vortices. As

a result, a more obvious wrinkled flame is observed compares to the tulip flame zone.

- The modified analytical results were not helpful. This was due to the unacceptable deficiency of the obtained results from this method in comparison to the experimental data. Therefore, its usage did not extend in all numerical sections.

- In this study, different numerical combustion models and two CFD software packages have been employed:

  - Semi-laminar combustion model (Star CCM+):

    * EBU model but its source term is limited to the Arrhenius reaction rate

  - Turbulent combustion models (OpenFOAM):

    * XiFoam model & RANS

    * XiFoam model & LES

    * TFCFoam model & RANS

  - Combustion model that can capture both laminar and turbulent conditions concurrently (OpenFOAM):

    * FSCFoam model & RANS

  - Laminar combustion model (OpenFOAM):

    * TFMFoam model (this model can be utilized in turbulent condition as well)

- In order to employ the above-mentioned models (OpenFOAM cases), considering the cell size, mesh numbers and time step, it is required to couple the models with adaptive mesh. Therefore a dynamic model was created for each model (XiDymFoam, TFCDymFoam, FSCDymFoam, and TFMDymFoam) and were

used for the 3D and semi-2D cases. Further modifications were necessary to make the models ready for the 2D geometries.

- All discussed combustion models could qualitatively simulate the propane-air tulip flame and the first inversion in an acceptable manner.
- For the fully opened end outlet:
  - The semi-laminar model (Star CCM+) simulates the flame first inversion quicker and closer to the ignition point in comparison to the experimental data (Φ=1.1). Generally the flame is slower and the whole propagation time is longer in comparison.
  - All examined cases of RANS & XiFoam model results (Table 7.1) show that this turbulent model could not simulate the initial stages of flame propagation prior to the tulip flame. The model is also sensitive to the initial conditions and the coefficients. Both of the tulip flame and the flame first inversion occur quicker and at a closer distance in a reference to the spark end. The whole propagation time is also shorter compared to the experimental data (Φ=1.1).
  - The LES & XiFoam model result provides a better simulation of the flame propagation at the initial stage in comparison to the RANS cases. Albeit, the propagation speed has a higher value in most of the points up to the tulip flame creation. Afterward, at the flame first inversion zone, the numeric underestimates the experiment (Φ=1.1) considerably.
  - There similarities between the TFCFoam model (RANS) and XiFoam (RANS) results. This can be seen especially at the tulip formation zone when both models have overestimated the experimental data (Φ=1.1). The TFCFoam flame flatten profile and tulip flame formation starts much quicker compared to the experiment. Despite the last section of the duct

(after the flame first inversion), the TFCFoam overestimated the experimental absolute flame speed.

  - As expected the FSCFoam model provides a better simulation at both the tulip flame and the flame first inversion regions. This can relate to the capability of FSC model for modeling of premixed flame at both laminar and turbulent conditions. The model results and experimental data (Φ=1.1) are almost identical up to the tulip flame collapsing point. After this point the model overestimates the experimental data. The FSC flame first inversion happens quicker and at a closer distance to the spark point in comparison to experimental data. Although, it generally presents better outcomes (in terms of time, flame location and flame absolute speed) among all other above mentioned models. The FSCFoam model captures well the flame propagation in the duct predictably both the tulip flame formation and the first inversion occurrence at similar time and location.

- For the fully closed end outlet:

  - The semi-laminar model (Star CCM+) simulates the tulip flame in a shorter distance from spark versus the experimental data (Φ=1.1). The model can reproduce the subsequent inversion for the rest of the flame propagation in the duct. In a closed end duct cases the flame propagation is occurs through laminar feeding flow conditions which provides better result when compared to opened end outlet cases.

  - The 3D modeling of tulip flame using the laminar TFMDymFoam presents acceptable results in comparison to the experimental data (Φ=0.8). The TFMDymFoam can predict the experiment at the initial stage of flame propagation after the spark initiation. For the point that is assumed to have turbulent feeding flow, the model underestimates the actual flame.

11.3 Summary of contributions

The following list contains the major contributions that this work has provided to the field of engineering science:

- The author proposed the coupling of the formed vorticities (as the results of flame-wall touch) and the instabilities as the main reasons behind the formation of tulip flame and the first inversion.

- The flame propagation in the long length duct includes the laminar, transitional, and turbulent flame (feeding flow states). Therefore, the author proposed this physical mechanism as an alternative case for validation of combustion models.

- The author developed XiDymFoam, TFCDymFoam, FSCDymFoam, and TFMDymFoam models for both 2D and 3D cases. These models were created based on the XiFoam model which is the embedded model for the simulation of premixed/partially premixed turbulent combustion in OpenFOAM 2.2.2.

11.4 Recommendations and future work

- For the opened end case, the experiment exhibits reverse flame (flow) movement (negative absolute flame speed) at both tulip flame and flame first inversion regions. None of the numerical models used in this study can predict this behavior. This requires further investigation.

- The FSC solvers which was made in OpenFOAM for this study is capable for more applications (e.g. Engine). The application of this solver for the further numerical combustion engine studies is recommended.

- The effects of compression wave which is initiated by the spark and unsteady flame propagation on the tulip flame and the flame subsequent inversion require further research. Also, the wave traveling through the duct and it reflects from

the duct end should be considered. Separate numerical equation/models may be need to add to the current solver equations.

- Finding the relationship between the flame absolute speed and the exit velocity at duct outlet (fully opened end case) during the flame propagation and through the experimental method is recommended (using LDA).

References

[1] Ellis, O. D. C. (1928). Flame movement in gaseous explosive mixtures. *Fuel Sci*, 7(11), 502-508.

[2] Warnatz, J., Maas, U., & Dibble, R. W. (2013). *Combustion: Physical and Chemical Fundamentals, Modeling and Simulation, Experiments, Pollutant Formation*: Springer Berlin Heidelberg.

[3] Kuo, K. K. (2005). *Principles of Combustion*: John Wiley, New York.

[4] Peters, N. Turbulent Combustion, 2000: Cambridge University Press, Cambridge.

[5] Lee, J., & Moen, I. (1980). The mechans of transition from deflagration to detonation in vapor cloud explosions. *Progress in Energy and Combustion Science*, *6*(4), 359-389.

[6] Borghi, R. (1985). On the structure and morphology of turbulent premixed flames *Recent Advances in the Aerospace Sciences* (pp. 117-138): Springer.

[7] Lewis, B., & Von Elbe, G. (2012). *Combustion, Flames and Explosions of Gases*: Elsevier.

[8] Xiao, H., Houim, R. W., & Oran, E. S. (2015). Formation and evolution of distorted tulip flames. *Combustion and Flame*, *162*(11), 4084-4101.

[9] Oran, E. S., & Gamezo, V. N. (2007). Origins of the deflagration-to-detonation transition in gas-phase combustion. *Combustion and Flame, 148*(1–2), 4-47.

[10] Matalon, M., & Metzener, P. (1997). The propagation of premixed flames in closed tubes. *Journal of Fluid Mechanics, 336*, 331-350.

[11] Zhou, B., Sobiesiak, A., & Quan, P. (2006). Flame behavior and flame-induced flow in a closed rectangular duct with a 90° bend. *International Journal of Thermal Sciences, 45*(5), 457-474.

[12] Bychkov, V., Akkerman, V. y., Fru, G., Petchenko, A., & Eriksson, L.-E. (2007). Flame acceleration in the early stages of burning in tubes. *Combustion and Flame*, *150*(4), 263-276.

[13] Starke, R., & Roth, P. (1986). An experimental investigation of flame behavior during cylindrical vessel explosions. *Combustion and Flame, 66*(3), 249-259.

[14] Clanet, C., & Searby, G. (1996). On the "tulip flame" phenomenon. *Combustion and Flame, 105*(1), 225-238.

[15] Dunn-Rankin, D., Barr, P., & Sawyer, R. (1988). *Numerical and experimental study of "tulip" flame formation in a closed vessel.* Paper presented at the Symposium (International) on Combustion.

[16] Kessler, D. A., Gamezo, V. N., & Oran, E. S. (2010). Simulations of flame acceleration and deflagration-to-detonation transitions in methane-air systems. *Combustion and Flame, 157*(11), 2063-2077.

[17] Bradley, D., Lawes, M., & Liu, K. (2008). Turbulent flame speeds in ducts and the deflagration/detonation transition. *Combustion and Flame, 154*(1-2), 96-108.

[18] Abu-Orf, G. M., & Cant, R. S. (2000). A turbulent reaction rate model for premixed turbulent combustion in spark-ignition engines. *Combustion and Flame, 122*(3), 233-252.

[19] Fairweather, M., Hargrave, G. K., Ibrahim, S. S., & Walker, D. G. (1999). Studies of premixed flame propagation in explosion tubes. *Combustion and Flame, 116*(4), 504-518.

[20] Salamandra, G., Bazhenova, T., & Naboko, I. (1959). Seventh Symposium (International) on Combustion. *The Combustion Institute, Butterworths,* 851.

[21] Sobiesiak, A., Battoei, M., Barbour, E., Mackellar, S., & Ting, D. (2006). *Flame Inversions in a Rectangular Duct with 90^{o}Bend.* Paper presented at the The Combustion Institute/Canadian Section, Spring Technical Meeting.

[22] Marra, F. S., & Continillo, G. (1996). Numerical study of premixed laminar flame propagation in a closed tube with a full navier-stokes approach. *Symposium (International) on Combustion, 26*(1), 907-913.

[23] Gonzalez, M. S., & Garcia, E. S. (1992). Effect of azadirachtin on the development of Trypanosoma cruzi in different species of triatomine insect vectors: Long-term and comparative studies. *Journal of Invertebrate Pathology, 60*(2), 201-205.

[24] Guenoche, H., & Markstein, G. (1964). Nonsteady flame propagation. *Pergamon Press, New York,* 107.

[25] Xiao, H., Makarov, D., Sun, J., & Molkov, V. (2012). Experimental and numerical investigation of premixed flame propagation with distorted tulip shape in a closed duct. *Combustion and Flame, 159*(4), 1523-1538.

[26] Kratzel, T., Pantow, E., & Fischer, M. (1998). On the transition from a highly turbulent curved flame into a tulip flame. *International Journal of Hydrogen Energy, 23*(1), 45-51.

[27] Dunn-Rankin, D., & Sawyer, R. F. (1998). Tulip flames: Changes in shape of premixed flames propagating in closed tubes. *Experiments in Fluids, 24*(2), 130-140.

[28] Kuzuu, K., Ishii, K., & Kuwahara, K. (1996). Numerical simulation of premixed flame propagation in a closed tube. *Fluid Dynamics Research, 18*(3), 165-182.

[29] Metzener, P., & Matalon, M. (2001). Premixed flames in closed cylindrical tubes. *Combustion Theory and Modelling, 5*(3), 463-483.

[30] Matalon, M., & McGreevy, J. L. (1994). Twenty-Fifth Symposium (International) on CombustionThe initial development of a tulip flame. *Symposium (International) on Combustion, 25*(1), 1407-1413.

[31] Chomiak, J., & hou, G. (1996). A numerical study of large amplitude baroclinic instabilities of flames. *Symposium (International) on Combustion, 26*(1), 883-889.

[32] Fernandez, G., & Guillard, H. (1989). Implicit schemes for subsonic combustion problems. In A. Dervieux & B. Larrouturou (Eds.), *Numerical Combustion* (Vol. 351, pp. 277-286): Springer Berlin Heidelberg.

[33] Sethian, J. (1984). Turbulent combustion in open and closed vessels. *Journal of Computational Physics, 54*(3), 425-456.

[34] Sobiesiak, A., & Zhou, B. (1999). Paper presented at the The Combustion Institute/Canadian Section Spring Technical Meeting.

[35] Poinsot, T., & Veynante, D. (2005). *Theoretical and Numerical Combustion*: Edwards.

[36] Lipatnikov, A. (2012). *Fundamentals of Premixed Turbulent Combustion*: Taylor & Francis.

[37] Schmidt, E. H., Steinicke, H., & Neubert, U. (1953). *Flame and schlieren photographs of combustion waves in tubes.* Paper presented at the Symposium (International) on Combustion.

[38] Yasari, E. (2015). *RANS Simulations of Interaction between Premixed Flame and Turbulence using OpenFOAM Library*: Chalmers University of Technology.

[39] McKellar, S. W. (2003). Combustion of propane-air mixtures with oxygenated additives in a closed duct and an SI engine.

[40] Star CCM+ Documentation. (2015). from https://steve.cd-adapco.com

[41] Gülder, Ö. L. (1984). *Correlations of laminar combustion data for alternative SI engine fuels* (No. 0148-7191): SAE Technical Paper.

[42] Weller, H. G., Tabor, G., Gosman, A. D., & Fureby, C. (1998). Application of a flame-wrinkling les combustion model to a turbulent mixing layer. *Symposium (International) on Combustion, 27*(1), 899-907.

[43] Lipatnikov, A. N., & Chomiak, J. (1997). *A Simple Model of Unsteady Turbulent Flame Propagation.* Retrieved from http://dx.doi.org/10.4271/972993.

[44] Zimont, V., & Lipatnikov, A. (1995). A numerical model of premixed turbulent combustion of gases. *Chem. Phys. Rep, 14*(7), 993-1025.

[45] Zimont, V., Polifke, W., Bettelini, M., & Weisenstein, W. (1998). An efficient computational model for premixed turbulent combustion at high Reynolds numbers based on a turbulent flame speed closure. *Journal of Engineering for Gas Turbines and Power, 120*(3), 526-532.

[46] Lipatnikov, A. N., & Chomiak, J. (2000). Transient and Geometrical Effects in Expanding Turbulent Flames. *Combustion Science and Technology, 154*(1), 75-117.

[47] Lipatnikov, A. N., & Chomiak, J. (2002). Turbulent flame speed and thickness: phenomenology, evaluation, and application in multi-dimensional simulations. *Progress in Energy and Combustion Science, 28*(1), 1-74.

[48] Yasari, E., & Lipatnikov, A. (2012). *Application of OpenFOAM Library to Simulations of Premixed Turbulent Combustion Using Flame Speed Closure Model.* Paper presented at the Conference on Modelling Fluid Flow CMFF'12, September 4-7, 2012. Conference Proceedings CD-Rom.

[49] Yasari, E., & Lipatnikov, A. (2013). *RANS Simulations of Premixed Turbulent Flames Using TFC and FSC Combustion Models and OpenFOAM Library.* Paper presented at the Proceedings of 6th European Combustion Meeting, Lund, Sweden, 25-28 June, 2013, CD.

[50] Xiao, H., He, X., Duan, Q., Luo, X., & Sun, J. (2014). An investigation of premixed flame propagation in a closed combustion duct with a 90° bend. *Applied Energy, 134*(0), 248-256.

[51] Xiao, H. (2015). *Experimental and Numerical Study of Dynamics of Premixed Hydrogen-Air Flames Propagating in Ducts*: Springer Berlin Heidelberg.

[52] Pope, S. B. (2000). *Turbulent Flows*: Cambridge University Press.

[53] Shalaby, H., Luo, K. H., & Thévenin, D. (2014). Response of curved premixed flames to single-frequency and wideband acoustic waves. *Combustion and Flame, 161*(11), 2868-2877.

[54] Teerling, O. J., McIntosh, A. C., Brindley, J., & Tam, V. H. Y. (2005). Premixed flame response to oscillatory pressure waves. *Proceedings of the Combustion Institute, 30 II*, 1733-1740.

[55] Colin, O. , Ducros, F., Veynante, D. & Poinsot, T. (2000). A thickened flame model for large eddy simulations of turbulent premixed combustion. *Phys. Fluids. 12* (7), 1843 - 1863.

[56] Baniabedalruhman, A. (2015). Dynamic meshing around fluid-fluid interfaces with applications to droplet tracking in contraction geometries.

[57] Cabral, B., & Leedom, L. C. (1993). Imaging vector fields using line integral convolution. In *Proceedings of the 20th annual conference on Computer graphics and interactive techniques*, 263-270. ACM.

Vita Auctoris

Name: Zakaria Movahedi

Place of Birth: Brojerd, Lorestan, Iran

Year of Birth: 1982

Education: National Organization for Development of Exceptional Talents (NODET) high school, Brojerd, Iran, 2001

Imam Hussein University (IHU),
B.Sc. Mechanical Engineering (Solid Design),
Tehran, Iran, 2006

University of Hertfordshire,
M.Sc. Automotive Engineering,
Hatfield, Hertfordshire, UK, 2011

University of Windsor,
PhD Mechanical Engineering
Windsor, Ontario, Canada (2012-2017)